UNIVERSITÀ DEGLI STUDI DI URBINO «CARLO BO»

DIPARTIMENTO DI SCIENZE PURE E APPLICATE (DiSPeA)

DOTTORATO DI RICERCA
IN SCIENZE DELLA TERRA, SCIENZA DELLA COMPLESSITÀ

Heat source and reservoir of geothermal areas in Latin America as inferred from thermobarometry of amphibole-bearing extrusives and fluid geochemistry: examples from Chile and Ecuador

by

Gorini Andrea

Tutor
Chiar.mo Prof. Renzulli Alberto

Co-Tutor
Chiar.mo Prof. Capaccioni Bruno†

Co-Tutor
Chiar.mo Dott. Ridolfi Filippo

XXVIII CICLO - Anno Accademico 2014/2015
Settore Scientifico Disciplinare
GEO/08 GEOCHIMICA E VULCANOLOGIA

List of contents

1. Introduction 1

1.1 RENEWABLE VS NON-RENEWABLE RESOURCES 1

1.2 GEOTHERMAL ENERGY AS RENEWABLE RESOURCE 3

1.3 GEOTHERMAL RESOURCES IN LATIN AMERICA 5

2. Geothermal resources: an overview on systems, exploration, technology, environmental impact 7

2.1 DIFFERENT TYPES OF GEOTHERMAL SYSTEMS 7

2.2 EXPLORATION FOR GEOTHERMAL RESOURCES 8

2.3 STATE OF THE ART OF EXPLOITATION TECHNOLOGY 12

2.3.1 Advanced power plants technology and unconventional geothermal resources 14

2.3.1.1 Self-superheating (SSH) and combined-cycle power plants 15

2.3.1.2 Hybrid systems and combined heat and power production (CHP) 15

2.3.1.3 Hot dry rocks and enhanced geothermal systems (EGS) 16

2.3.1.4 Closed-Loop Geothermal Wells 17

2.3.1.5 Coproduction of geothermal and Oil/Gas and geopressured geothermal systems 18

2.3.1.6 Supercritical fluids and magmatic systems 19

2.3.2 Direct Use 21

2.4 ENVIRONMENTAL IMPACT 22

3. Current status of power production from geothermal resources 24

3.1 THE WORLD SCENARIO 24

3.2 GEOTHERMAL RESOURCES IN CHILE 26

3.2.1 The Apacheta Geothermal project 27

3.3 GEOTHERMAL RESOURCES IN ECUADOR 29

3.3.1 The Tufiño-Chiles-Cerro Negro geothermal field 30

3.3.2 The Chachimbiro geothermal field 31

4. The application of amphibole thermobarometry to constrain the heat source of geothermal systems in geothermal areas of Chachimbiro (Ecuador), Apacheta and La Torta (Chile) 34

4.1 INTRODUCTION 34

4.2 VOLCANOLOGICAL, GEOPHYSICAL, GEOCHEMICAL AND GEOTHERMAL BACKGROUND 35

4.2.1 The Apacheta and La Torta geothermal areas (Chile) 35
4.2.2 The Chachimbiro Geothermal Area (Ecuador) 38

4.3 SAMPLES AND ANALYTICAL METHODS 40

4.4 RESULTS 40

4.4.1 Mineral chemistry and petrography 40

4.4.2 Amphibole texture and classification 48

4.5 DISCUSSION 50

4.5.1 Compositional-textural relationship of amphiboles 50
4.5.2 Amphibole thermobarometry application. The P-T-h diagram 55
4.5.3 Comparison between thermobarometric and geophysical constraints 59

4.6 CONCLUSIONS 62

5. Origin of geothermal fluids along active to semi-dormant volcanoes of Northern Ecuador (1°S to 1°N) as inferred from chemical and isotopic composition 64

5.1 INTRODUCTION 64

5.2 GEODYNAMIC, GEOLOGICAL AND VOLCANOLOGICAL SETTINGS 66

5.2.1 Chiles-Cerro Negro Volcanic Complex 67
5.2.2 Chachimbiro Volcanic Complex and Cuicocha caldera 68
5.2.3 Chacana Caldera Complex 69
5.2.4 Quilotoa volcano 70

5.3 SAMPLING AND ANALYTICAL METHODS 71

5.4 RESULTS 72

5.4.1 Chemical composition of thermal waters 72
5.4.2 Chemical composition of gases 74
5.4.3 Isotopic composition of waters (δD, $\delta^{18}O$) and gases ($\delta^{13}C_{CO_2}$ and R/Ra) 76

5.5 DISCUSSION 77

5.5.1 Thermal water discharges 77
5.5.2 Gas discharges 78
5.5.3 R_H and T geoindicator 80

5.6 CONCLUSIONS 83

1 Introduction

1.1 RENEWABLE VS NON-RENEWABLE RESOURCES

The energy supply issue has always played an important role in the development of society, but with the advent of modern highly industrialized and technological realities this role has become strategic. The world's largest economies and the rapid ascent of developing countries need of affordable and reliable energy supply to plan long-term strategies for meeting social and economic growth objectives. By far the energy policies have been based almost entirely on non-renewable resources, mainly fossil fuels. Around 45% more oil, gas and coal is used today than twenty years ago (IEA, 2013a) and today fossil fuels meet more than 80% of total primary energy demand (IEA, 2015a). The current models of economic growth and development are affected by the availability of raw materials, their cost and their commercial use on the market. The conventional fuels such as oil, gas, coal and uranium in this respect offer clear advantages since they are abundant in many regions of the world, the technologies and exploitation techniques are proven and fully available, they have a high calorific value, they are tradable and their by-product are widely used in other manufacturing sectors. However, no doubt that this type of energy supply suffers from numerous weak points. First of all the availability of non-renewable energy resources will go running out in the future. The heavily dependence on continued access to fossil fuels greatly affects their consumption rate and depletion times of reserves (Shafiee and Topal, 2009). Furthermore most of the fossil fuels are still classified as resources and not yet as reserves, which means they are not fully characterised or are costly to extract, so they cannot be brought to the market (IEA, 2013a). Using advanced technology to move from resources to reserves may tend to make fossil fuels availability last longer but at present, the reserves of oil, gas and coal are expected will last a further 51, 53 and 114 years, respectively (British Petroleum, 2016). Another risk factor is the complex geopolitical contexts of oil and gas sector. The major production areas are historically characterized by political instability and diplomatic tensions that often result in armed conflicts as happened recently in Afghanistan, Iraq, Libya, Syria, Yemen, Russia and Ukraine. These scenarios have serious repercussion on production quotas, threaten the production, transportation and supply infrastructures and thus, ultimately, affect the sale price and the availability of hydrocarbons. As result oil and gas-importing countries could become a "hostage" of the exporting countries and the changing geopolitical situation, taking risk of energy crisis as in the past during the conflicts in Middle East in the 1970s.

Last but not least problem is the environmental impact. The production and supply chain of conventional fuels is highly risky. The potential hazards for hydrocarbon may manifest as crude oil spills at the

production site or during the transport to the consumer. For the nuclear sector the main challenges comes from the storage of radioactive waste or the release of radionuclides into the environment during the rare, but highly impactful accidents, at the nuclear power plants. On global scale the main concern comes from climatic change caused by the emission of greenhouse gases (GHG), predominantly carbon dioxide and methane. Suffice it to say that the energy sector alone represents roughly two-thirds of all anthropogenic greenhouse-gas emissions and over 90% of energy-related emissions are CO_2 from fossil fuel combustion (IEA, 2015a). Projection of long-term energy trends by the International Energy Agency in 2015 (New Policies Scenario: IEA, 2015b), outline an energy demand growth by nearly one-third between 2013 and 2040 driven, in the same period, by gross domestic product (GDP) growth at an average annual rate of 3.5% and by world population increase of 0.9% per year, from 7.1 to 9 billion of people. The same projection shows that growth in energy demand will continue to be met overwhelmingly by fossil fuels, with energy-related CO_2 emissions 16% higher by 2040. It seems clear that a model of economic growth fully dependent on fossil fuels poses serious problems concerning environmental impact and energy security, pointing out how necessary is a transformation of the energy sector toward a more efficient use and sustainable supply of energy.

This goal is even more urgent for low-middle-income countries which suffer the high prices of fossil fuels and cannot rely on alternative energy supply such as nuclear since they lack of technology and economic resources. These countries need access to modern, reliable, affordable and clean energy infrastructure to meet rising energy demands and support their economic development.

These challenges can be addressed by energy efficiency policies and increasing use of renewable and sustainable energies which are attractive for many reasons, including supply diversification, increased energy security, fostering new industries and skill diversification, reducing air and water pollution, and contributing to global efforts to reduce GHG emissions (ESMAP, 2012).

For some time the international community has moved concrete steps in order to achieve a more sustainable development. The Kyoto Protocol in the 1990s, the recent Paris Agreement (2015) and the UN's 2030 Agenda for Sustainable Development are a global effort to combat climate change and ensure access to modern energy services for all countries by encouraging the use of renewable energies. Since the introduction of sustainable energy policies, the global investment in clean energy continues to grow. Renewable energy sources have grown at an average annual rate of 2.2% in the period 1990-2014 and, in 2014, 13.8% of total primary energy supply was produced from renewable sources (IEA, 2016). In the near future low-carbon fuels will continue to increase as outlined in the New Policies Scenario where demand for energy from renewable sources grows by nearly 80% and its share to total primary energy reach 18% in 2035 (IEA, 2013b). Despite lower fossil-fuel prices, there were no signs of weakening appetite for renewables: for example in the electricity generation sector, renewables-based power production is estimated to have

increased by 128 GW in 2014 which amounted to more than 45% of world power generation capacity additions in 2014 (IEA, 2015a).

1.2 GEOTHERMAL ENERGY AS RENEWABLE RESOURCE

Geothermal energy is the heat stored in the earth's interior originated during the planetary accretion and formation and primarily, the heat produced through the constant decay of long-lived radioactive isotopes inside the rocks (Barbier, 2002), which moved to the surface through conductive and convective processes; in the crust, the temperature gradient is typically 30°C/km but can be as high as 150°C/km in hot geothermal areas (Gehringer and Loksha, 2012).

The amount of energy is huge and practically inexhaustible and it would take a small fraction of this heat to solve the energy supply problem. However tapping into this tremendous renewable energy reservoir is not an easy task from a technical and economic point of view (ESMAP, 2012), since it is unevenly distributed, seldom concentrated, and often at depths too great to be exploited industrially (Barbier, 2002). It is clear that geothermal energy can be economically exploited in geologically favorable contexts, characterized by active o recent volcanic and tectonic episodes, where a natural thermal engine provides a high heat flux. This natural engine triggers the convective circulation of the water contained in the overlying rocks which transfers the heat toward the surface (Marini, 2000). The amount of energy that could reasonably be extracted at costs competitive with other forms of energy constitutes what is called a geothermal resource (Muffler and Cataldi, 1978).

Geothermal resources have been classified according to their reservoir fluid temperatures so that we can distinguish between high (T>180°C), medium (100°C<T<180°C) and low (T<100°C) enthalpy resources. High enthalpy resources are suitable for power generation and often supply heat to combined heat and power plants. Medium enthalpy fluids are used for direct heating (for example, district heating and snow melting) and in several industrial and productive processes (for example, drying materials, fish farming, food production) and used for power production with the aid of binary turbines. Waters from low enthalpy resources are directly used for heating, and temperatures found at very shallow depths may be used to extract and store heat for heating and cooling by means of ground-source heat pumps (Sigfússon and Uihlein, 2015).

Geothermal energy is a renewable and sustainable energy because it draws from the huge heat stored within the earth that can be considered inexhaustible if compared to human timescale. Moreover, if we refer to a classic hydrothermal system, the groundwater transferring the heat toward the surface is replenished by precipitations in the recharge area which seep toward the reservoir through the fractures or the porous structure of the rocks. However the extraction of very large amounts of water for direct use or power production can compromise the availability of the resource if

the fluid extraction rate exceeds the reservoir replenishment rate. A long-term sustainable production relies upon an exhaustive model of the resource characteristic and a strategic positioning of production and re-injection wells to minimize the effects of pressure and temperature decrease. More than 95% of the fluid produced is often reinjected into the reservoir contributing to limit pressure losses and to replace at least part of the fluid extracted (Barbier, 2002). The extraction and re-injection processes should be frequently monitored by geochemical tracers, seismicity, reservoir pressure and temperature, micro-gravity and results from monitoring tools are then fed into geothermal system model which aid in planning the exploitation of the resource and predicting its behaviour in the future (Sigfússon and Uihlein, 2015).

From an environmental perspective, the greenhouse gas emissions of a geothermal power plant are much lower than those of fossil fuel-fired power plants, not to mention the reduction of emissions due to direct use of geothermal energy for heating and industrial processes. Geothermal plants emit approximately 5% of carbon dioxide, 1% of sulphur dioxide equivalents and less than 1% of nitrous oxide emitted by a coal power plant of equal size (Sigfússon and Uihlein, 2015). Anyway like any infrastructure development, geothermal installations have a social and environmental impact that have to be managed during the project preparation and development. The impacts are usually highly localized concerning hydrogen sulphide emissions from high enthalpy power plants and induced seismicity during reservoir stimulation with Enhanced Geothermal Systems (EGS; hydraulic fracturing of hot dry rocks) plants, unless seismicity can be also correlated with operations of hydrothermal power plants (Sigfússon and Uihlein, 2015).

Among renewable energies, geothermics is one of the most versatile because it can be used both for heating and power generation, provides an opportunity to be exploited by cascade utilisation (stepwise usage at progressively lower temperature) increasing the total efficiency and results in economic benefits (Sigfússon and Uihlein, 2015), is available continuously and is not affected by daily or seasonal variations compared to other renewable resources (e.g. solar or wind power). It is considered a base-load energy since it provide a stable and reliable power around the clock at a relatively low cost and with few operational or technological risks. As reported by Gehringer and Loksha (2012), once a geothermal power plant is operational, it will produce a steady output usually for several decades, at costs competitive with other base-load generation options, such as coal. Technological risks involved are relatively low because the geothermal power generation from hydrothermal resources is a mature technology. Levelized costs of generation are typically between US$ 0.04 and 0.10 per kWh (for medium sized plants around 50 MW), offering the potential for an economically attractive power operation.

Therefore geothermal energy has many attractive qualities stemming from its various forms of high, medium and low enthalpy largely distributed worldwide, many uses ranging from direct utilization of heat to low cost base-load power production and a mature technology in hydrothermal systems

sector and broad prospect of development in non-conventional geothermal resources such as the EGS. These characteristics make geothermal energy one of the most important in the panorama of renewable energies since that it has the potential to offer a strategic alternative to the energy supply diversification in the key of renewability and sustainability as well as ensure a lower dependency on the use of conventional fuels and reduce the environmental problems and the risk associated with geopolitical framework and price volatility.

1.3 GEOTHERMAL RESOURCES IN LATIN AMERICA

The best high enthalpy geothermal fields are generally found in tectonically and volcanically active areas where the heat flux is high. Geothermal resources have been identified in nearly 90 countries and more than 70 countries already have some experience utilizing geothermal energy (Gehringer and Loksha, 2012). Numerous countries worldwide possess a geothermal potential that could meet a substantial part of their energy demands. Anyway, unless the technologies for a commercially use of geothermal power are fully available and proven, the share of geothermoelectric production in the overall renewable power capacity is still quite small at about 0.7% (REN21, 2016). This factor is mostly related to the high upfront costs and the risk involved in exploration, especially in the drilling phase, making geothermal projects a risky investment less attractive than other types of energy resources for the stakeholders.

The countries located along the western active continental margin of Latin America, from Mexico to Tierra del Fuego, stand out among the other countries for the intense geodynamic processes which have created the ideal geological conditions for one of the major exploitation potential of geothermal energy of the entire planet. Anyway, unless some countries of Latin America such as Mexico, Costa Rica and Guatemala have already built geothermal power plants, the enormous geothermal potential of South America has not yet been exploited. In the last decades, numerous investigation and exploration programs have been carried out, but as of 2016 only one geothermal power plant, in the Apacheta geothermal field in Chile, has been approved and it is developing. For this reason is crucial to improve knowledge about resources endowments with the aim to identify the least risky projects that may attract new investment in the geothermoelectric sector.

This PhD thesis maintains a consistent focus on high-medium temperature hydrothermal resources exploitable for power production in geothermal areas of Ecuador and Chile through the study of the heat sources of hydrothermal systems and the thermal fluids discharged by the reservoir.

In Chapter 2, a briefly overview on different types of geothermal systems, exploration techniques, and exploitation technology is given.

In Chapter 3, the worldwide current utilization of geothermal resources for power production is discussed, with special emphasis to Ecuador and Chile.

In Chapter 4, thermobarometric applications are applied to amphiboles. Mineral analyses on crystal from Apacheta and La Torta geothermal concessions (Chile) and Chachimbiro geothermal area (Ecuador) are used to retrieve the pressure-temperature conditions during the crystallization of amphibole with the aim to constrain the depth of magma chambers that could represent the heat source for the geothermal systems.

In Chapter 5, geochemical technique, isotopic geochemistry and fluid geothermometry are applied to fluids discharged by thermal springs in geothermal areas of northern Ecuador.

2 Geothermal resources: an overview on systems, exploration, technology, environmental impact

2.1 DIFFERENT TYPES OF GEOTHERMAL SYSTEMS

The current commercially exploitable geothermal resource relies upon geothermal systems with availability of hydrothermal resources which consist of three natural main elements: a heat source, a reservoir and a fluid. As summarized by Sigfússon and Uihlein (2015), a geothermal system is called hydrothermal when a natural aquifer (fluid), usually with fracture permeability (reservoir), coincides with elevated temperatures in the crust (heat source, generally represented by a magmatic intrusion) and the energy stored in the reservoir is accessible since groundwater transfers the heat from rocks to the surface either through bore holes or natural cracks and faults (Fig. 2.1).

A large amount of geothermal resources have been identified in other types of geothermal systems which store or are able to produce, with artificial intervention, hot fluids or steam exploitable for direct utilization or power production. According to Saemundsson et al. (2009) we can distinguish:

Convective systems: the heat source is the hot crust at depth in tectonically active areas, with above average heat-flow. Here the geothermal water has circulated to considerable depth (> 1 km), through mostly vertical fractures, to mine the heat from the rocks.

Sedimentary geothermal systems: are found in many of the major sedimentary basins of the world. These systems owe their existence to the occurrence of permeable sedimentary layers at great depths (> 1 km) and above average geothermal gradients (> 30°C/km). These systems are conductive in nature rather than convective, even though fractures and faults play a role in some cases.

Geo-pressured systems: are analogous to geo-pressured oil and gas reservoirs where fluid caught in stratigraphic traps may have pressures close to lithostatic values. Such systems are generally fairly deep.

Hot dry rock (HDR) or enhanced geothermal systems (EGS): consist of volumes of rock that have been heated to useful temperatures by volcanism or abnormally high heat flow, but have low permeability or are virtually impermeable. Physical and chemical treatments are used to fracture the rocks creating permeability allowing the fluid to circulate throughout the fractured rock and to transport heat to the surface.

Shallow resources refer to the normal heat flux through near surface formations and the thermal energy stored in the rocks and warm groundwater systems near the surface of the Earth's crust. Heat is used directly and extracted with the aid of ground source heat pumps (home heating).

Another type of unconventional geothermal resource is hydrothermal fluids in supercritical conditions. Three high-temperature geothermal fields were selected

in Iceland as sites for deep drilling operation (Iceland Deep Drilling Project, IDDP) in order to reach natural fluid in supercritical conditions to a minimum depth of some 3.5–5 km, where temperature can be expected to range between 400 and 600 °C (Friðleifsson and Elders, 2005; Friðleifsson et al., 2014). With the exception of shallow resources, for which the recent developments in the application of ground source heat pumps have opened up a new dimension in their utilization, the other geothermal systems are still in development stage or under study. Anyway, with regard to HDR, they are much more widespread than hydrothermal resources and successful EGS have the potential to produce power and or heat on much larger scale than the hydrothermal resources.

2.2 EXPLORATION FOR GEOTHERMAL RESOURCES

Geothermal development is essentially a sequential and a systematic process of exploring of productive sites with the ultimate aim of geothermal power production. The development phases begin with reconnaissance and exploration, pre-feasibility, feasibility and finally power plant construction (Ochieng, 2013).

During the early stages of a geothermal project set up, a successful surface exploration could avoid unnecessary expenditure when the project enters in the development phase (Shah et al., 2015).

According to Shah et al. (2015), geothermal exploration is a multidisciplinary task which

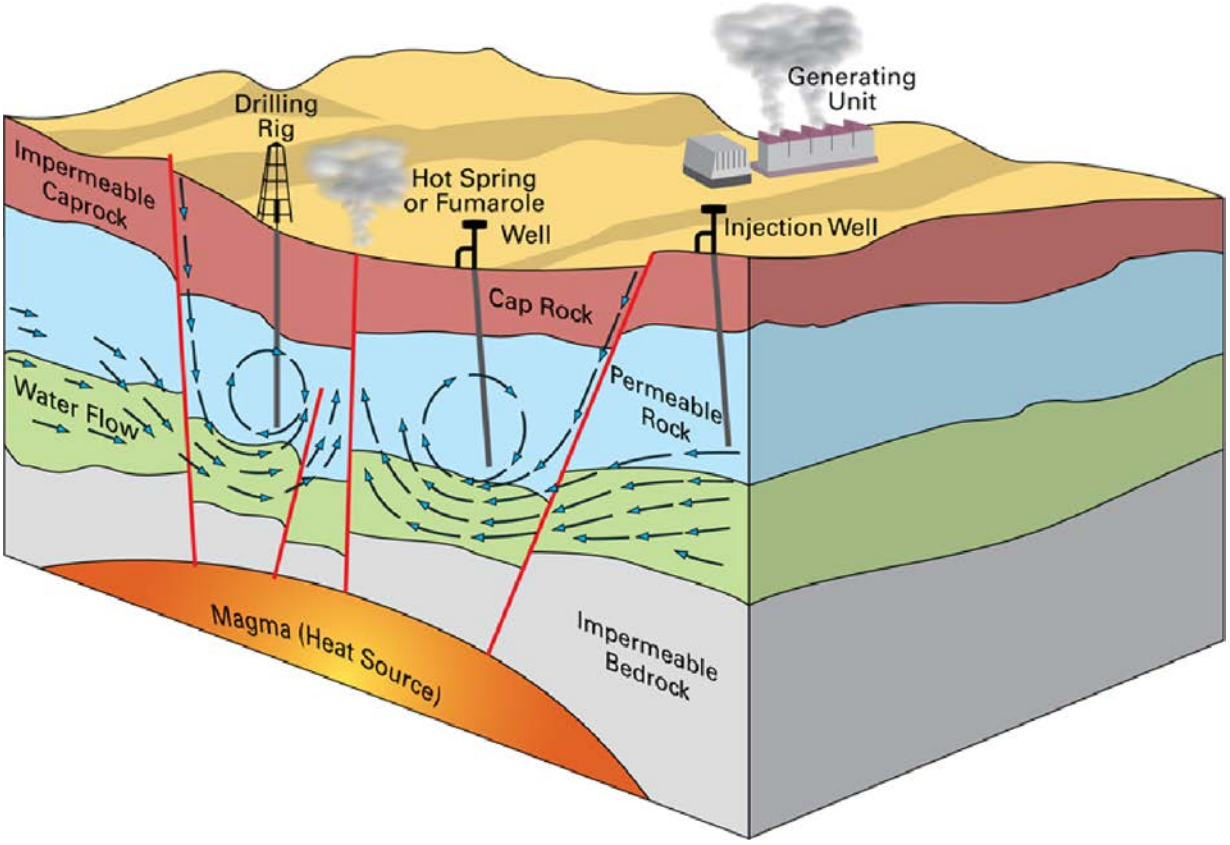

Fig. 2.1. Schematic view of an ideal geothermal system (source: http://www.bgs.ac.uk/research/energy/geothermal/).

entails activities like geological, geochemical and geophysical surveys. The main goal of exploration is to determine the existence of a geothermal resource and subsequently identify suitable drilling sites based on integrated data obtained by all exploration methods.

Geological survey is of paramount importance to provide information on the stratigraphic and structural framework of the area (Barbier, 2002). A preliminary mapping of the area is performed with the identification of the lithologic units and their chronological sequence, structural and tectonic setting and mapping of thermal surface manifestations. Petrological studies are performed to identify the types of rocks and structural mapping is done in the effort to distinguish the types of faults and fissures that transect the geothermal prospect and be able to discern the structural controls of the system (Ochieng, 2013). Many geothermal fields are related to past, recent or ongoing volcanism so that in cases of volcanic settings, the eruptive structures, the timing of events, the nature and volume of the erupted material have to be evaluated in order to understand the volcanological evolution that could offer insights into the present, unseen state of the deep formation (DiPippo, 2012). An exhaustive mapping of thermal manifestations is performed and the physical properties of surface manifestations are measured and recorded, including temperature, flow rate and conductivity (Árnason and Gíslason, 2009). Geological survey also makes use of remote sensing technique, that is satellites and/or airborne based multi-spectral or hyperspectral sensors used to detect natural electromagnetic radiation that is emitted or reflected by the terrestrial surface. These techniques are useful surveying tools for geological mapping, identification of thermal anomalies and recognition of hydrothermally altered products like sinter and tuff in prospective geothermal areas (Calvin et al., 2005). Contextually with geological studies is necessary to carry out a detailed hydrologic survey. The objective is to learn as much as possible about the fluids in the system, including their age, physical properties, abundance, flow paths, and recharge modes (DiPippo, 2012).

Geochemical survey plays a major role in preliminary prospecting of geothermal resources and it is an essential tool for monitoring the geothermal system during the exploitation phase. Furthermore, geochemical methods are relatively inexpensive when compared to geophysical survey therefore it is used in all stages of geothermal exploration and development. The major goals of geochemical exploration are to obtain the composition of geothermal fluids and use this to obtain information on temperature, origin and flow direction with the aim to localize the subsurface reservoir, interpret the subsurface conditions and the processes controlling the water chemistry and contribute to conceptual model of the geothermal system (Ármannsson, 2007). Geochemical studies of fluids involve sampling, analysis and data interpretation of water samples from hot spring, gas samples from fumaroles, bubbling gases from hot pools (Barbier, 2002).

The fundamental contribution of geochemistry to geothermal exploration is provided by interpretation of the behaviour

of conservative constituents and the use of geothermometers and isotopes. The knowledge of the origin of geothermal waters is important to discriminate their chemical properties and their source of recharge. As reported by Ármannsson, (2007), stable isotope ratios studies (especially ^{2}H and ^{18}O) and conservative constituents ratio (e.g. Cl and B) play an important role in hydrogeological investigation. The isotopes carry imprints of the origin of the waters and Cl and B ratio can be used to trace origin, mixing and flow of geothermal fluids. Similarly, the origins of geothermal gases can be traced through isotope ratio studies (e.g. ^{13}C in CO_2 and CH_4 and ^{34}S in H_2S). Geothermometry is the application of geochemistry to infer reservoir temperatures from the composition of geothermal fluids. Many reaction in geothermal systems are temperature dependent but their kinetics are not fast at lower temperature so that their equilibrium characteristics are preserved even though the waters rise to the surface and cool down (Ármannsson, 2007). Many chemical and isotopic geothermometers are used to estimate the aquifer temperatures beyond the zone of secondary processes like boiling, cooling and mixing on the basic assumptions that the sampled fluids are representative of the undisturbed aquifers where local equilibrium conditions are achieved (Ochieng, 2013). The most important and used geothermometers are based on temperature-dependent solubility of individual minerals (e.g. SiO_2), exchange reactions involving at least two minerals and the aqueous solution (e.g. Na-K, K-Mg, Na-K-Mg) and temperature-dependent fluid-mineral and gas-gas equilibria (Marini, 2000).

As reported by Manzella (1973), a geophysical exploration play a key role in geothermal exploration since it is direct at obtaining indirectly, from the surface or from shallow depth, the physical parameters of the geothermal system. Physical properties of the subsurface are variably affected by temperature gradient, porosity, saturation, salinity, faulting, and difference in the density and elastic properties of rocks. The presence of a geothermal system generally causes inhomogeneities in the physical properties of the subsurface, which can be observed as anomalies measurable from the surface. Thermal, seismic, gravity, electric, electromagnetic and magnetic surveys can be used to detect variations of subsurface characteristics, providing valuable information on the geometry (shape, size and depth) of the heat sources, reservoir and cap rock. It also aims at imaging structures that are responsible for the geothermal system, and delineating the areal extent of the geothermal resource (Ochieng, 2013). The following brief description of these methods, unless otherwise specified, is based on Barbier (2002):

Thermal survey: provides information on the thermal condition of the subsurface, the areal distribution of the heat flow and location and intensity of thermal anomalies. Soil temperature and heat flow measurements can often map hidden structures, such as faults or fissures which control flow of geothermal fluid (Ochieng, 2013).

Seismic survey: elastic properties of rocks influence the propagation velocity of seismic

waves. Interpretation of seismic information can provide data on the location of active faults that can channel hot fluids towards the surface and some indication of the location and physical characteristics of heat source.

Gravity survey: variations in the Earth's gravity field are caused by changes in the density of subsurface rocks. They give valuable information on the type of rocks at depth and their distribution and geometric characteristics. Positive gravity anomalies usually imply higher density values which are normally associated with plutonic intrusions and dykes while negative gravity anomalies implying lower densities values caused by higher porosities or by highly fractured parts of a rock and alteration minerals produced by circulation of hot water (Pipan, 2009).

Electrical-resistivity surveys: it quantifies how strongly a given material opposes the flow of electric current. Resistivity is largely affected by electrical conduction within waters occupying the pore spaces in the rock. Temperature and salinity of interstitial fluids tend to be higher in geothermal reservoirs than in the surrounding rocks. Consequently, the resistivity of geothermal reservoirs is generally relatively low. It is this contrast in resistivity between hot water-saturated rocks and the surrounding colder rocks that is used in resistivity surveys. This technique is based on injection of current into the ground and measurements of voltage differences produced as a consequence at the ground surface.

Electromagnetic survey: induction or electromagnetic methods are a tool for determining the electrical resistivity distribution in the subsurface by means of measurements of transient electric and magnetic fields. These methods are more suitable than the above-mentioned electrical-resistivity methods since it has a much deeper penetration into the ground, mitigating the screening effect of very resistive surface rocks. The electrical and magnetic fields are measured at several points and comparison between these fields allows to obtain the resistivities of the underlying formations. Magnetotelluric method use natural oscillations of the Earth's electromagnetic field due to interaction of the solar wind with the earth's magnetic field or interaction with electromagnetic signals originated during electric storm. Part of this low frequencies energy penetrates into the earth and is used to determine the resistivity structure of the sub-surface ranging from a few tens of meters to several hundreds of kilometres (Shah et al., 2015). Due to very low frequencies used in this method, it is often possible to achieve a penetration as great as 3–5 km with a reasonable degree of precision.

Magnetic survey: The Earth has a primary magnetic field which induces a magnetic response in certain minerals at and near the Earth's surface. By detecting spatial changes of the magnetic field, the variations in distribution of magnetic minerals may be deduced and related to geologic structure. In the exploration, magnetic measurements generally aim mainly at locating hidden intrusives and possibly estimating their depth, or at tracing individual buried dykes and faults. On the other hand circulation of hydrothermal fluids causes alterations in the rock which lead to a reduction of magnetic susceptibility as a consequence of the destruction of the magnetite contained in the

rocks (Ochieng, 2013). The magnetic method may also be used to constrain temperatures in the crust using the Curie isotherm (the temperatures at which minerals lose their magnetic properties) (Nabighian, 2005) and to confirm the existence of a hot rock (or near the melting point) mass in the crust (Lichoro, 2014).

2.3 STATE OF THE ART OF EXPLOITATION TECHNOLOGY

Hydrothermal resources of extractible hot water or steam are the most used geothermal resources for power production and their reservoirs are categorised as:

- liquid -dominated
- vapour-dominated

As reported by Barbier (2002) liquid-dominated reservoirs contain water in liquid phase and can be subdivided in *hot water reservoir* and *wet steam reservoir.* Hot water reservoir produces liquid at temperatures up to 100 °C which remain below the boiling point of water at any pressure. Impermeable cap-rocks may be not present. Wet steam reservoir contains pressurised water at temperatures exceeding 100 °C with little amount of steam, generally as discrete bubbles. Water represents the dominant phase and controls the pressure inside the reservoir. An impermeable cap-rock generally exists to prevent the fluid from escaping to the surface, thus keep in it under pressure. When fluid is brought to the surface and its pressure decrease, a fraction of the fluid is flashed into steam, while the greater part remains as boiling water.

Vapour-dominated reservoir produces dry saturated or superheated steam at pressure above atmospheric and are related to high-enthalpy resources. The steam is the continuous predominant phase, regulating the pressure in the reservoir. The presence of the cap-rock is of primary importance because prevents the leakage of fluids and keeps the system under pressure.

The following description of technological status and development of geothermal resources for power production is based on the *2014 JRC Geothermal Energy Status Report* written by Sigfússon and Uihlein (2015). Fluids production from a geothermal field are derived from oil and gas industry and conversion systems are based on traditional steam-electric power generation technology. A good understanding of the type and temperature of geothermal resources is of fundamental importance to determine the design of the power plants and to maximize the efficiency of converting fluid energy into electrical output. Geothermal power plants belong to the following categories:

- Direct dry steam
- Flash cycle and dual flash
- Binary

Direct dry steam technology (Fig. 2.2a) is used for exploitation of vapour-dominated resources. The steam from production wells (PW) is piped towards a particulate remover (PR) and moisture remover (MR) and finally transferred into the turbine attached to the generator (T/G). The exhausted steam

condenses in a condenser (C) and is then pumped (CP) towards the cooling tower (CT). The cooling fluid is recirculated by pumps (CWP) towards the condenser again or re-injected to the reservoir through re-injection wells (IW). The amount of non-condensable gases (mainly CO_2 and H_2S) is typically between 0.5-10% by weight of steam and requires a gas extraction system to be installed. Dry steam power plants reach efficiency of 50-70% (DiPippo, 2012), are commercially proven, simple to operate and require low capital costs and represent almost a quarter of geothermal power capacity today. However they are only suitable for dry steam reservoirs which are not common and unevenly distributed resources and almost all the known geothermal potential have already been put into operation.

The flash steam technology (Fig. 2.2b) makes use of liquid-dominated hydrothermal resources with a temperature above 180 °C. In the reservoir the liquid water boils, or "flashes" as pressure drops. The hot water or liquid-vapor mixture coming from the production wells (PW) flows through cyclone separators (CS), where the steam is separated from the liquid, and moisture remover (MR) before being directed towards the turbine and generator. The exhausted steam is condensed in a condenser (C) with the same flow path of dry steam power plants prior its discharge in re-injection wells (IW). In a single flash plant the separated water from the cyclone separators is pumped towards injection wells. The separated water may also be flashed in a flasher (F) (double-flash) (Fig. 2.2c) where additional steam is generated at lower pressure than the first flash. The single-flash and double-flash technology reach efficiencies between 30-35% and 35-45%, respectively when electricity is the sole product but overall efficiency is increased by producing hot water through heat-exchangers. Flash steam power plants are the most common type of geothermal power plants, making up about two thirds of geothermal installed capacity.

Binary cycles technology is able to use low- to medium-temperature resources which are more prevalent compared to high enthalpy fluids and today have an 11% share of the installed worldwide generating capacity and a 45% share in terms of numbers of plants (Bertani, 2012). Binary cycle power plants, employing organic rankine cycle (ORC) or a kalina cycle, operate at lower water temperatures of about 74-180 °C using the heat from the hot water to boil a working fluid, usually an organic compound with a low boiling point. In ORC plants (Fig. 2.2d), geothermal fluid is usually pumped from production wells (PW) towards an evaporator (E), and passes a pre-heater (PH) before it is pumped back into injection wells (IW). In the evaporator a preheated working fluid from a pre-heater is boiled prior to entering a turbine unit (T/G). The working fluid is condensed in a condenser (C) and pumped back (CP) to the pre-heater in a closed loop. Cooling water is pumped (CWP) from a cooling tower (CT) towards the condenser and make-up water (M) is pumped into the cooling tower to compensate for losses by evaporation. Kalina plants operate with a mixture of ammonia and water and the chemical composition of the working fluid is adjusted to the temperature of the geothermal fluid. In binary plants, the fluid

from production wells and the working fluid are kept separated during the whole process, so there are little or no air emissions. The ORC can reach efficiencies between 25% and 45% while the kalina cycle can operate up to efficiencies of 65% (Emerging Energy Research 2009).

2.3.1 Advanced power plants technology and unconventional geothermal resources

Today geothermoelectric production relies primarily on the availability of conventional geothermal resources such as hydrothermal systems, where hot water or steam extracted from a permeable, natural reservoir are converted into electricity by means of mature and widely applied technology that is direct dry steam, single or double flash and binary systems.

However the necessity to overcome some limitations intrinsic to the resource itself has led to the development of new strategies of exploitation and exploration. The main issue related to conventional resources (i.e. hydrothermal systems) concerns the limited distribution of natural permeable reservoir from which to extract high enthalpy hot fluids. Consequently the efficiency of the production facilities is often low since most of the resources have relatively low temperatures. Another critical point concerns the need to install the re-injection wells to balance the production rate of geofluids and the inflow toward the reservoir in order to maintain a long-term sustainability of the geothermal field. This result in higher costs of power plant installation since the drilling

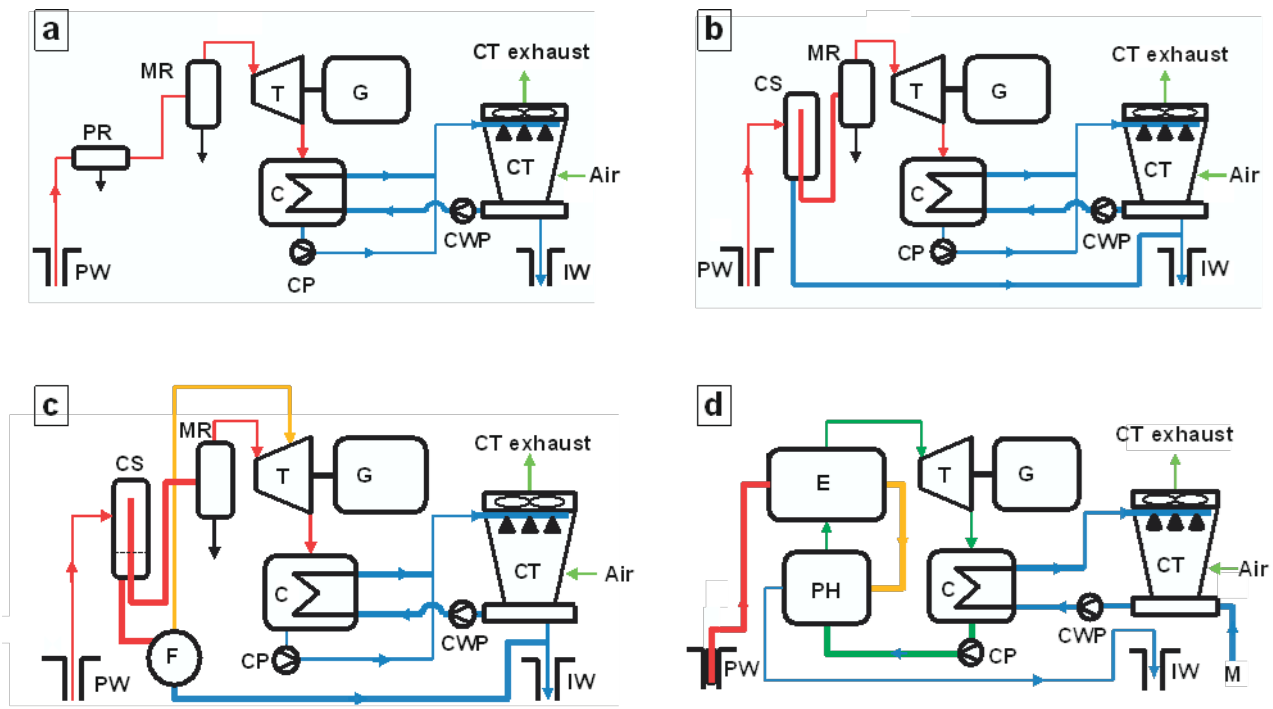

Fig. 2.2. Simplified flow diagrams for: a) direct steam geothermal power plant. b) single flash geothermal power plant. c) double flash geothermal power plant. d) organic rankine cycle (ORC) geothermal power plant. Red and yellow line: flow of hot geofluid toward the turbine and condenser or toward the pre-heater (ORC plant); blue line: path of the cooling fluid; green line: path of working fluid in ORC plant. See text for details and acronyms (modified from Sigfusson and Uihlein, 2015).

phase frequently constitutes more than 50% of the capital expenditure (Sigfússon and Uihlein, 2015). Furthermore, from an environmental point of view, the main issue is represented by emissions of hydrogen sulphide. Innovative approaches, concerning technological application to use in power plants to increase performance of geothermal energy utilization and the exploration of unconventional geothermal resources, have been conducted with the aim to improve the use of geothermal energy and to reduce the problems related to it.

2.3.1.1 Self-superheating (SSH) and combined-cycle power plants

The efficiency of geothermal plants have low values due to the low temperature of the steam, which is generally below 250°C, and results about three time lower than the efficiency of nuclear or fossil-fuelled plants (Barbier, 2002). As reported by Budiarto et al. (2014), the *self-superheating* (SSH) geothermal power plant is a modification of the geofluid pathway in the single and double flash cycles to increase the power output of the plant. In the SSH system the hot fluid at the wellhead is used, before entering the separator, to superheat the steam leaving the separator through a heat exchanger. In double flash type the self-superheating approach can be applied at each stage of the double flash cycle. In this design the saturated liquid leaving the first separator is brought to the second heat exchanger where it transfers its heat to the steam leaving the second separator (Mathieu-Potvin, 2013). In this way the temperature of the steam at the turbine inlet is higher than that for single or double flash type resulting in an increase of the specific output approximately 5% (Mathieu-Potvin, 2013).

Another option to increase the exergy of the resource to useful output is to use a combination of dry/wet steam and binary technology, called *combined cycle*. The heat from the low pressure steam coming out of the turbine (dry steam cycle) (Budiarto et al. 2014) or the heat from separated geothermal brine (wet steam cycle) are used to run a binary system (Sigfússon and Uihlein, 2015) to produce additional power prior to re-injection.

2.3.1.2 Hybrid systems and combined heat and power production (CHP)

Exploitation of geothermal energy can be enhanced integrating another resource into a geothermal power plant. This is referred to *hybrid systems*, where the steam originated from the geofluid can be superheated through any other source (e.g. biomass or coal) (Kagel, 2008). This combination offers the flexibility of determining the optimal steam temperature independently of the geothermal fluid temperature and increase efficiency, and therefore creates more electricity without expanding the use of the geothermal resource. Power plants in the order of 5 MWe could become conceivable even in areas with a relative low geothermal gradient (Kohl and Speck, 2004). A similar approach can be extended by connecting geothermal power plants to industries that produce waste heat, such as steel mills or waste incinerators, to enhance the temperature of the geofluid and increase

power production (Gehringer and Loksha, 2012).

Geothermal energy can be more efficiently exploited to produce both electricity and also for direct use purposes, in combined heat and power plants (CHP). The geothermal fluid, after being used for power production, can be exploited by cascading the residual heat to successively lower temperature applications including space or district heating, greenhouse heating, aquaculture pond and swimming poll heating (Lund and Chiasson, 2007). As a result the energy contained in the fluids is almost completely used (Gehringer and Loksha, 2012) and the economics of the entire system is improved (Lund and Chiasson, 2007).

2.3.1.3 Hot dry rocks and enhanced geothermal systems (EGS)

The exploration and exploitation of unconventional geothermal resources could further expand the diffusion and the benefits of geothermics. Hot dry rocks (HDR) are volumes of subsurface rocks abnormally heated but lacking of permeable fracture and circulating natural fluid which can be exploited through hydraulic fracturing. As reported by Sigfússon and Uihlein, (2015), the basic concept is to drill two wells into a hot dry rock with limited permeability and fluid content to create permeability in the rock by hydro-fracturing the reservoir with cold water pumped into the first well (the injection well) at high pressure. The second well (the production well) intersects the stimulated fracture system and returns the hot water to the surface where electricity can be generated. This technical solution is known as enhanced geothermal systems (EGS) (Fig. 2.3). Adoption of flash or binary technologies may be used with EGS depending on the temperature of geothermal fluid extracted from the artificial reservoir created by hydraulic stimulation.

EGS technologies have the potential to produce large amounts of electricity almost anywhere in the world since temperatures of 150°C can be found at depth of 5 km in areas with normal geothermal gradient of 30-35°C/km. Thus any convenient volume of hot dry rock in the earth's crust, at accessible depth, can become an artificial reservoir (Barbier, 2002). At the moment, several pilot projects are being conducted in Australia, Europe, Japan and the US (Sigfússon and Uihlein, 2015). One of these pilot geothermal power plants has been built by a French-Germany industrial consortium in Soultz, France. Three 5 km-depth boreholes (two production wells and one re-injection well) have been drilled and stimulated by hydraulic and chemical methods. On surface, an ORC binary power plant with a net capacity of 1.5 MWe has been installed and put into operation in 2008 (Genter et al., 2010).

However the experimental projects carried out so far demonstrate that there are some significant problems in energy production with the EGS system and the commercially viability of the technology has not been successfully proven yet (Gehringer and Loksha, 2012). As reported by Barla (2008), the hydraulic fracturing in HDR systems must be pushed at a considerable distance from the injection well, in order to create continuous and stable fractures in the rock through which fluids can circulate with sufficient flow rate extracting heat from the

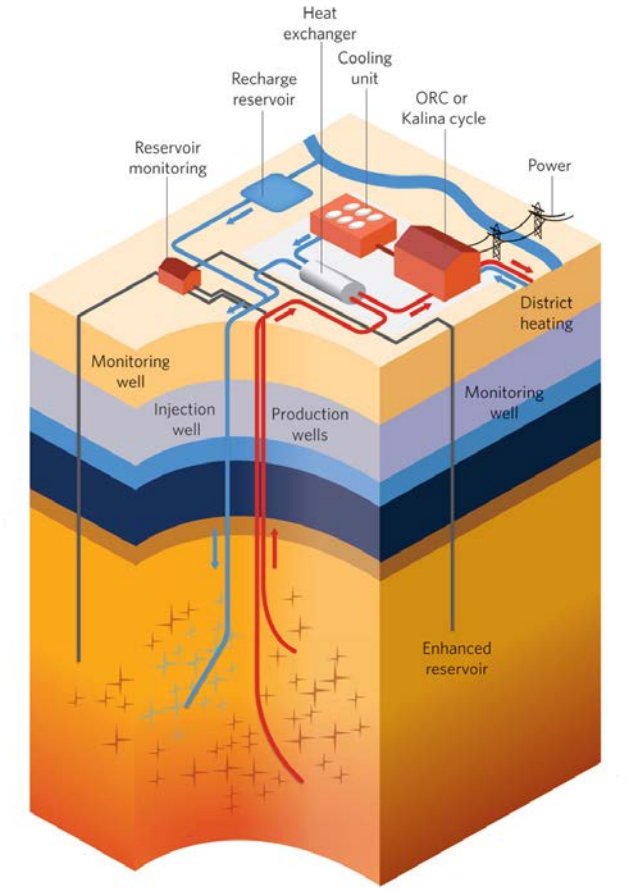

Fig. 2.3. Schematic view of HDR-EGS system (source: http://lifefreeenergy.com/g/geothermal-energy-home.html).

surrounding rocks. This implies that high pressures have to be applied to increase and maintain permeability with the risk of induced seismicity. Loss of circulating water, progressive scaling of underground fluid pathway, and the limited heat capacity of the artificial reservoir, represent other issues related to EGS systems. Moreover, as well as conventional hydrothermal resources, the geothermal fluids should be treated and re-injected underground because of its polluting properties. These operations entail high economic costs since they require the drilling and maintenance of additional wells, the treatment and the pumping of the fluids (Alimonti and Soldo, 2016). Furthermore, from an economic point of view, experts agree that the following key parameters, representing the lower end of the range for each, are required for a commercially-viable HDR reservoir: production flow rate 50-75 kg/s, effective heat transfer area >2 million square meters, rock volume accessed >200 million cubic meters and flow losses (% of injection flow) <10% (Garnish et al., 1992).

2.3.1.4 Closed-Loop Geothermal Wells

An innovative approach to overcome the limitations associated with EGS systems consists in positioning to a proper depth a closed loop heat exchanger to mine heat from the hot rocks. As reported by (Riahi et al., 2017) this systems works with a pressurized working fluid injected from the surface into a coaxial-designed wellbore. The fluid flows downward through the outer tube extracting heat from the surrounding hot rocks and rises upward through the thermally insulated inner tube. In closed-loop system, compared with traditional EGS application, no geothermal fluids production take place and there is no contact between the working fluid and rock formation. Consequently, the hydraulic fracturing is not requested thus mitigating the risk of induced seismicity, and pipe corrosion due to aggressive fluids, scaling of fluid pathway due to minerals precipitation or release to the atmosphere of pollutants from the artificial reservoir, are also avoided.

A virtual-modelled pilot project of a 1 MWe binary power plant was tested with good results in Italy (Santucci, 2013) while a successful demonstration of the world's first

New Geothermal Power system was carried out in Kokonoe, Japan, in October 2016 (Kyoto University, 2016).

2.3.1.5 Coproduction of geothermal and Oil/Gas and geo-pressured geothermal systems

Heated water is a natural byproduct of oilfield production processes that has long been considered unusable (Blodgett, 2014). Field operators in oil and gas industry need to handle hot fluid with pumping and reinjection and this operation requires extra cost (Budiarto, 2014). The idea behind the coproduction is that the hot water, upon separation from the hydrocarbons in a separator located on the surface, would pass through a binary power plant then disposed of or used for other purposes (Milliken, 2007). The potential for power production from oil fields is substantial. By considering only the United States, there are 823,000 oil and gas wells that co-produce hot water concurrent to the oil and gas production; this equates to approximately 25 billion barrels annually of water which could be used as fuel to produce up to 3 GW of clean power (ElectraTherm, 2012). In the United States, at the Rocky Mountain Oil Test Center, Wyoming, geothermal company Ormat Technologies built a successful 0.25 MW coproduction demo unit which first ran in 2008 (Blodgett, 2014).
Moreover, there are currently many oil and gas wells which are neglected or abandoned (Budiarto, 2014). These wells are either deep enough to encounter hot water, or could be deepened into hot zones (Kagel, 2008). Geothermal heat could be extracted from them by using WellBore Heat Exchangers (WBHX) in which a heat carrier fluid circulate in a closed loop, in a similar way to what happens in closed-loop geothermal wells (cap. 2.3.1.4). An example of this application was carried out by Alimonti and Soldo (2016) who evaluated the implementation of the WBHX on the Villafortuna Trecate oilfields in Italy, one of the largest European oil fields in which only 8 wells are still producing against 50 wells drilled. The authors developed a model of heat extraction from a reservoir between 5800 and 6100 m depth with temperature of about 160-170 °C. They set up a simulation of WBHX considering two different heat transfer fluids (water and diathermic oil) and established that optimum condition is obtained with water at a flowrate of 15 m^3/h. The thermal power output is 1.5 MW and the net electrical power, generated through an ORC binary plant, is 134 kW (Fig. 2.4). Another example in this regard was proposed by Wight and Bennet (2015). The authors evaluated the electricity generation via a binary cycle power plants using water as circulating fluid and abandoned oil fields wellbore as a heat exchanger. They established that a power of 109 kW could be generated using a wellbore depth of 4200 m with a mass flow rate of 2.5 kg/s and a given geothermal gradient of 0.0311 °C/m. Well abandonment at present remains the final outcome for every oil and gas well drilled so that they could represent a significant source of renewable energy (Wright and Bennet, 2015). Furthermore the use of abandoned oil wells has many advantages ranging from economic to environmental point of view. Dismissing oil fields costs are reduced and economic

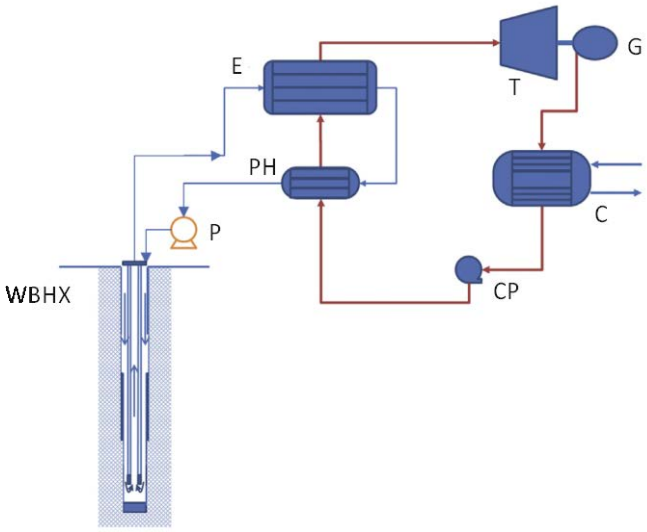

Fig. 2.4. Simplified schematic explanation of WellBore Heat eXchanger (WBHX) and associated ORC power plant. P and CP=pumps; E=evaporator; T=turbine; G=generator; C=condenser (Alimonti and Soldo, 2016).

feasibility of the geothermal plant are improved, since drilling cost are avoided, while environmental impact is reduced since no geothermal fluids production take place (Alimonti and Soldo, 2016).

Some sedimentary basins contain sedimentary rocks with pore pressure exceeding the normal hydrostatic pressure gradient. These systems are classified as geo-pressured geothermal systems. They are confined and analogous to geo-pressured oil and gas reservoirs where fluid caught in stratigraphic traps may have pressures close to lithostatic values. The known geo-pressure systems are found in conjunction with oil exploration (Saemundsson et al., 2009) and the most intensively explored geo-pressured geothermal sedimentary basin is in the northern part of the Gulf of Mexico and in Europe in Hungary. According to DiPippo (2012), the main properties of these systems are high pressure, high temperature and dissolve methane. These characteristics make them attractive for geothermal exploitation allowing the use of mechanical energy stored in the form of high pressure and thermal energy. Furthermore, dissolved natural gases can be extracted and used for further power production or for sale to enhance the economics of a development project. The geopressured formations in the Gulf of Mexico (especially Texas and Louisiana) are estimated to hold tens of thousands of megawatts of geothermal energy, and a hundred year supply of natural gas for the United States (Muffler, 1979). As reported by Taylor (2007), one major test of this technology has been carried-out at the Pleasant Bayou site, near Houston, United States, where a demonstration 1MW binary power plant powered by a geopressured system and extracted natural gas, was put into operation from January to May of 1990 (Campbell, 2006). Anyway, despite the advantage of being able to co-produce natural gases and electricity through geothermal resource, geopressured fields have not yet been completely explored and the resource has yet to achieve commercial status (DiPippo, 2012).

2.3.1.6 Supercritical fluids and magmatic systems

When a fluid reaches a temperature and pressure higher than its critical point, its behaviour became supercritical and the distinction between the liquid and the vapour phases disappears. Pure water passes into its supercritical behaviour at temperature of 373.95 °C and pressure of 22.064 MPa (Pioro and Mokry, 2011). Temperatures in the

immediate vicinity of magmatic intrusions exceed the critical temperature of water, implying the possible occurrence of geothermal water as a single-phase, supercritical fluid (Scott et al., 2015).

These supercritical geothermal resources may be very useful for power production since thermodynamic constrains indicate that an aqueous hydrothermal fluid at supercritical conditions with a temperature of 400 °C and a pressure of 25 MPa has more than five times the power-producing potential of liquid water at a temperature of 225 °C (Tester et al., 2007).

These kinds of resources are being actually investigated by Iceland Deep Drilling Project (IDDP). This is a long-term program to improve the economics of geothermal energy by producing supercritical hydrous fluids from drillable depths. Producing supercritical fluids will require the drilling of wells and the sampling of fluids and rocks to depths of 3.5–5 km, and at temperatures of 450–600 °C (Friðleifsson and Elders, 2005; Friðleifsson et al., 2014). Three geothermal fields, Krafla, Hengill (Nesjavellir) and Reykjanes, were selected as being the most suitable to drill deeper to develop supercritical geothermal resources (Friðleifsson et al.,2003). In 2009, the first drilled well at Krafla, in north-east Iceland failed to reach its target as drilling had to be terminated at a depth of only 2.1km when magma unexpectedly entered the borehole (Hólmgeirsson et al., 2010; Pálsson et al., 2014). Conversely, the drilling of second well, at the Reykjanes Peninsula, was successfully completed on January 2017. Temperature at the bottom of the well has already been measured at 427°C, with fluid pressure of 340 bars making it clear that the bottom of the well reached fluids at supercritical conditions (http://iddp.is/). A deep well producing from a reservoir with a temperature significantly above 450 °C might, under favorable conditions, yield enough high-enthalpy steam to generate 40 - 50 MW of electric power. This exceeds, by an order of magnitude, the power typically obtained from a conventional geothermal well (Friðleifsson, 2003). As reported by Elders et al. (2014), the potential advantages of exploitation of supercritical geothermal resources are a general improvement in the economics of geothermal power production with increase ratio of drilling costs to power output per well and increase in the power output of existing geothermal fields without increasing their environmental footprints. Significant benefits in the life time of existing geothermal fields are also obtained by increasing the size of the producible resource by extending it downwards.

The thermal energy stored in magma bodies, relatively close to the surface of the Earth, represents a huge potential resource that could be directly tapped and exploited (Barbier, 2002). According to DiPippo (2012), the concept is to drill a well until reach the magma, insert an injection pipe and pump down cold water at high pressure. The thermal stress induced by the contact between cold water and magma will induce cracking of the solidifying rock, making it permeable. If the water can be made to return to the surface by passing upward through the cracked, extremely hot glassy material, it would reach the surface hot and ready for use in a binary power plant. Two research projects were conducted by the U.S. Department of Energy in the 1970s and

1980s. The first one was carried out at the lava lake within the crater of Kilauea Iki, Hawaii (Hardee et al., 1981). It succeeded in drilling to the molten lava and several experiments were run to understand the mechanism of energy extraction from a lava body. The second project took place at Long Valley caldera in Central California with the aim to better understand the existence and behaviour of large magma bodies within calderas (Chu et al., 1990) but it was suspended for lack of funds. Anyway it produced scientific information that led to a better understanding of the Long Valley caldera.

2.3.2 Direct Use

The following discussion is taken from Sigfússon and Uihlein (2015).

Direct use is the oldest form of geothermal energy exploitation by mankind (Gudmundsson, 1985) and it is used for various purpouse: space and district heating, greenhouse heating, aquaculture pond heating, agricultural drying, industrial uses, cooling, snow melting, bathing and swimming (Lund, 2011). Most of the direct uses of geothermal energy occur with the exploitation of fluids with temperatures below 150 °C (Blanco Ilzarbe et al. 2013). Advantages of direct use are a widespread resource available at economic drilling depths and the use of conventional well drilling, heating and cooling equipment (Lund 2009).

A basic direct use system consists in heat exchanger that extracts the heat from the geothermal fluid and transfer it to a secondary clean fluid which carries the heat to the user as the geothermal fluid usually is unsuitable for direct use due to fluid chemistry (Karlsson and Ragnarsson 1995) (Fig. 2.5). The main components of a direct use system are the down hole and circulation pumps, pipelines, and the heat extraction and exchange parts (Lund 1998).

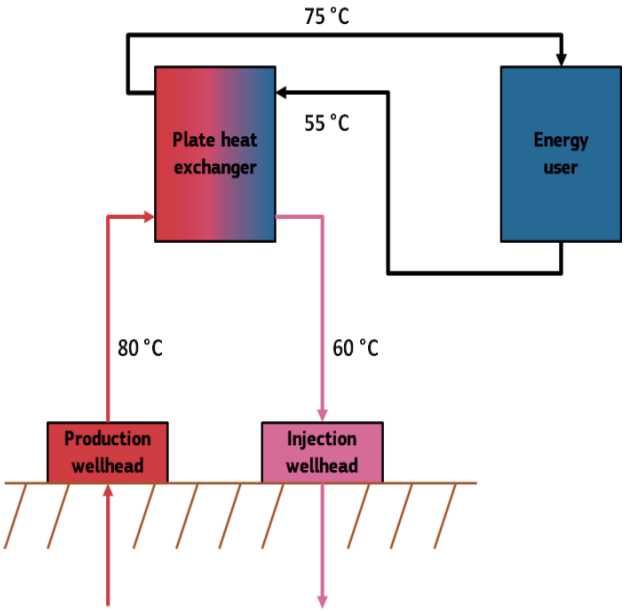

Fig. 2.5. Schematic process flow diagram for a direct use system with heat exchanger (Sigfússon and Uihlein, 2015).

A technology that is expanding very quickly is the ground source heat pumps (GSHP). They use shallow geothermal energy which is available almost everywhere converting the low temperature geothermal energy of the ground to thermal energy at a higher temperature which can be used for space or water heating (Ochsner 2008). Usually, a refrigerant is used as the working fluid in a closed cycle (Self et al. 2013) and electric energy is used to drive the compressor (Fig. 9). The GSHP can be used with other energy sources, such as solar thermal collectors, whose energy can be added to the GSHP's ground loop to increase efficiency of the

system. The installed capacity of GSHP has seen a dramatic increase with annual growth rates of 10 % since 1994 with a main focus on Europe and the United States (Self et al. 2013).

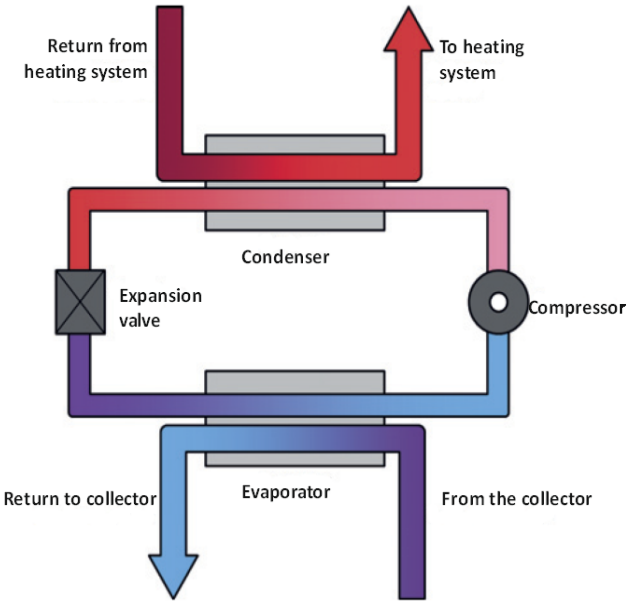

Fig. 2.6. Schematic process flow diagram for a ground source heat pump system (Sigfússon and Uihlein, 2015).

According to REN21 (2016), geothermal heat represents the 2% share of modern renewable heat generation and account for one-half of total final geothermal output (75 TWh). Over the past few years, direct use of geothermal heat, excluding heat pumps, has grown by over 3% annually on average, with geothermal space heating growing around 7% annually. China, Turkey, Japan and Iceland lead in terms of heat energy generated by direct use of geothermal.

2.4 ENVIRONMENTAL IMPACT

Local environmental impacts from geothermal power replacing the use of fossil fuels also tend to be positive on balance, due to avoided impacts of fuel combustion on air quality, the hazards of fuel transportation and handling. Nevertheless, like any infrastructure development, geothermal power has its own environmental impacts and risks that have to be assessed, mitigated, and managed (Gehringer and Loksha, 2012).
The environmental impact of geothermal activities has been classified by Mannvit hf (2013):

Surface disturbance (access roads, pipe and power lines, land use);
Physical effects (effect of fluid withdrawal on surface manifestations, land subsidence, induced seismicity, visual effects due to structures);
Noise (during drilling, construction and operation);
Thermal pollution (hot liquids and steam released from discharging boreholes and the power plant);
Chemical pollution (disposal of liquids and solid waste, gaseous emissions);
Impact on protected faunas and floras;

The most relevant environmental impact arises during plant operation. Geothermal fluids usually contain gases, such as CO_2, H_2S, NH_3, and CH_4 (called non-condensable gases, NCG), which can contribute to global warming, acid rain or noxious smell if released into the atmosphere (Gehringer and Loksha, 2012). Flash and direct steam power plants direct the geothermal fluids through

the turbines and gases are extracted from condensers. Conversely, binary power plants direct the geothermal fluids in a closed loop through heat exchangers prior to re-injection therefore facilitating nearly emission free operation Sigfússon and Uihlein (2015). Although CO_2 constitutes 90% of the NCG (Bertani and Thain, 2002), emissions from geothermal power generation, while not exactly zero, are far lower than those produced by power generation based on burning fossil fuels. Data from 85 geothermal plants, representing 85 percent of global geothermal capacity in 2001, indicate a weighted average of CO_2 emissions of 122 g/kWh (Friðleifsson et al., 2008).

Of the gases emitted from high temperature power plants, H_2S is of primary concern due to its toxicity and because it may constitute a large share of emission (up to 20-35 vol % of NCG) Sigfússon and Uihlein (2015). Although is not present in every geothermal resource, mercury may be emitted during power production both in gaseous and in particulate form.

As reported by Gehringer and Loksha (2012) discharge of waste fluids is also a potential source of chemical pollution. After having passed the turbine, geothermal fluids with high concentrations of chemicals, such as sodium chloride (NaCl), boron (B), fluoride (F), or heavy metals such as mercury (Hg) and arsenic (As), should either be treated or reinjected into the reservoir. Fluids coming from low to medium temperature geothermal fields, as used in most direct-use applications, generally contain low levels of chemicals. Furthermore the pollution it is not only limited to the chemical composition of waters but also to the residual heat. Waste water from cooling towers has a higher temperature than ambient water, therefore constituting a potential thermal pollutant when discharged to nearby streams or lakes.

The withdrawal and/or reinjection of geothermal fluids may cause ground subsidence at the surface. In certain areas, this may trigger or increase the frequency of micro seismic events, unless the distinction between induced seismicity and natural seismicity is not easy in hydrothermal fields Sigfússon and Uihlein (2015). The induced seismicity is primarily associated to EGS due to the use of rocks fracturing techniques to create the artificial reservoir and earthquake up to M 3.4 were detected in Basel (Deichmann and Giardini 2009, Zang et al. 2014)

3 Current status of power production from geothermal resources

3.1 THE WORLD SCENARIO

The exploitable geothermal energy potential in several parts of the world is far greater than the current utilization and geothermal power has an important role to play within the energy systems of many countries since that it can deliver a clean, reliable and locally produced baseload power. It has been estimated that nearly 40 countries worldwide possess enough geothermal potential that could, from a purely technical perspective, satisfy their entire electricity demand. Geothermal resources have been identified in nearly 90 countries and more than 70 countries already have some experience utilizing geothermal energy (Gehringer and Loksha, 2012). Currently, electricity from geothermal energy is produced in 23 countries (Bertani, 2015) (Fig. 3.1) but, as of 2011, only 0.3 percent of the world's total power generation come from geothermal resources (ESMPA, 2012) and, also when compared with other renewable energy sources, the share of geothermoelectric production in the overall renewable power capacity represents only 0.7% of the total (REN21, 2016). The underutilization of geothermal resources can be explained by considering that the current commercially available geothermal power technology relies upon the availability of hydrothermal resources (i.e. underground sources of extractible hot fluids or steam) to energize the power plant and estimates are that geothermal resources, in the form of hot steam or fluids, are only available on 1/4 to 1/3 of the planet's surface (Gehringer and Loksha, 2012). Other issues are related to high upfront investments needed for the pre-survey, exploration and test drilling phases and to high resource risks at initial stages of development of a geothermal project (Fig. 3.2).

However, even if slowly, the use of geothermal resources has been growing for decades (Fig. 3.3). Short term forecast highlights a power capacity increase by 70%

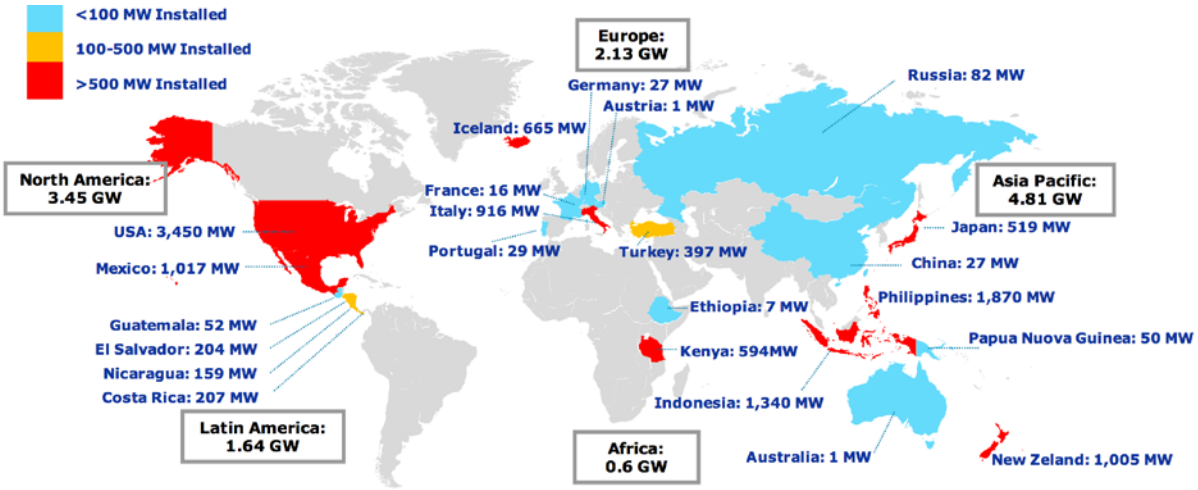

Fig. 3.1. Installed capacity (GWe) in 2015 worldwide from geothermal resources (Bertani, 2015).

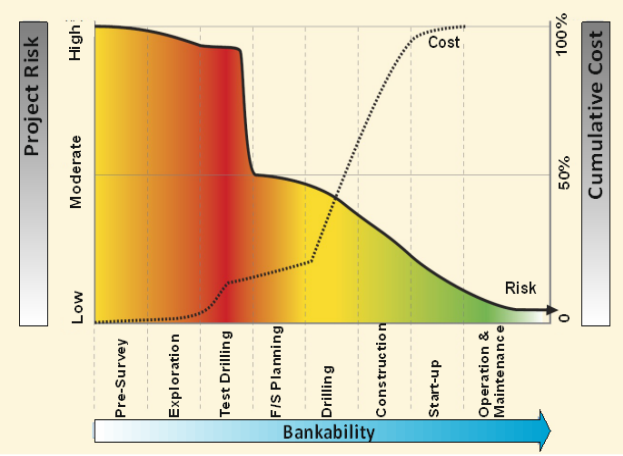

Fig. 3.2. Cumulative cost and risk profile at various stages of development of geothermal project (Gehringer and Loksha, 2012).

to 2020 (Bertani, 2015) (Fig. 3.3) and the share of geothermal power in the overall energy balance of the world is expected to grow to 0.5% by 2030 in the International Energy Agency's conservative Current Policies Scenario or to about 1.0% in the aggressive 450 Scenario (Gehringer and Loksha, 2012). As of 2015 the global total of geothermal power has been estimate to be 13.2 GW with about 315 MW of new geothermal power completed in 2015 (+2.3% compared to 2014) (REN21, 2016). The United States and Philippines have the biggest installed capacity of geothermal power plants, 3,450 MW and 1,870 MW, respectively (Fig. 3.1) and countries that added capacity during the year 2015 were Turkey, the United States, Mexico, Kenya, Japan and Germany (REN21, 2016).

With sufficient investment in drilling and improved knowledge about resource endowmnents, geothermal energy could have a much larger role in Central and South America, the Caribbean, East Africa and Southeast Asia (ESMPA, 2012). The unexpressed potential of geothermal resources in America Latina is a striking example. Central and South America countries, especially the western regions, are located along an active convergent plate margin characterized by Quaternary volcanism which ensures the presence of diffuse heat flow anomalies.

Geothermal exploration in Latin America started with the study and exploration of the El Tatio area in Chile in the'20s (Tocchi, 1923), but it is only since the '70s and '80s that the governments of the main countries in the Region started an extensive campaign of investigation in search of geothermal resources. Mexico was the first country to generate electricity from geothermal sources in 1973 then El Salvador in 1975, which were followed by Nicaragua in 1983 and Costa Rica and Guatemala in the '90s. As of 2015 the geothermoelectric capacity in Latin America is 1,629 MW but it represents just 13% of global electric power generation from geothermal resources and moreover it is generated only in Central America since that do not exist operating geothermal power plants in South America (Bona and Coviello, 2016).

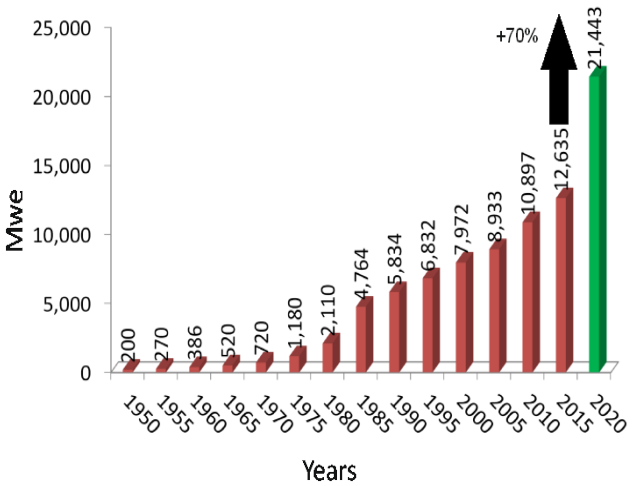

Fig. 3.3. Installed capacity (MWe) from 1950 up to 2015 (modified from Bertani, 2015).

3.2 GEOTHERMAL RESOURCES IN CHILE

Early geothermal exploration in Chile began in '20s with drilling of the El Tatio geothermal field (Tocchi, 1923). At the end of '60s a new program of geologic, geophysical and geochemical investigation was carried out by the Chilean Development Corporation (Corporación de Fomento de la Producción, CORFO) and the United Nations Development Program (UNDP) (Lahsen, 1976). Between the '70s and the '80s numerous exploration, drilling and feasibility studies have been conducted (Lahsen 1988; Hauser, 1997; Peréz, 1999) until closure of exploration programs in 1982. By early 2000, a new impulse was given by the enactment of a law providing the framework for the exploration and development of geothermal energy in Chile.

The high-temperature areas in Chile are located along the Andean Cordillera in close spatial relationship with active volcanism which is primarily controlled by the convergence of the Nazca and South American Plates. The main geothermal systems occur in the extreme northern (17-28 °S) and central-southern part (33-46 °S) of Chile (Fig. 3.4). Flat slab geometry of subducting oceanic crust generates areas of volcanic gaps (Barazangi and Isacks, 1976) (28-33 °S and 46-48 °S) where thermal manifestation, as well as in the Coastal Range, are scarce and their temperature are usually lower than 30 °S (Lahsen et al., 2010).

In the country there are more than 300 geothermal areas associated with Quaternary volcanism. As reported by Lahsen et al. (2015a), the Northern Chile Geothermal Zone

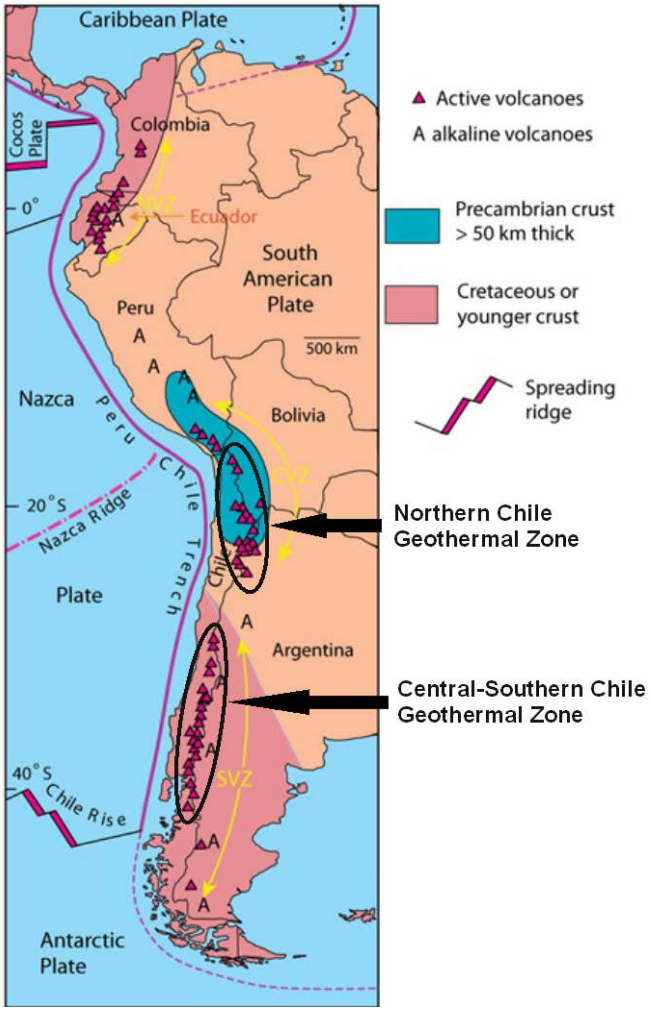

Fig. 3.4. Quaternary volcanic zones of South America controlled by subduction of Nazca Plate and Antartic Plate beneath South American Plate. The volcanic arc is subdivided in Northern (NVZ), Central (CVZ) and Southern Volcanic Zone (SVZ) (modified from Thorpe and Francis, 1979; Thorpe et al., 1984).

(Fig. 3.5a) has about 90 hot-spring areas (Hauser, 1997) and 45 exploration concessions are being surveyed; the most advanced exploration programs have been conducted in the Colpitas, Apacheta, Pampa Lirima and El Tatio-La Torta geothermal prospects (e.g. Urzúa et al., 2002; Aguirre et al., 2011; Sofia and Clavero, 2010). Exploratory wells have been drilled in all of

these areas, and the estimated combined power potential of exploitable geothermal energy of these four prospects is between 400 and 1,000 MWe. There are currently 3 geothermal systems in the country with available measured wellhead resource values: Apacheta (9 MWe); El Tatio (23 MWe); and Tolhuaca (13 MWe) (Aravena et al., 2016). These wells yield a total confirmed power potential of 45 MWe (Aravena et al., 2016). Exploitation concessions have been granted for the Apacheta and El Tatio geothermal fields and the environmental assessment for the installation of a 50 MWe power plant has been approved for the Apacheta field.

In the Central-Southern Zone (Fig. 3.5b) there are about 200 hot-spring areas (Hauser, 1997), and 31 exploration concessions have been granted; the most advanced exploration studies have been completed at the Tinguiririca, Calabozos, Laguna del Maule, Chillán and Tolhuaca geothermal areas (e.g., Clavero et al., 2011; Sofia and Clavero, 2010; Melosh et al., 2010, 2012; Hickson et al., 2011). Exploratory wells have been drilled in these prospects and the estimated combined power potential for the five areas ranges from 650 to 950 MWe. Exploitation concessions were granted for the Laguna del Maule (Mariposa) and Tolhuaca (San Gregorio) projects, where production size wells have been drilled.

3.2.1 The Apacheta Geothermal project

The Apacheta geothermal fields is located in the Antofagasta Region, Northern Chile about 100 km NE from city of Calama, at about 4500 meters a.s.l. The geothermal system is

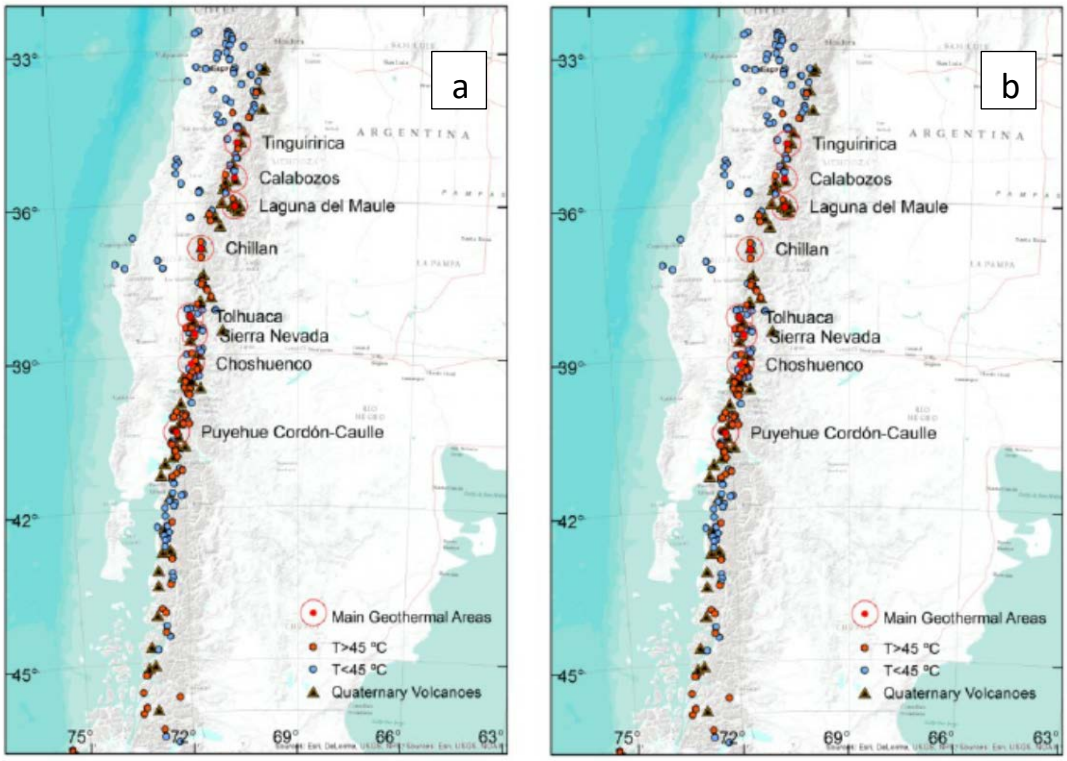

Fig. 3.5. Geothermal prospect of a) Northern Chile and b) Central- Southern Chile (Lahsen et al., 2015b)

build up upon a large zone of silicic volcanism occupying the 21°-24° south segment of the Andean Central Volcanic Zone (AVCZ; de Silva, 1989; de Silva et al., 1994) and it is hosted by a 3 to 5 km wide NW tranding graben nesting the Pliocene-Pleistocene lavas and pyroclastic products of Apacheta-Aguilucho Volcanic Complex (AAVC).

The Chilean mining company CODELCO discovered the geothermal field in 1999, during a shallow water exploration well (Salgado and Raasch, 2002). MT and TDEM survey detected a low resistivity boundary (<10 ohm-m) extending over an area of 25 km^2 and geochemical survey indicated reservoir temperature of 250-260 °C (Urzua et al., 2002) (Fig. 3.6a, b). Temperature >200 °C was successively measured at depth > 500 m in a 550 m-deep core-hole carried out by the Empresa Nacional de Geotermia in October 2007. Four commercial-diameter exploratory 2000 m deep wells, drilled by Geotermica del Norte S.A. between August 2009 and October 2010, allowed to detect the presence of water-dominate reservoir with temperature of about 260 °C.

On September 2015 was announced the construction, in the Apacheta geothermal field, of the first power plant powered by geothermal energy of South America. The ORC binary plant will comprise two 24 MW units which, when fully working, will be able

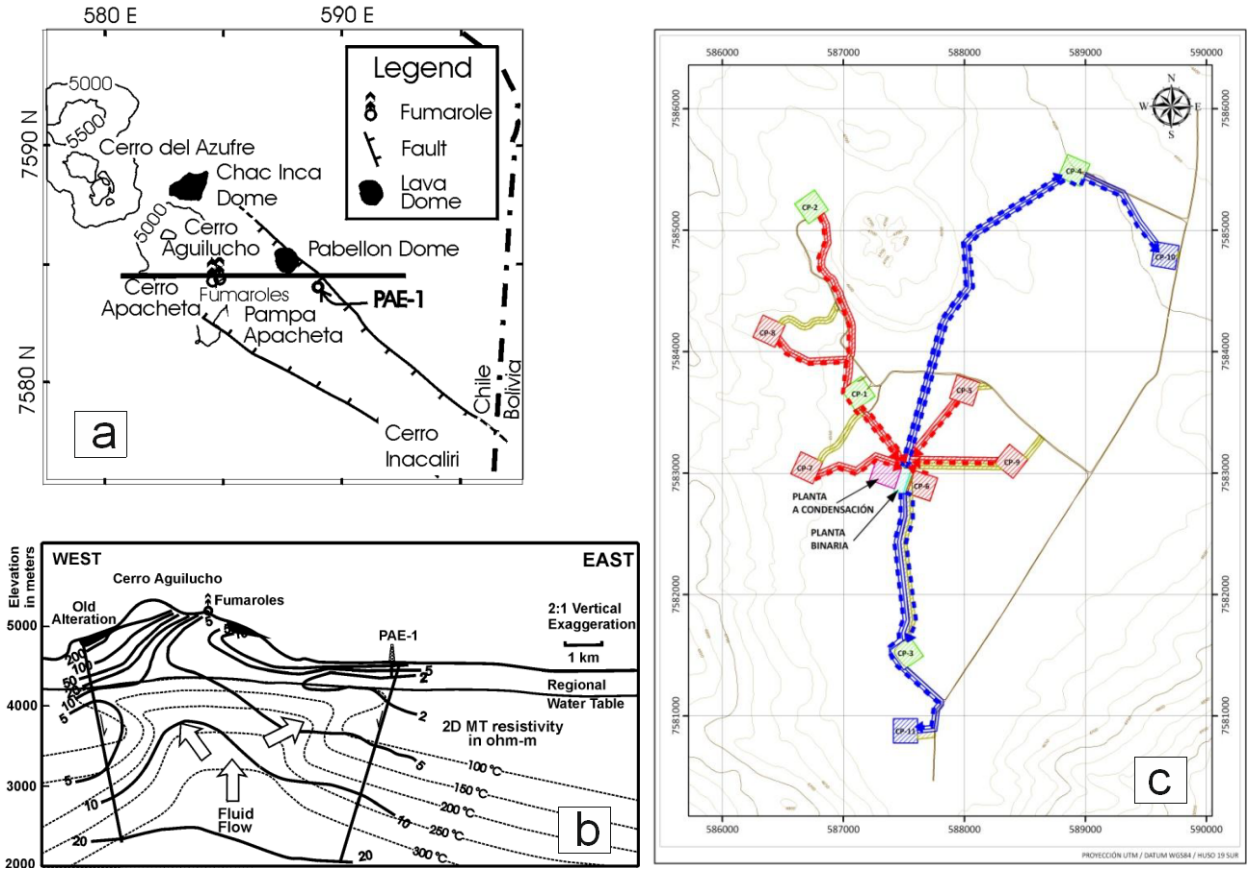

Fig. 3.6. a) Map of the Apacheta prospect. Thick black line indicates location of cross section depicted in b). b) Conceptual cross section of temperature and MT resistivity (Urzua et al., 2002). c) Production and re-injection platforms of power plant. Red squares and lines: production platforms and pipeline system of hot fluid toward the plant. Blue squares and line: re-injection platforms and pipeline system to re-injection wells. Green squares: platforms that have already been constructed in the context of the exploration stage (Enel Latinoamérica (Chile) Ltda.).

to produce nearly 340 GWh per year, equivalent to the needs of consumption of 165,000 Chilean homes, and avoiding the emissions of more than 166,000 tons of CO_2 per year (Rojas, 2015). The project contemplates the construction and operation of a maximum of 20 geothermal wells, being either production or reinjection, located in 11 individualized platforms (Fig. 3.6c). In each platform, a maximum of 4 wells can be perforated. The wells will be perforated until they reach the geothermal reservoir, with an estimated depth of 1,900 to 2,700 meters (Dixon and Nakagawa, 2016).

The commissioning of the first 24 MW unit is expected to be in early 2017, while that of the second unit in the first months of 2018.

3.3 GEOTHERMAL RESOURCES IN ECUADOR

Ecuador is located on the active convergent margin of South America, in the Andean Northern Volcanic Zone (Fig. 3.4). It is characterized by Quaternary volcanism resulting from the eastward subduction of the Nazca Plate beneath the South American Plate. In Ecuador there are more than 50 volcanoes, many of which are of Holocene age and still active (Hall et al., 2008). The intense and widespread volcanic activity ensures the presence of important exploitable crustal thermal anomalies.

Earlier geothermal exploration in Ecuador began in 1979 with the "Proyecto de

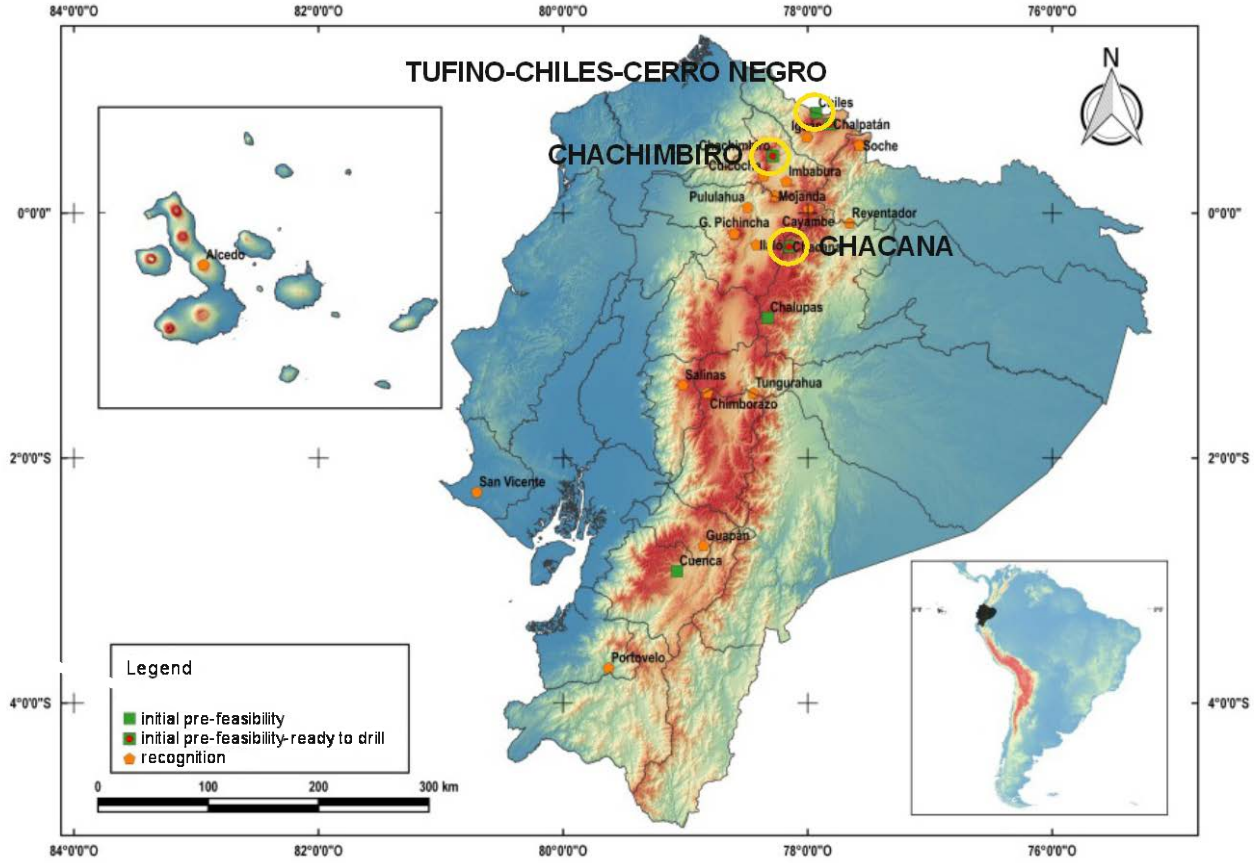

Fig. 3.7. Geothermal areas of Ecuador and location of main geothermal prospect for electric generation (modified from INER, 2015).

Investigación Geotérmica de la Repubblica de Ecuador" (INECEL, OLADE, BRGM, Aquater) with the aim to find high-temperature hydrothermal systems along areas of recent volcanism. The report summarized the areas of interest in two main groups: a high temperature group, Tufiño, Chachimbiro and Chalupas and a low-temperature group, Ilaló, Chimborazo and Cuenca. Between 1981 and 1992, INECEL with the collaboration of Colombian ICEl carried out prefeasibility studies on bi-national geothermal prospect of Tufiño-Chiles-Cerro Negro located at the border between Ecuador and Colombia. In the same period other investigation through geochemical and isotopic technique were carried out in various geothermal areas. Anyway the geothermal investigation program ended in 1993. In 2008, the Ecuadorian government through MEER, re-starts geothermal exploration, aiming to develop the former geothermal prospects for power generation. In 2010 MEER launched the Geothermal Plan for electricity generation, which described and priorized 11 geothermal prospects countrywide. These prospects were: Chachimbiro, Chalpatán, Chacana-Jamanco, Chalupas, Guapán, Chacana-Cachiyacu, Tufiño, Chimborazo, Chacana-Oyacachi, Baños de Cuenca and Alcedo.

According to INER (2015) (Fig. 3.7), there are four prospects classified as high enthalpy resources (Tufiño-Chiles-Cerro Negro, Chacana, Chachimbiro and Chalupas) in Ecuador, three medium-low enthalpies (Chalpatán, Baños de Cuenca and Ilaló) and other prospects with not enough information to be cataloged. Some of these not cataloged prospects already have certain preliminary survey studies (Chimborazo, Oyacachi, Salinas de Bolivar, Cuicocha, Tungurahua, San Vicente, Portovelo) while others are only identified by vulcanological signs and by the presence of hot springs (Cayambe, Pululahua, Guagua Pichincha, Imbabura, Mojanda, Iguán, Soche and Reventador). Among the most advanced projects pre-feasibility studies provided favorable results for high-temperature resources at Tufiño-Chiles-Cerro Negro, Chachimbiro and Chacana while in the case of Chalpatán have determined the existence of a resource of low temperature. Tufiño-Chiles-Cerro Negro, Chachimbiro and Chacana are therefore the only projects in Ecuador that currently have clear development prospects for electricity generation.

3.3.1 The Tufiño-Chiles-Cerro Negro geothermal field

This prospect is located in Ecuador, on the Western Cordillera, at 35 km west of the city of Tulcán, 7 km west of the villages of Tufiño and Chiles, in the province of Carchi (Ecuador) and Nariño department (Colombia). The development area lies across the Ecuador-Colombia border. Late Pleistocene andesitic to dacitic Chiles volcano and the adjacent to the west Cerro Negro de Mayasquer constitute the main heat source of the area. The tectonic framework is characterized by active NNE trending regional strike-slip faults (Cepeda et al., 1987) and local NNE and NW trending fault systems cutting the volcanic complex (ICEL, 1983).

As reported by Coviello (2000), in 1978 INECEL (Instituto Ecuatoriano de Electrificación) carried out the first

geothermal reconnaissance activities during which identified the presence of several relatively high temperature thermal sources and volcanic structures of recent age. In 1979, the OLADE (Organización Latinoamericana de Energía) with the technical support of Italian (Aquater) and French (Brgm) companies operating in the energy sector, carried out a preliminary geological and geochemical study on the most promising areas for the existence of geothermal resources. In 1982 the governments of Ecuador and Colombia signed an agreement to develop a joint geothermal exploration that marked the beginning of the "Binational Geothermal Project Tufiño-Chiles-Cerro Negro. During the 1980's were carried out pre-feasibility studies on behalf of OLADE, INECEL and ICEL (Instituto Colombiano de Energía Eléctrica) which detected the presence of a 2000 meters-deep reservoir with temperature higher than 200 °C and a shallower reservoir between 500 and 1000 meters with temperatures up to 150 °C.

As reported by Beate and Urquizo (2015), acid hot springs, up to 55°C occur 2 – 3 km to the east of Volcan Chiles, along E-W faulting and extensive areas of hydrothermally altered rocks are found few kilometers south of Volcán Chiles indicating likely that the shallow part of the system has sealed up. Gas geothermometers indicate reservoir temperatures as high as 230°C. Resistivity data suggest the existence of a geothermal reservoir with a fault controlled eastwards lateral outflow on the east flank (INECEL-OLADE-AQUATER, 1987). Elevation of top of reservoir is below 3,100 masl with 100°C waters, but exploitable temperatures are 200-300 m deeper, indicating a drilling target for production at 1,000 to 1,500 m depth; this is indicated by the presence of a thick conductive layer, which is shallow (about 100 m) below the acid springs, but deepens 400 to 500 m towards the east (outflow).

In 2009, a shallow (500 m), small gradient bore holes was drilled in Ecuadorian side of the prospect. It was the very first geothermal hole to be drilled in Ecuador and reached a total depth of 554 m. Lithology comprises of till, lavas and thick sequence of rather low permeability volcaniclastics (microbreccias) and associated sediments as sandstone and siltstone.

Recently, in 2013, new fundings allowed to carry out complementary studies, comprising geology (mainly $^{40}Ar/^{39}Ar$ dating of rocks and defining alteration mineralogy), geochemistry (focused on gas analyses and isotope determination, D/^{18}O, He, ^{13}C and ^{34}S) and geophysics based on about 100 MT/TDEM stations. This international contract was won by SYR in late 2013 and field work on geology and geochemistry started February 2014 on the Ecuadorian side.

3.3.2 The Chachimbiro geothermal field

The following discussion is based on Beate and Urquizo (2015).

This prospect is located in Ecuador, on the east slopes of the Western Cordillera about 70 km NNE from Quito and 17 km NE from Ibarra. Long-lived Quaternary andesitic-dacitic Chachimbiro volcanic complex represents the heat source for the system and several mixed chloride-bicarbonate hot and warm springs, with temperatures up to 61 °C, are located on the E and SE slopes of

volcanic structure. The subsurface rocks are formed by thin layer of late Tertiary volcanic products and by a folded and faulted late Cretaceous volcanic and sedimentary basement of accreted oceanic affinity. The tectonic setting is dominated by regional NE-SW trending dextral strike-slip faults with extensional component providing both the conduit for the magmatic intrusion as well as the pathways for the ascent of deep thermal fluids and ensuring a favourable environment for the development of a high permeability fracture network. Hydrothermal alteration occurs and smectite-chlorite haloes around advanced argillitic alteration might indicate that the temperature of the thermal manifestations was higher in the past. The geochemistry of prospect waters and gas is complex and does not lead to a single interpretation. Solute and gases geothermometry indicates temperatures up to 235°C and 206°C, respectively. Geophysical surveys (MT) resolves an extensive, low resistivity, smectite clay alteration zone consistent with the clay alteration that caps almost all developed geothermal reservoirs.

However, although generally encouraging, the relatively high values of resistivity in some parts of the clay seal appear to indicate potentially permeable gaps that complicate the conceptual model and increase the risk that a reservoir could not be present. Integration of the geology, fluid geochemistry and geophysics survey results yields three possible conceptual models for the resource: model 1, moderate to high temperature geothermal resource are associated with the Azufral fault zone and an optimistic interpretation of the resistivity anomaly provides an upside areal extent of 12 km^2. By applying a range of power densities from 10 to 20 MWe per km^2, probabilistic assessments of resource capacity provide a range of 13 to 178 MWe with a mean resource size of 81 MWe. Model 2, the high temperature system has peaked and is now in a cooling and waning phase. Model 3, the system is immature and the fluids have failed to achieve chemical equilibrium. This latter is the most pessimistic model and would imply that a commercial resource does not exist at Chachimbiro. A conceptual model of

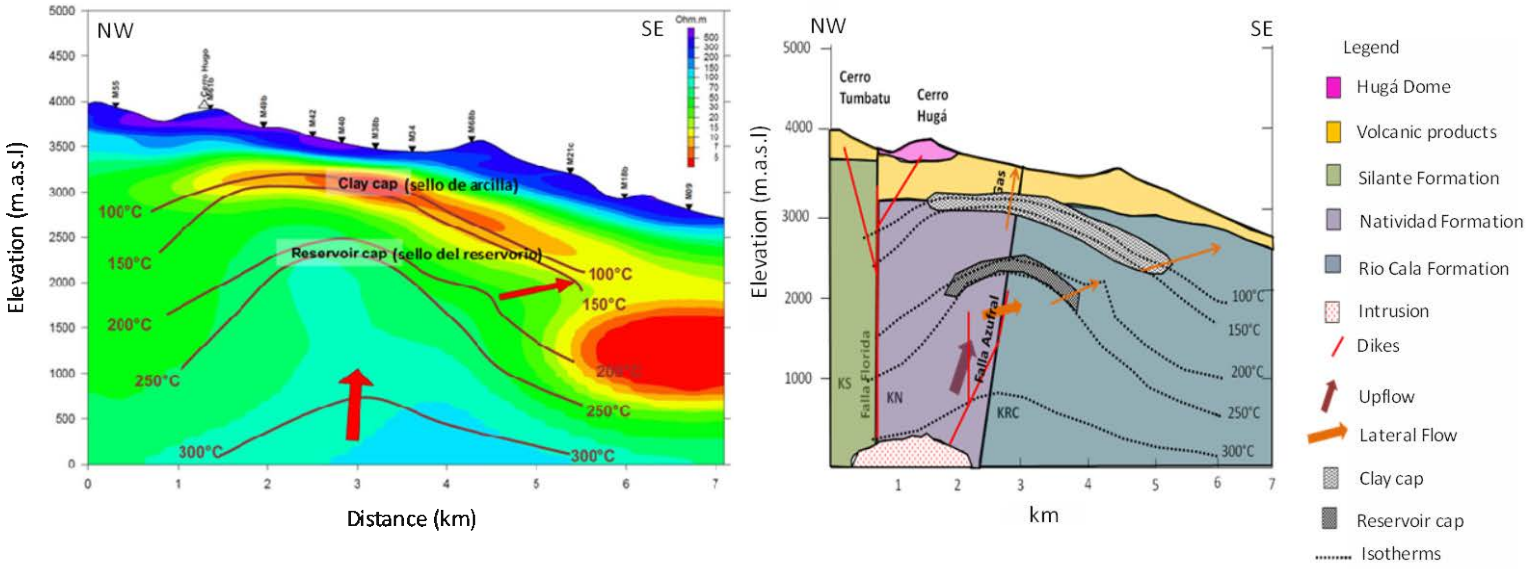

Fig. 3.8. NW-SE cross section of MT resistivity. Conceptual model of Chachimbiro geothermal system (SYR: Chachimbiro Pre-Feasibility Study presentation: *informe final*).

Chachimbiro prospect is shown in Figure 3.8 (SYR: Chachimbiro Pre-Feasibility Study presentation: informe final). Ecuadorian utility Corporacion Electrica del Ecuador (Celec) will start initial preparation work for exploration work at the Chachimbiro geothermal prospect. Celec is in discussion with “Japan International Cooperation Agency (JICA)” on technical cooperation for advanced stage of pre-feasibility studies, including the first deep geothermal drilling (Hristova, 2015).

4 The application of amphibole thermobarometry to constrain the heat source of geothermal systems in geothermal areas of Chachimbiro (Ecuador), Apacheta and La Torta (Chile)

4.1 INTRODUCTION

Knowledge of physico-chemical parameters of magmatic systems is crucial to describe the processes of cooling and differentiation and to formulate petrogenetic intepretations. Thermobarometric models based on chemical equilibria among coexisting mineral-mineral or mineral-melts pairs (Andersen and Lindsley, 1988; Beattie, 1993; Holland and Blundy, 1994; Putirka et al., 2003; Putirka, 2005) are useful tools widely used to estimate the P-T path and chemical evolution during igneous processes (Civetta et al., 1998; Scaillet and Evans, 1999; Lindsay et al., 2001; Bachmann and Dungan, 2002; Thornber et al., 2003; Blundy et al., 2006; Herzberg et al., 2007; Martins et al., 2008; Savov et al., 2008; Stroncik et al., 2009; Turner et al., 2013; Yücel et al., 2014; Ridolfi et al., 2015).

An important contribution to thermobarometry comes from calcic amphibole since it crystallizes in a wide range of physico-chemical and compositional conditions (Anderson, 1980; Niida and Green, 1999; Féménias et al., 2006; Evans, 2007; Ishimaru and Arai, 2008; Ridolfi et al., 2010a; Ridolfi and Renzulli, 2012) and was recently used by several authors to relaunch old (Anderson et al. 2008) and develop new thermobarometric applications (Ridolfi et al. 2010a; Krawczynski et al. 2012; Ridolfi and Renzulli 2012; Simakin et al. 2012; Molina et al. 2015). The high sensitivity of amphibole to physical-chemical changes makes it a good tracer of sub-volcanic processes such as magma storage, mixing and ascent. In literature there are many works concerning the use of amphibole compositional data to unravel magmatic processes and pre-eruptive conditions of subduction-related volcanic systems (Rutherford and Hill, 1993; Rutherford and Devine, 2003; Humphreys et al., 2006; Ridolfi et al., 2008; Rutherford and Devine 2008; Thornber et al., 2008; Ridolfi et al., 2010a; Ridolfi and Renzulli 2012; Costa et al., 2013; De Angelis et al., 2013; Shane and Smith, 2013; Erdmann et al., 2014; Kiss et al., 2014). The good reliability achieved with amphibole thermobarometry to constrain the sub-surface P-T conditions (Ridolfi et al., 2010a; Ridolfi and Renzulli, 2012), makes it possible to extend this application to high enthalpy geothermal energy studies for which the preliminary prospecting stage needs tools able to identify the depth and chemical-physical conditions of magma body which represents the heat source of the geothermal system. So far there are not examples from literature in this regard.

Anyway, the high sensitivity of amphibole composition to several and somehow mutual factors such as temperature (T), pressure (P), oxygen fugacity (fO_2), melt composition and volatile content (H_2O_{melt}), make the

application of amphibole-related thermobarometers difficult any time a system depart from chemical equilibrium. Indeed rapid or significant variations in these parameters can lead to amphibole disequilibrium texture such as reverse and oscillatory zoning, fast crystal growth and quenching (Rutherford and Hill, 1993; Scaillet and Evans, 1999; Kuşcu and Floyd, 2001; Sato et al., 2005; Browne and Gardner, 2006; Ridolfi et al., 2008; Humphreys et al., 2009; De Angelis et al., 2013; Shea and Hammer, 2013). These disequilibrium states, if not properly considered, can result in misleading, anomalous and even erroneous thermobarometric applications such as the use of granitoid amphibole barometers to high temperature crystallizing conditions (e.g. Kiss et al. 2014).

This work tests the capability of amphibole thermobarometry to characterize the heat sources of the Chachimbiro Geothermal Area (CGA), located in the northern sector of Ecuador, Apacheta Geothermal Area (AGA) and La Torta Geothermal Area (TGA), located in the northern sectors of Chile. We used the application of Ridolfi and Renzulli (2012) (hereafter R&R2012) allowing to estimate the intrinsic physico-chemical parameters with reasonably low uncertainties (T±24 °C, P±12%, fO_2±0.4 log units) and the composition of the melt in equilibrium with Mg-rich calcic amphibole in a wide range of conditions, up to 1,130°C and 2.2 GPa. We have chosen this thermobarometric/chemometric model because as far as we know it is the only amphibole application calibrated with accurately selected experimental amphiboles approaching, as much as possible, total equilibrium conditions in both textural and chemical terms. Since this thermobarometric model was obtained at “perfect” equilibrium conditions, a fundamental aspect is to avoid its application to amphiboles showing clear evidence of crystallization at disequilibrium conditions. In this work we suggest a method to avoid as much as possible the application of amphibole thermobarometry to compositions resulting from disequilibrium crystallization. Furthermore we test the reliability of the barometric model to high pressures comparing our results to a model of seismic tomography for the AGA system (Ward et al., 2014).

4.2 VOLCANOLOGICAL, GEOPHYSICAL, GEOCHEMICAL AND GEOTHERMAL BACKGROUND

4.2.1 The Apacheta and La Torta geothermal areas (Chile)

The Apacheta geothermal area (AGA; about 100 km NE of the city of Calama) and La Torta geothermal area (TGA; about 100 km E of the city of Calama) are located in the northernmost sectors of the Altiplano Puna Volcanic Complex (APVC) close to the Chile-Bolivia border, above an exceptionally thick continental crust (>70 km, Schmitz et al., 1999) in a large area of silicic volcanism occupying the 21-24°S segment of the Andean Central Volcanic Zone (ACVZ; de Silva, 1989; de Silva et al., 1994; Stern, 2004) (Fig. 4.1 a, b, c). The ignimbrite flare up that produced the APVC is characterized by

episodic volcanism over the last 11 Ma time-span that climaxed at about 4 Ma (de Silva, 1989). Since peak activity, the temporal and spatial record of volcanism suggests a waning of the ignimbrite activity over the past 2 million years (Salisbury et al., 2011) with only one other super-volcanic eruption at 2.6 Ma (Casey, 2011). The crystal-rich ignimbrites are distribuited over an area of about 70,000 km^2 and are characterized by predominantly calc-alkaline dacite with rare rhyolite and andesites (de Silva et al., 2006). The occurrence of dacite to rhyolite lavas and domes (*tortas*) erupted in the past 100 ka and the existence of a partially melted zone in the upper crust of the APVC, i.e. Altiplano-Puna Magma Body (APMB; Chmielowsky and Zandt, 1999; Zandt et al., 2003; Ward et al., 2014), indicate that the magmatic system of the APVC is currently active (de Silva, 1989).

The AGA extends within a NW-SE oriented graben (Inacaliri Graben) between the Quatenary Azufre volcano toward NW and the Pliocene Lailay volcano to the south. The geothermal system is associated with the basaltic andesite to rhyolite Plio-Pleistocene Apacheta-Aguilucho Volcanic Complex (AAVC) (Mercado et al., 2009) including the associated Apacheta (also known as Pabellòncito) and Chac-Inca domes (Fig. 4.1 c) dated at 50 ± 10 (K/Ar method; Urzua et al., 2002), 80-130 Ka (Ar-Ar method; Renzulli et al., 2006) and 140±80 Ka (Ar/Ar method (report ENG, Empresa Nacional de Geotermia

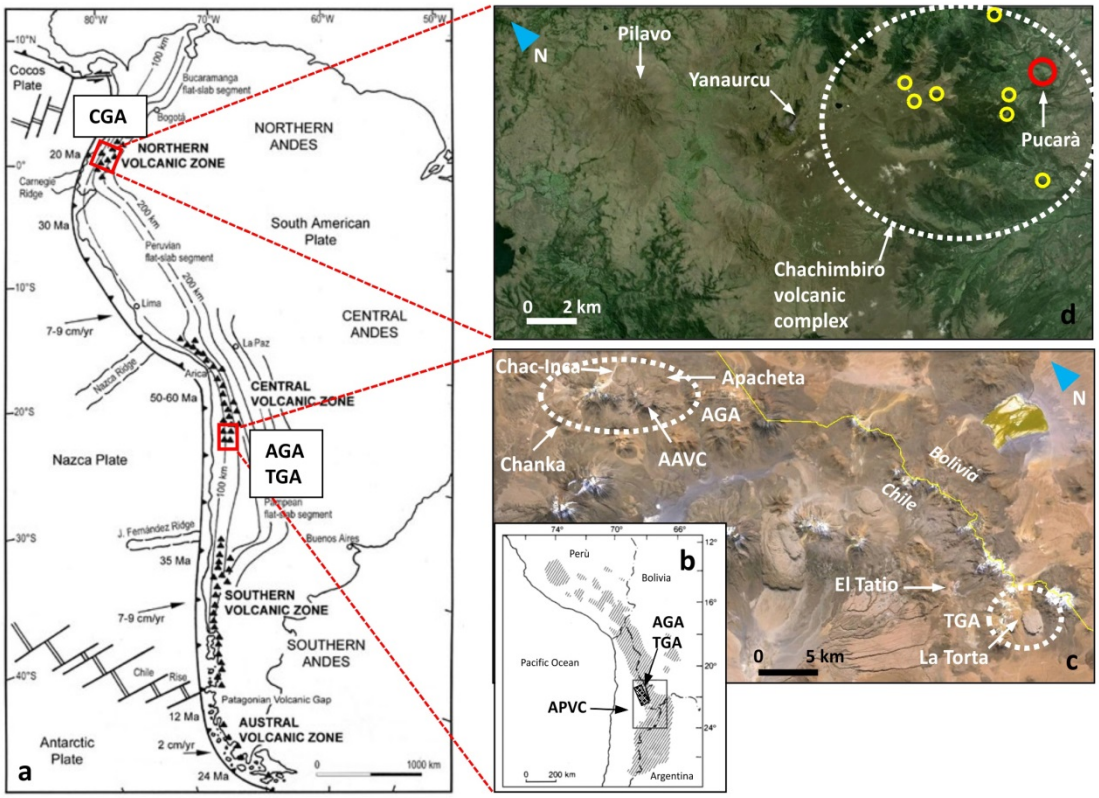

Fig. 4.1. a) Image showing the subduction zone of South America with the subdivision in Andean Northern, Central, Southern and Austral Volcanic Zone (modified by Cordani et al. 2000); the red rectangles indicate the location of CGA, AGA, TGA geothermal areas. b) image showing location of APVC, AGA and TGA (modified by Piscaglia 2011) and c) enlarged view of AGA and TGA with the position of studied volcanic structures. Location of El Tatio geothermal area is also reported. d) enlarged view of CGA with the border of Chacimbiro Volcanic Complex inside which are shown the location of Pucarà dome (red circles) and the other main volcanic structures (yellow circles); toward NNW are located other two important volcanoes of the area, Pilavo and Yanaurcu.

S.A., Chilean National Geothermy Company), respectively. The 1.5 Ma-years-old Chanka dome (Roobol et al., 1974) (Fig. 4.1 c) lies about 13 km toward NW, on the prolongation of the southern fault of Inacaliri Graben. According to Piscaglia (2011) AGA products are classified as high-K calc-alkaline andesites, dacites and rhyolites [57.7-69.9 wt% SiO_2; 5.5-7.9 wt% (Na_2O+K_2O); 2-4.5 K_2O, normalized to an anhydrous basis] (Fig. 4.2).

A temperature >200°C was found at depths >500 m in a 550 m-deep core-hole recently carried out on October 2007 [ENEL (Ente Nazionale per l'Energia Elettrica, Italian National Electric Energy Company), *personal communication*)] whereas MT (Magnetotelluric) and TDEM (Time Domain Electromagnetic) geophysical survey detected a low resistivity boundary (< 10 Ω·m) extending over an area of 25 km^2 (Urzua et al., 2002). The ENG has recently obtained the approval of the environmental impact assessment for the installation of a 50 MWe geothermal power plant in the AGA. Prominent hydrothermal alteration is present in the north, west, southwest and eastern flanks of Apacheta and Aguilucho volcanoes related to past and present fumarolic activity. The structural weakening of the Apacheta and Aguilucho volcanoes by hydrothermal alteration is confirmed by the presence of a debris avalanche deposit morphologically emphasized by small hummocks in the eastern flank of the volcanoes and mainly consisting of hydrothermally altered lava fragments (Mercado et al., 2009; Aguilera et al., 2008). The study of the drilled cap-rock samples confirm the presence of hydrothermally altered volcanic rocks belonging to the zeolite (shallower depths) and argillitic facies (Piscaglia, 2011). Thermal fluid discharges of the Apacheta fumarolic system have outlet temperatures varying between 83.2 and 84.3 °C. The chemical composition of dry gases is dominated by the presence of CO_2 and N_2 (Tassi et al., 2010). Geochemical surveys and related gas thermometers (CO_2/Ar and H_2/Ar) of the AGA indicate reservoir temperatures of ca 250°C (Urzua et al., 2002). Additional reservoir temperatures, estimated with the H_2/Ar (Chiodini et al., 2001) and organic gas geothermometers (Capaccioni and Mangani, 2001; Tassi et al., 2005) are particularly high (>330°C), possibly in relation to the presence of a deep magmatic system still active in the area, as also indicated by the relatively high contents of light alkenes, HCl and SO_2 (Tassi et al., 2010).

La Torta geothermal area is dominated by the tabular Pleistocene La Torta dome dated 34±7 Ka (Ar/Ar method, Renzulli et al., 2006) (Fig. 4.1 c) with a high-K calc-alkaline rhyolite composition [71.7 wt% SiO_2; 7.5 (Na_2O+K_2O); 4.1 K_2O, according to Piscaglia (2011)] (Fig. 4.2). Hot springs and gas seeps near 4800 m elevation at La Torta discovered by ENAP (Empresa Nacional del Petróleo, Chilean National Oil Company) in 1998, the presence of Sol de Mañana geothermal field 20 km to the southeast in Bolivia and the El Tatio geothermal field 10 km to the northeast (Fig. 4.1 c) suggests a large scale alignment of hydrothermal manifestations along regional extensional structural environment (Cumming et al., 2002). La Torta geothermal field is located at the southern extension of the eastern edge of El Tatio graben and the

geology of La Torta area is assumed to be similar to that of El Tatio, dominated by thick Tertiary ignimbrite flows (Lahsen and Trujillo, 1976b; Hauser, 1997). According to Cumming et al., (2002), MT-TDEM survey identified a low resistivity hydrothermal smectite clay zone extending more than 15 km southeast of El Tatio, continuing beneath the La Torta dome and covering more than 50 km^2. Some wells drilled at El Tatio show temperature reversals indicating that they had encountered a tabular outflow flowing to the west and north from an area to the east or south of the wells (i.e La Torta area). Consistently, N_2/Ar and He isotopes and geothermometry of 250 to 280°C suggest that the gas seep at La Torta originates from the same hydrothermal system as the gases from the El Tatio fumaroles. A progressive southeast (La Torta) to northwest (El Tatio) depletion of less water-soluble gases relative to CO_2 is consistent with an upflow near the La Torta gas seep. Geophysical and geochemistry evidence suggest that El Tatio and La Torta share the same deep reservoir with a magma body centered near the Cerros del Tatio and La Torta dome.

4.2.2 The Chachimbiro Geothermal Area (Ecuador)

The CGA is located in the Andean Northern Volcanic Zone in the northern part of the Ecuadorian Volcanic Front (EVF) (ANVZ, Stern, 2004) (Fig. 4.1 a), about 70 km NNE from Quito and 17 km NW from Ibarra. The Holocene volcanic activity of the EVF is characterized by powerful but low-frequency explosive eruptions of andesite to dacite, and by lava dome extrusions (Von Hillebrandt 1989; Hall and Mothes 2008; Hidalgo et al., 2008; Robin et al., 2008). The CGA is underlain by mid-Tertiary volcanoclastic sediments and strongly tectonized Cretaceous oceanic basalts and associated sediments (Pallatanga Terrain). The inferred thickness of the crust is about 50-60 km (Feininger and Seguin, 1983; Guillier et al., 2001).

The heat source of the CGA is represented by the Quaternary Chachimbiro Volcanic Complex (CVC), which includes the collapsed Middle Pleistocene andesite Huanguillaro volcano, a series of caldera-filling rhyodacite domes and the Late Pleistocene-Holocene Chachimbiro – Pucará NNE line of dacite (Beate and Salgado, 2010) and andesite domes (Fig. 4.1 d). The most recent volcanic products of CVC are pyroclastic deposits related to volcanic activity of Pucarà dome. This dome suffered south-east sector collapse ascribed to a major lateral blast, followed by a period of quiescence and a second phase of dome building. Finally a new eruptive phase marked the end of volcanic activity of Pucarà and the entire volcanic complex. Radiocarbon dating of soils underlying the pyroclastic deposits, constrain the first eruption (called *Lower Event*) between 7,250-4,420 years BP while the second eruption (called *Upper Event*) is younger than 4150 years BP (Comida, 2012). CVC domes are classified as andesites and dacites of calc-alkaline and subordinately, tholeiitic series [58.6-69 wt% SiO_2; 4-6.5 wt% (Na_2O+K_2O); 0.5-2 wt% K_2O, according to Comida (2012)] (Fig. 4.2). Bernard et al. (2014) pointed out as the source of the most

recent eruption of CVC, dated between 4,720-4,855 years BP, was a moderate-sized dome, destroyed by the eruption, emplaced in a valley at the foot of Cerro La Viuda about 3 km N of Pucarà dome. Juvenile samples collected by Bernard et al. (2014) are calc-alkaline rhyodacites [67.3-68.5 wt% SiO_2] (Fig. 4.2).

Older Yanaurcu volcano (andesite to rhyodacite) as well as late Pleistocene Pilavo volcano (mainly basaltic andesites), are located to the W of Huanguillaro volcano (Chiaradia et al., 2011; Gorini, 2011) (Fig. 4.1 d).

The geothermal reservoir could be composed by fractured volcanic rocks related to dome activity and older proximal lava flow facies related to early volcanic activity covering the crustal basement, as well as locally fractured facies of the Pallatanga Terrain. On the basis of surface exploration data Almeida (1990) estimated for the CGA a potential of ca. 113 Mwe. Sodium-chloride to Na-Cl-HCO_3 type hot springs are present, with temperatures ranging from 40 to 55 °C (Beate and Salgado, 2010) probably originated through dilution of the parent geothermal fluids with different degrees of re-equilibration with country rocks at lower temperatures (Aguilera el al., 2005). Possible deep-temperatures of the geothermal reservoir are 225-235°C, although temperatures at the base of the geothermal system are inferred to be higher than 260°C (Aguilera et al., 2005). Deep equilibrium temperatures of the reservoir around 260°C were also estimated by Gherardy and Spycher (2014) through the application of the integrated multicomponent geothermometry (Spycher et al., 2011, 2014) based on the mineral saturation index method (Reed and Spycher, 1984), coupled with numerical optimization

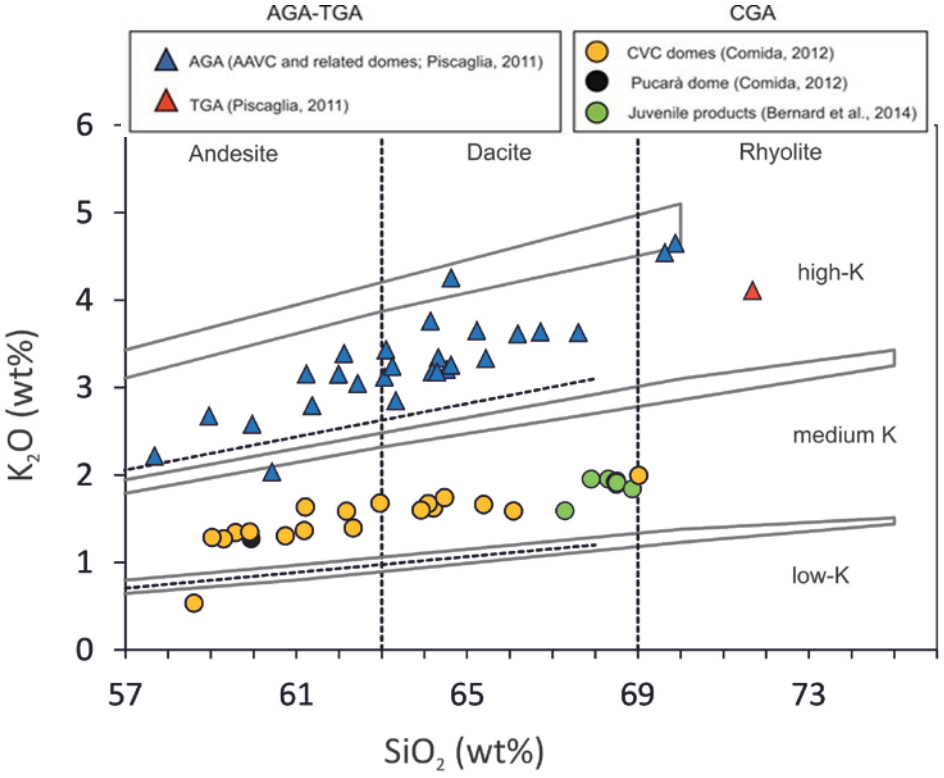

Fig. 4.2. K_2O vs SiO_2 diagram (Rollinson, 1993). All compositions recalculated to 100% on a LOI-free basis. Data for Apacheta Geothermal Area (AGA), La Torta Geothermal Area (TGA), Chachimbiro Volcanic Complex (CVC) and Pucarà domes are unpublished.

to reconstruct the deep fluid chemistry. As reported by Beate and Salgado (2010) fault controlled areas of hydrothermally altered rocks with no anomalous temperature, crop out in the central part of the CGA, probably indicating a self-sealing of the upper part of the system. Resistivity soundings on the E part of the CGA reveal a lateral outflow to the E, whereas there are no deep-reaching resistivity surveys in the centre of the area.

4.3 SAMPLES AND ANALYTICAL METHODS

Representative volcanic products from AGA, TGA and CGA for petrographic observation and electron microprobe analyses were selected. For AGA was taken into account samples of andesite (AA010) and rhyolite (AA064) lava flows along the Apacheta-Aguilucho volcanic edifice and associated lava domes of Apacheta (CPBa) and Chac-Inca (CINKA). Sampling has been extended to the Chanka dome (CKA1, CKA1a, CKA1b). For TGA we considered the lava dome of La Torta (TA12, CT1a).

Sample collection from CGA was focused on the most recent volcanic products of CVC, i.e. Pucarà lava dome (CH17) and juvenile ejecta from related pyroclastic deposits of lower event (CH22, CH23, CH24) and upper event (CH27) (Comida, 2012) (see section 3.2.2).

Polarized light optical microscopy was used for textural and modal analyses. Qualitative compositional analyses were performed at the University of Urbino (Italy) with an Environmental Scanning Electron Microscope (ESEM, Quanta 200 FEI) equipped with a field emission gun and an energy dispersive system (EDS). The ESEM analyses were performed on carbon-coated thin sections at vacuum conditions (0.83 mbar) with an accelerating voltage of 30 kV and a beam current of 264 mA.

Electron microprobe analyses of the minerals (Table 4.1a, b) were performed at the "Istituto di Geoscienze e Georisorse" - National Research Council (IGG-CNR), Padua research centre (Italy), using a Cameca SX-50 microprobe equipped with four vertical wavelenght-dispersive spectrometers. Analyses were carried out in spot mode (beam size ~ 1 µm, 15 keV, 15 nA) and using natural silicate standards for major elements calibration. Analyses were focused on amphibole crystals (Table) and comprise amphiboles from abundant intermediate-basic microcrystalline enclaves hosted in Apacheta, Chac-Inca and Chanka domes. We selected 152 amphibole crystals for a total of 462 data (among single point analyses and core-rim transects, 50).

4.4 RESULTS

Petrography and mineral chemistry of representative thin sections are briefly described below except the amphibole, which is discussed in detail in section 3.4.2.

4.4.1 Mineral chemistry and petrography

Among the andesite lava of AAVC, the AA010 sample (62.1 wt% SiO_2, Piscaglia, 2011) (Fig. 4.3 a) contains both clino- and orthopyroxene

Table 4.1a. Chemical compositions of representative minerals of AGA and TGA.

Site	AAVC												Apacheta				Chac-Inca		
Sample	AA010						AA064						CPBa				CINKA1		
Host	andesite						rhyolite						dacite			andesite	dacite		
Type	lava flow						lava flow						lava dome			enclave	lava dome		
Mineral	pl	pl	cpx	opx	Fe-Ti ox.	bt	pl	pl	cpx	opx	Fe-Ti ox.	bt	pl	Fe-Ti ox.	bt	pl	pl	Fe-Ti ox.	bt
Texture	phen	phen	phen	phen	microphen	phen	phen	phen	phen	phen	microphen	phen	phen	microphen	phen	phen	phen	microphen	phen
SiO_2	59.73	50.61	52.99	53.58	0.09	39.43	62.56	51.12	53.20	56.61	0.03	37.21	58.45	0.11	38.04	53.37	58.26	0.09	37.61
TiO_2	0.00	0.08	0.34	0.24	8.54	5.31	0.02	0.02	0.31	0.21	2.06	3.72	0.00	4.72	4.23	0.06	0.00	4.03	4.22
Al_2O_3	25.01	30.90	1.20	1.51	2.70	13.27	23.90	30.78	2.48	1.40	0.93	12.92	26.47	1.52	13.97	29.76	25.76	1.59	13.68
Cr2O3	0.00	0.00	0.00	0.07	0.08	0.00	0.00	0.03	0.56	0.28	0.06	0.08	0.00	0.07	0.06	0.00	0.05	0.05	0.00
FeO_T	0.32	0.59	8.61	18.93	79.91	11.20	0.27	0.62	6.16	11.35	87.66	17.98	0.13	82.81	14.87	0.49	0.20	86.52	14.93
MnO	0.00	0.00	0.33	0.78	0.44	0.04	0.00	0.03	0.06	0.25	0.35	0.24	0.00	0.40	0.16	0.02	0.00	0.61	0.17
MgO	0.09	0.00	14.48	23.65	2.17	16.70	0.00	0.02	16.42	28.36	0.36	14.01	0.03	0.96	15.44	0.03	0.02	0.94	14.58
CaO	7.43	14.63	21.56	1.12	0.05	0.01	6.00	14.10	21.01	1.37	0.10	0.01	8.52	1.48	0.00	12.69	8.26	0.03	0.00
Na_2O	6.54	2.79	0.34	0.05	-	0.87	7.82	3.54	0.39	0.01	-	0.622	6.40	-	0.76	4.18	6.34	-	0.66
K_2O	0.99	0.39	0.00	0.00	-	8.44	1.09	0.15	0.00	0.03	-	8.74	0.50	-	8.71	0.19	0.50	-	8.85
Total	100.12	99.99	99.86	99.92	93.99	95.28	101.67	100.41	100.60	99.86	91.55	95.53	100.50	92.07	96.25	100.79	99.39	93.85	94.69
Ab%	58	25	-	-	-	-	66	31	-	-	-	-	56	-	-	37	56	-	-
An%	36	73	-	-	-	-	28	68	-	-	-	-	41	-	-	62	41	-	-
Or%	6	2	-	-	-	-	6	1	-	-	-	-	3	-	-	1	3	-	-
Wo%	-	-	45	2	-	-	-	-	43	3	-	-	-	-	-	-	-	-	-
En%	-	-	42	67	-	-	-	-	47	79	-	-	-	-	-	-	-	-	-
Fs%	-	-	14	30	-	-	-	-	10	18	-	-	-	-	-	-	-	-	-
Mg#	-	-	75	69	-	-	-	-	83	82	-	-	-	-	-	-	-	-	-
Mgn	-	-	-	-	79	-	-	-	-	-	95	-	-	89	-	-	-	90	-
Usp	-	-	-	-	14	-	-	-	-	-	3	-	-	7	-	-	-	6	-
Spn	-	-	-	-	7	-	-	-	-	-	2	-	-	4	-	-	-	4	-
Chr	-	-	-	-	0	-	-	-	-	-	0	-	-	0	-	-	-	0	-
Si	-	-	-	-	-	2.875	-	-	-	-	-	2.817	-	-	2.807	-	-	-	2.826
$^{[4]}Al$	-	-	-	-	-	1.125	-	-	-	-	-	1.153	-	-	1.193	-	-	-	1.174
$^{[6]}Al$	-	-	-	-	-	0.016	-	-	-	-	-	0.000	-	-	0.021	-	-	-	0.038
Ti	-	-	-	-	-	0.291	-	-	-	-	-	0.212	-	-	0.235	-	-	-	0.239
Cr	-	-	-	-	-	0.000	-	-	-	-	-	0.005	-	-	0.004	-	-	-	0.000
Fe	-	-	-	-	-	0.683	-	-	-	-	-	1.139	-	-	0.918	-	-	-	0.938
Mn	-	-	-	-	-	0.003	-	-	-	-	-	0.016	-	-	0.010	-	-	-	0.011
Mg	-	-	-	-	-	1.816	-	-	-	-	-	1.582	-	-	1.699	-	-	-	1.633
Ca	-	-	-	-	-	0.001	-	-	-	-	-	0.001	-	-	0.000	-	-	-	0.000
Na	-	-	-	-	-	0.123	-	-	-	-	-	0.091	-	-	0.109	-	-	-	0.097
K	-	-	-	-	-	0.785	-	-	-	-	-	0.844	-	-	0.820	-	-	-	0.848
Mg#	-	-	-	-	-	73	-	-	-	-	-	58	-	-	65	-	-	-	64

Table 4.1a: continued

Site	Chanka												La Torta					
Sample	CKA1				CKA1a						TA12	CT1a						
Host	dacite				andesite							rhyolite						
Type	lava dome				enclave						lava dome	lava dome						
Mineral	pl	opx	Fe-Ti ox.	bt	pl	opx	Fe-Ti ox.	bt			pl	pl	Fe-Ti ox.	bt				
Texture	phen	phen	phen	phen	phen	microphen	microphen	phen			phen	phen	phen	phen				
SiO_2	60.52	56.06	0.02	37.49	58.63	56.19	0.08	37.36			60.6	52.64	0.13	37.76				
TiO_2	0.00	0.18	4.20	4.30	0.05	0.15	6.79	4.13			0.02	0.00	3.39	4.79				
Al_2O_3	25.60	1.80	1.49	13.88	26.60	1.07	1.84	13.80			25.32	30.55	1.24	13.56				
Cr2O3	0.00	0.35	2.90	0.00	0.06	0.01	0.16	0.01			0.06	0.00	0.10	0.00				
FeO	0.20	10.91	81.98	15.01	0.24	13.79	83.62	18.73			0.26	0.28	85.69	15.97				
MnO	0.00	0.17	0.60	0.24	0.04	0.25	0.57	0.25			0	0.00	0.74	0.27				
MgO	0.00	29.99	1.06	14.85	0.03	27.86	1.16	11.90			0.01	0.00	0.75	13.62				
CaO	7.34	1.41	0.05	0.04	8.75	1.60	0.00	0.00			7.65	13.56	0.00	0.00				
Na_2O	7.09	0.00	-	0.72	6.45	0.01	-	0.3508			6.61	3.67	-	0.48				
K_2O	0.66	0.00	-	8.71	0.50	0.02	-	8.85			0.73	0.20	-	9.03				
Total	101.42	100.87	92.29	95.23	101.34	100.95	94.23	95.39			101.26	100.89	92.05	95.48				
Ab%	61	-	-	-	56	-	-	-			58	32	-	-				
An%	35	-	-	-	42	-	-	-			37	66	-	-				
Or%	4	-	-	-	3	-	-	-			4	1	-	-				
Wo%	-	3	-	-	-	3	-	-			-	-	-	-				
En%	-	81	-	-	-	76	-	-			-	-	-	-				
Fs%	-	16	-	-	-	21	-	-			-	-	-	-				
Mg#	-	83	-	-	-	78	-	-			-	-	-	-				
Mgn	-	-	85	-	-	-	85	-			-	-	92	-				
Usp	-	-	6	-	-	-	11	-			-	-	5	-				
Spn	-	-	4	-	-	-	5	-			-	-	3	-				
Chr	-	-	5	-	-	-	0	-			-	-	0	-				
Si	-	-	-	2.802	-	-	-	2.836			-	-	-	2.829				
[4]Al	-	-	-	1.198	-	-	-	1.164			-	-	-	1.171				
[6]Al	-	-	-	0.025	-	-	-	0.070			-	-	-	0.026				
Ti	-	-	-	0.242	-	-	-	0.236			-	-	-	0.270				
Cr	-	-	-	0.000	-	-	-	0.000			-	-	-	0.000				
Fe	-	-	-	0.938	-	-	-	1.189			-	-	-	1.001				
Mn	-	-	-	0.015	-	-	-	0.016			-	-	-	0.017				
Mg	-	-	-	1.655	-	-	-	1.346			-	-	-	1.522				
Ca	-	-	-	0.003	-	-	-	0.000			-	-	-	0.000				
Na	-	-	-	0.105	-	-	-	0.052			-	-	-	0.070				
K	-	-	-	0.831	-	-	-	0.857			-	-	-	0.863				
Mg#	-	-	-	64	-	-	-	53			-	-	-	60				

Table 4.1b. Chemical compositions of representative minerals of CGA.

Site	Pucarà dome						LPD*				UPD**			
Sample	CH17						CH23J	CH24J2	CH23J	CH24J2	CH27J1			
Host	andesite						andesite				andesite			
Type	lava dome						juvenile				juvenile			
Mineral	pl	pl	cpx	opx	Fe-Ti ox.	Fe-Ti ox.	pl	pl	Fe-Ti ox.	Fe-Ti ox.	pl	pl	Fe-Ti ox.	Fe-Ti ox.
Texture	microphen	phen	microphen	microphen	microphen	phen	phen	phen	microphen	microphen	phen	phen	microphen	phen
SiO_2	51.53	48.02	51.27	53.23	0.15	0.12	60.73	53.86	0.06	0.05	61.45	56.43	0.06	0.09
TiO_2	0.03	0.01	0.49	0.23	14.13	6.83	0.02	0.01	27.02	2.79	0.00	0.02	26.18	3.30
Al_2O_3	29.16	32.53	2.36	1.82	1.04	2.04	24.37	29.15	0.33	1.33	23.96	27.57	0.39	1.91
Cr2O3	0.00	0.00	0.00	0.00	0.00	0.04	0.00	0.00	0.01	0.00	0.00	0.00	0.02	0.00
FeO_T	0.80	0.50	10.04	16.93	73.14	82.41	0.08	0.3	65.67	88.41	0.23	0.23	65.97	86.54
MnO	0.02	0.02	0.54	0.75	0.61	0.52	0.00	0.01	0.15	0.38	0.01	0.03	0.22	0.68
MgO	0.15	0.05	16.46	26.08	1.52	2.11	0.03	0.01	0.73	0.90	0.00	0.00	0.89	1.02
CaO	12.14	15.66	18.44	1.38	0.45	0.00	6.00	11.32	0.03	0.07	5.40	9.49	0.05	0.02
Na_2O	4.27	2.39	0.25	0.02	-	-	7.66	4.85	-	-	8.19	5.96	-	-
K_2O	0.22	0.04	0.00	0.02	-	-	0.40	0.12	-	-	0.35	0.18	-	-
Total	98.32	99.21	99.86	100.45	91.04	94.06	99.29	99.63	94.01	93.98	99.58	99.91	93.80	93.56
Ab%	38	22	-	-	-	-	68	43	-	-	72	53	-	-
An%	60	78	-	-	-	-	30	56	-	-	26	46	-	-
Or%	1	0	-	-	-	-	2	1	-	-	2	1	-	-
Wo%	-	-	38	3	-	-	-	-	-	-	-	-	-	-
En%	-	-	47	71	-	-	-	-	-	-	-	-	-	-
Fs%	-	-	16	26	-	-	-	-	-	-	-	-	-	-
Mg#	-	-	76	73	-	-	-	-	-	-	-	-	-	-
Mgn	-	-	-	-	52	71	-	-	19	87	-	-	21	85
Usp	-	-	-	-	39	18	-	-	77	8	-	-	74	9
Spn	-	-	-	-	8	11	-	-	4	5	-	-	5	6
Chr	-	-	-	-	0	0	-	-	0	0	-	-	0	0

*LPD=lower pyroclastic deposit

**UPD=upper pyroclastic deposit

and has a partially vesiculated and seriated porphyritic texture (porphyritic index, P.I.=20 vol.%). The phenocrysts are, in order of abundance, plagioclase, orthopyroxene, clinopyroxene, amphibole, biotite and Fe-Ti oxides. The groundmass is micro-cryptocrystalline with the same mineralogical paragenesis of phenocrysts. Plagioclase phenocrysts compositions range from An_{36} to An_{73}. Bigger sized crystals show resorption and sieve textures with intense direct, inverse and oscillatory zoning, while smaller crystals are generally lacking of such textures and zoning. Clinopyroxenes have augitic compositions (Wo_{43-45} En_{40-41} Fs_{13-15}) and represent the most abundant mafic phase, while orthopyroxenes have generally enstatitic compositions (Wo_{2-4} En_{65-72} Fs_{25-32}). Fe-Ti oxides are magnetite with nearly constant composition (Mgn_{79} Usp_{14} Spn_{6-7}) with chromite content less than 0.14% (Table 4.1a).

AA064 rhyolite lava (Fig. 4.3 b) represents the most evolved magma erupted in the AAVC (69.6 wt% SiO_2, Piscaglia, 2011). It has a porphyritic texture (P.I.=20 vol.%) with convoluted banded textures and light-coloured zones surrounding highly vesiculated darker zones containing more basic material, probably due to mingling processes. The phenocrysts are, in order of abundance, plagioclase, sanidine, amphibole, quartz, biotite, orthopyroxene, clinopyroxene, Fe-Ti oxides and titanite (accessory phase). The groundmass is micro-cryptocrystalline with interstitial devitrified glass and locally pilotaxitic texture. Plagioclase phenocrysts compositions range from An_{28} to An_{68} with direct, inverse and oscillatory zoning. Quartz crystals have rounded edges and sometimes are embayed. Clinopyroxenes have augitic compositions (Wo_{32-46} En_{38-53} Fs_{10-15}) and represent the most abundant mafic phase. Orthopyroxenes have generally enstatitic compositions (Wo_3 En_{79} Fs_{18}). Fe-Ti oxides are magnetite (Mgn_{87-95} Usp_{3-11} Spn_{2-3}) with chromite content less than 0.12% (Table 4.1a). Hydrated minerals are always affected by breakdown textures or secondary alteration processes.

Chac-Inca and Apacheta domes are classified as dacites (66.7-67.6 wt% SiO_2, Piscaglia, 2011). The CPBa (Fig. 4.3 c) and CINKA sections have porphyritic and partially seriated texture (P.I.=30-35 vol.%). The mineral assemblage is composed of plagioclase, biotite, amphibole, quartz, clinopyroxene, Fe-Ti oxides, ±apatite and zircon as accessory phases. The groundmass of the Chac-Inca dacite is micro and crypto-crystalline locally glassy with interstitial devitrified glass . The Apacheta sample show micro-cryptocrystalline and highly vesiculated groundmass. Both rocks show the same mineralogical paragenesis of phenocrysts. Plagioclase phenocrysts are variably sized (from 0.3 mm up to 2 mm) with oscillatory zoning and composition range from An_{33} to An_{48}. Quartz crystals have rounded edges. Fe-Ti oxides are magnetite (Mgn_{87-90} Usp_{6-8} Spn_4) (Table 4.1a). Accessory phases are hosted as inclusions in hydrates minerals. Both lava domes contain frequent micro-vesiculated intermediate-basic enclaves composed by micro-phenocrysts of plagioclase, orthopyroxene, amphibole, biotite and Fe-Ti oxides (Fig. 4.3 c). Small-sized and acicular micro-phenocrysts habits

of Chach-Inca enclaves compared with relatively bigger sized and well developed micro-phenocrysts habits in Apacheta enclaves, suggest a different rate of cooling for both domes during the interaction between two different magmas. Bigger-sized plagioclases are also present with a composition range from An_{37} to An_{62} (Table 4.1a). They show sieve and resorption textures with overgrowth rims and inclusions of amphibole, biotite and Fe-Ti oxides sometimes with poikilitic textures. Probably they belonged to the dacite and subsequently they have been embedded by the enclave during the mingling processes.

Chanka dome is a dacite (66.2 wt% SiO_2, Piscaglia, 2011). CKA sample (Fig. 4.3 d) has porphyritic and partially seriate texture (P.I.=30-35 vol.%). The phenocrysts are, in order of abundance, plagioclase, biotite, amphibole, quartz, pyroxene and Fe-Ti oxides. The groundmass is micro-cryptocrystalline, locally glassy with perlitic cracks. Plagioclase phenocrysts are variable sized (from 0.3 mm up to 4 mm) with composition ranging from An_{35} to An_{54}. Generally, they have a fresh appearance although weak coarse-sieve texture and smooth edges, probably linked to resorption processes, are locally observed. Sometimes they are poikilitic enclosing crystals of biotite. Quartz crystals have rounded edges. Pyroxenes have enstatic compositions (Wo_{2-3} En_{80-81} Fs_{16-17}). Fe-Ti oxides are magnetite (Mgn_{85-88} Usp_{6-8} Spn_4) with chromite content up to 5% (Table 4.1a). Euhedral to subhedral large sized-hydrate minerals (up to 2 mm) can be affected by intense breakdown that sometimes replace the entire mineral with pseudomorph crystal composed by plagioclase and pyroxene assemblage. Holocrystalline, fine-grained and micro-vesiculate-textured intermediate-basic enclaves (Fig. 4.3 e) are common in the dacite lavas (e.g. CKA1a and CKA1b samples). They have a mineral assemblage composed of quench and acicular phases such as plagioclase (An_{35} to An_{42}), a more ferric pyroxene (Wo_{1-3} En_{69-78} Fs_{19-30}), compared to hosting dacite, and amphibole. Fe-Ti oxides (Mgn_{85-91} Usp_{6-11} Spn_{3-5}; with chromite content less than 0.3%) (Table 4.1a) and traces of biotite and quartz are present. The plagioclases are affected by sieve and resorption textures with overgrowth rims. Their habits, size and textural relations with other crystals, suggest they belong to the hosting dacite. These enclaves represent, together with convoluted banded textures of AAVC rhyolite lava, mixing/mingling episodes between magmas with different compositions and physical parameters that could have generated, to some extent, disequilibrium conditions. Micro-vesiculate texture are evidence of gas exsolution, rapid undercooling and high nucleation rate due to the intrusion in a silicic body of a hotter basic magma coming from deeper zones.

La Torta dome is classified as rhyolite [71.7 wt% SiO_2, Piscaglia, 2011). CT1a (Fig. 4.3 f) and TA12 samples have a porphyritic texture (P.I.=30-35%) with a mineral assemblage composed by plagioclase, quartz, biotite, amphibole and Fe-Ti oxides, apatite, zircon and titanite as accessory phases. It is mainly characterized by a glassy groundmass with perlitic cracks but locally show an oxidized cryptocrystalline matrix, in which are

immerged angular phenocrysts of plagioclase, quartz, biotite and amphibole. Plagioclase phenocrysts range from An_{37} to $An_{66.}$ They are characterized by sub-euhedral to anhedral habits with size up to 2 mm and are affected by sieve and resorption textures with direct, inverse and oscillatory zoning. Fe-Ti oxides, zircon, biotite and amphibole appear as common inclusions in plagioclase. Quartz crystals exhibit anhedral habits with common rounded edges and embayed contours. Fe-Ti oxides exhibit massive and elongated habits related, respectively, to magnetite (Mgn_{92-94} Usp_{2-5} Spn_{3-4}; with chromite content less than 0.4%) and ilmenite (Table 4.1a). Biotite is a common phase and some of them have Fe-Ti oxides and plagioclase reaction rims.

In CGA, the Pucarà dome is a calc-alkaline andesite (60 wt% SiO_2, Comida, 2012) (Fig. 4.2). CH17 sample (Fig. 4.3 g) has a porphyritic texture (P.I.=25 vol%) and a phenocrystic assemblage composed by amphibole, plagioclase, Fe-Ti oxides, traces of clinopyroxene and orthopyroxene (as microphenocrysts). The groundmass is micro/criptocrystalline with rare interstitial glass and locally pilotassitic texture. It is composed by the same mineralogical paragenesis of phenocrysts and SiO_2 patches, probably tridymite. Apatite is found as micro-inclusions in amphibole. Plagioclase phenocrysts compositions range from An_{60} to An_{78}. They are less than 1mm in size, show euhedral to anhedral habits and rare sponge textures. Pyroxenes have augitic (Wo_{37-41} En_{43-48} Fs_{15-16}) and enstatitic compositions (Wo_3 En_{71} Fs_{26}). Fe-Ti oxides are magnetite and Ti-magnetite (Mgn_{52-71} Usp_{17-39} Spn_{8-11}) with chromite content less than 0.06% (Table 4.1b).

Pyroclastic products (Fig. 4.3 h) (CH22, CH23, CH24, CH27 samples) are classified as andesites on petrographic and modal mineralogy bases. They show similar petrographic characteristics, regardless of sampling location (see section 3.2.2). They have similar porphyritic indexes (10-13 vol%) and a phenocrystic assemblage mainly consisting of plagioclase, amphibole and Fe-Ti oxides. The micro-cryptocrystalline and micro-vesiculated groundmass is composed by the above-mentioned phases, traces of biotite and apatite and SiO_2 patches, probably tridymite. Only one section from the lower event is characterized by higher porphyritic index, up to 20 vol%, and traces of clinopyroxene micro-phenocrysts. Plagioclase phenocrysts compositions range from An_{26} to An_{56}. They are variable-sized, from 0.2 mm up to 2.5 mm, with subhedral to euhedral habits and rare sponge textures. All the samples are generally characterized by direct, inverse and oscillatory zoning. Small inclusions of apatite and biotite are occasionally found. Fe-Ti oxides are magnetite and Ti-magnetite (Mgn_{19-87} Usp_{8-77} Spn_{4-7}) with chromite content less than 0.12% (Table 4.1b). The lack of pyroxenes, the appearance of biotite, although rare and not easily distinguishable from amphibole microlites and the lower Ca content in plagioclase phenocrysts, suggest that these products are more evolved compared to Pucarà dome andesite and could have a chemistry composition similar to the pyroclastic products studied by Bernard et al. (2014).

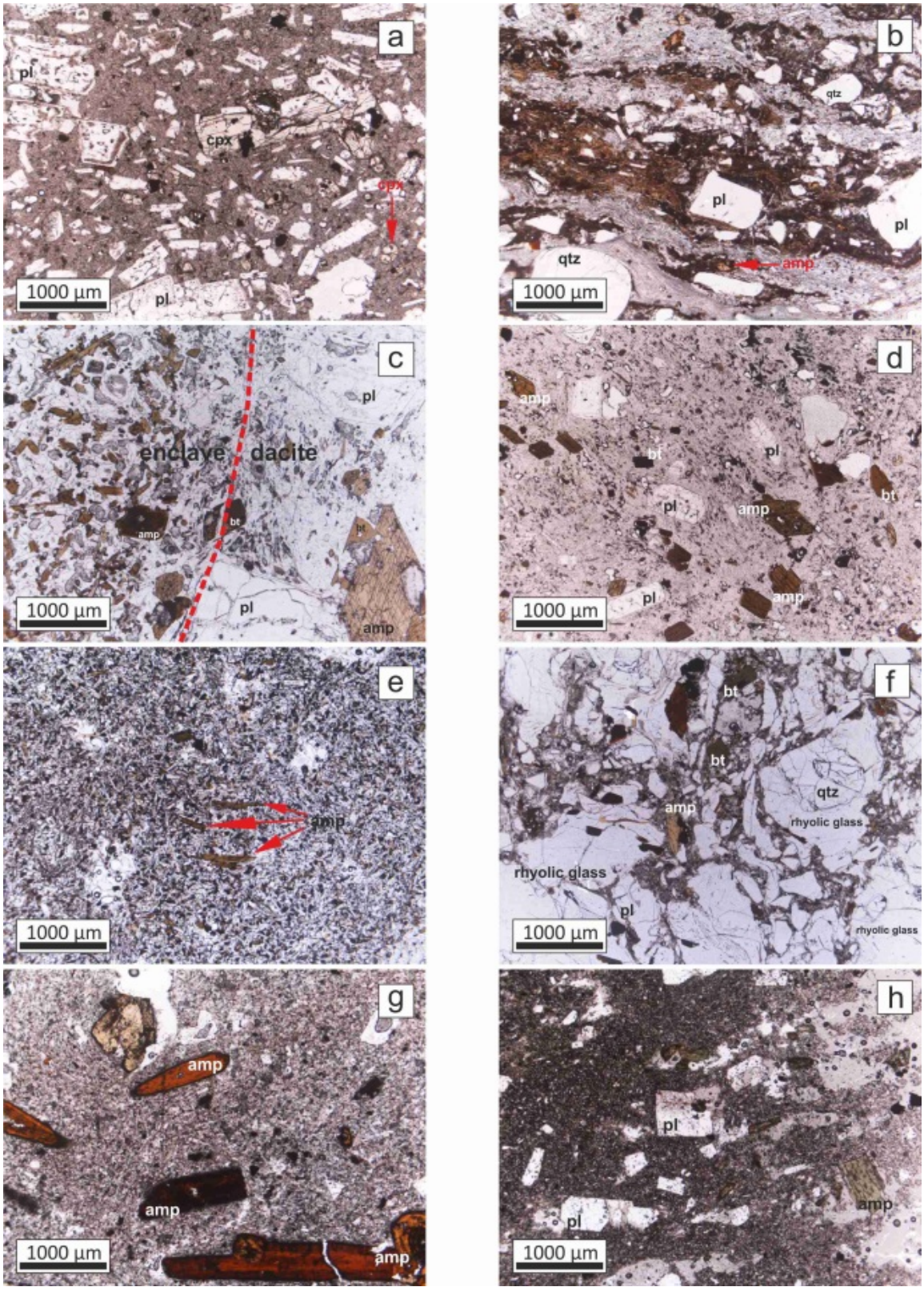

Fig. 4.3. Photomicrograph of selected thin section textures. a) andesite lava of AAVC; b) rhyolite lava of AAVC with banded texture; c) Apacheta dome with contact between intermediate-basic enclave and hosting dacite; d) Chanka dome; e) holocrystalline, fine-grained and micro-vesiculate-textured intermediate-basic enclave; f) La Torta dome; g) Pucarà dome; h) typical texture of juvenile ejecta of Pucarà dome pyroclastic deposits.

4.4.2 Amphibole texture and classification

Amphibole phenocrysts from AAVC andesite (AA010) and rhyolite (AA064) lava flows are affected by breakdown texture (composed of plagioclase, pyroxene and magnetite) or coarse-grained reaction rim (composed of pyroxene). Pervasive fine-grained resorption textures can also be present (Fig. 4.4 a, b). Zoning textures are not frequent. Dome-related crystals (Apacheta, Chac-Inca, Chanka and La Torta) are variable-sized from 0.2 to 1.5 mm but they can exceed 2mm, with subhedral to euhedral habits. They show a green-brownish pleochroism and usually, are not affected by evident reaction or breakdown textures. Large poikilitic crystals are present. Plagioclase, biotite, Fe-Ti oxides and zircon can occur as inclusions. Amphiboles hosted in the intermediate-basic enclaves are affected by alteration or can be totally replaced by pseudomorph minerals. Zoning texture characterized by a dark brownish core and a pale brownish rim can be present (Fig. 4.4 c).

CGA dome-related amphiboles are variable-sized, commonly ranging from 1 to 3 mm but in some cases up to 6 mm (Fig. 4.4 d) with euhedral and anhedral habits characterized by rounded edges. They typically show pale yellow to brown-reddish and brown pleochroism with no evident optical zoning. The larger crystals show subhedral-elongated shapes (Fig. 4.4 d) with a sort of hopper morphology (with a negative crystal cavity) suggesting undercooling and fast growth conditions (Shea and Hammer, 2013). The reddish colours of the crystals is most probably the result of syn/post-eruptive oxidation which commonly induced the formation of thin opacitic rims of breakdown (thickness <25 μm) (Fig. 4.4 d, e) characterized by fine-grained intergrowth of clinopyroxene, plagioclase and Ti-magnetite. Broader opacitic rims of breakdown (thickness >25 μm) or pervasive breakdown textures in the crystal core can also occur.

Amphibole phenocrysts in the pyroclastic deposit look quite different from the dome-related amphiboles (Fig. 4.4 f). They are variable-sized, ranging from 0.3 to 1 mm and sometimes up to 2 mm. They show subhedral to euhedral habits with pale yellow-green pleochroism. Breakdown textures are not present. “Cycling” zoning with alternating dark and light greenish layers is common (Fig. 4.4 f). Sometimes the zoning can be described as “patchy”.

Mineral formulas were calculated with the Amp-TB-xls spreadsheet (Ridolfi et al., 2010a) using the 13 cations method, also known as the 13eCNK method (Leake et al., 1997) (Tab 4.2a, b). AGA, TGA and CGA amphiboles belong to the group of calcic amphiboles (i.e. $^{B}Ca>1.5$) with $^{B}Na<0.5$, $Mg/(Mg+Fe^{2+})>0.5$ and $Ti<0.5$ apfu (i.e. atoms per formula unit).

Figure 4.5 (a, b) shows the classification of amphiboles according to Leake et al. (1997). CGA amphiboles belong almost entirely to tschermakite group ($^{[4]}Al>1.5$, $Ti<0.5$ and $^{A}(Na+K)\leq0.5$ apfu) (83% of dataset) while the remaining amphiboles are Mg-horneblende ($^{[4]}Al\leq1.5$ and $Ti<0.5$) (17% of dataset). The situation is the opposite for AGA amphiboles with the most consistent group represented by Mg-horneblende (81% of dataset) then Mg-hastingsite group ($^{[4]}Al>1.5$, $Ti<0.5$,

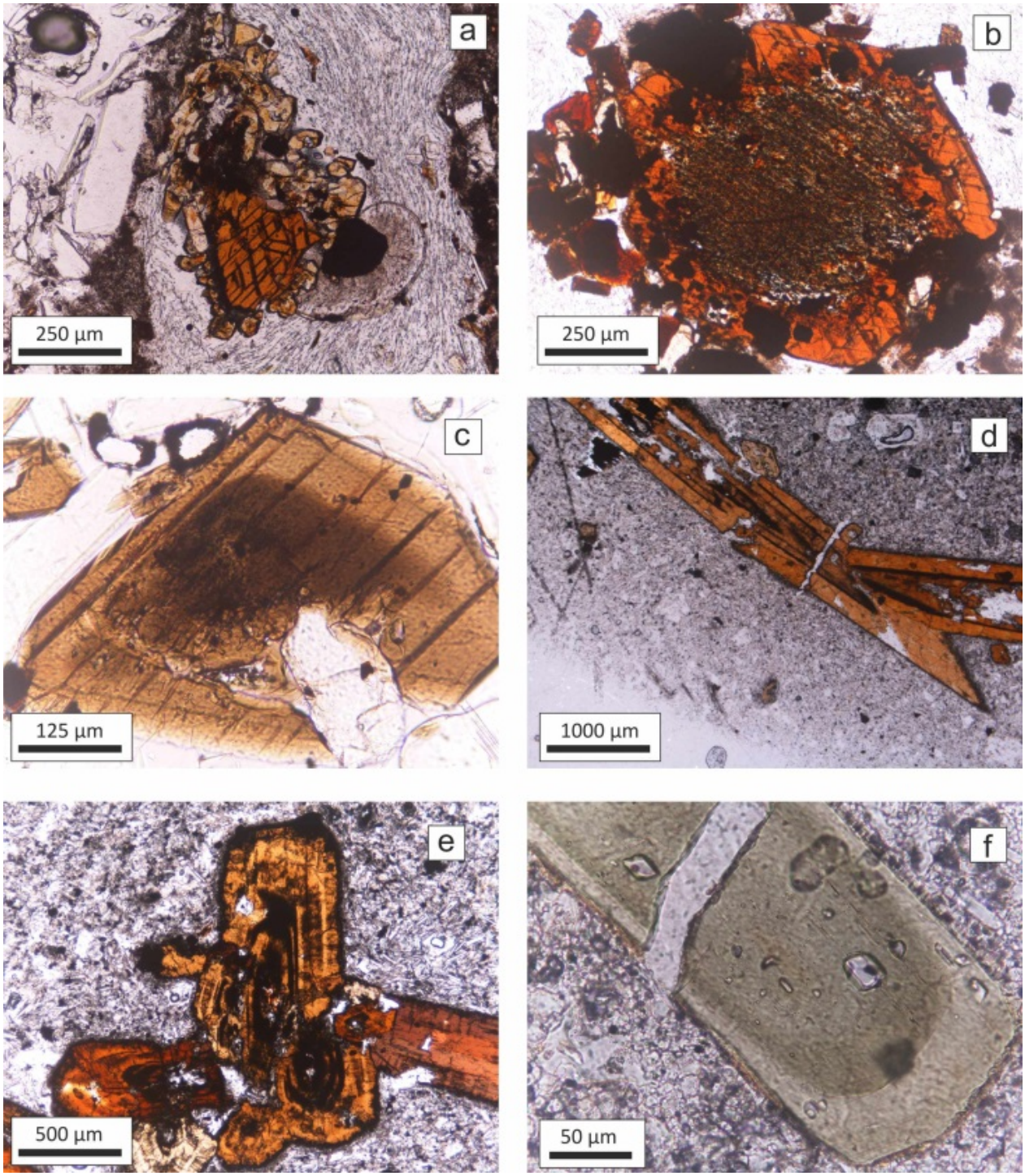

Fig. 4.4. Representative photomicrographs of amphibole textures . a) Coarse-grained reaction rim formed mainly by pyroxene and b) fine-grained pervasive resorption textures in amphiboles of rhyolite lava of AGA. c) Typical zoned crystal with brownish dark core and brownish pale rim found in intermediate-basic enclaves of Apacheta dome (AGA). d) and e) large-sized reddish coloured amphiboles with elongated shape of Pucarà dome (CGA). Breakdown texture is evident. f) greenish coloured amphibole in the pyroclastic deposit of Pucarà dome. Breakdown texture is absent but concentric optical zoning is evident.

^{A}(Na+K)>0.5 apfu and $^{[6]}$Al<Fe^{3+}) (13%) of dataset (Fig. 4.5b) and tschermakite (6%) of dataset. TGA amphiboles are almost entirely classified as Mg-horneblende (91% of dataset). According to Ridolfi et al. (2010a) and Ridolfi et al. (2012) all the amphibole falling in the tschermakite field are renamed tschermakitic pargasites..

4.5 DISCUSSION

4.5.1 Compositional-textural relationship of amphiboles.

Representative core to rim compositional profiles (SiO_2, Na_2O, TiO_2, MgO, FeO, Al_2O_3) of selected amphiboles are reported in Figure 4.6. By definition. zoned crystals are not homogeneous in composition. Chemical variations occur according to optical zoning within the crystal (Fig. 4.6 a, b, c). Generally, dark greenish sectors have lower SiO_2, TiO_2, MgO and higher Al_2O_3, FeO compared to the light greenish sector with higher SiO_2, TiO_2, MgO and lower Al_2O_3, FeO. By contrast, Na_2O do not show an univocal correlation with optical zoning (Fig. 4.6 a, b, c). Homogeneous amphiboles show chemical variations roughly within the analytical uncertainties (Fig. 4.6 d). According to the general SiO_2-Al_2O_3 inverse relation of calcic amphiboles (Ridolfi et al. 2010a) the oscillatory zonings are characterized by alternating decreases and increases in major elements (e.g. Fig. 4.6 a). This phenomenon

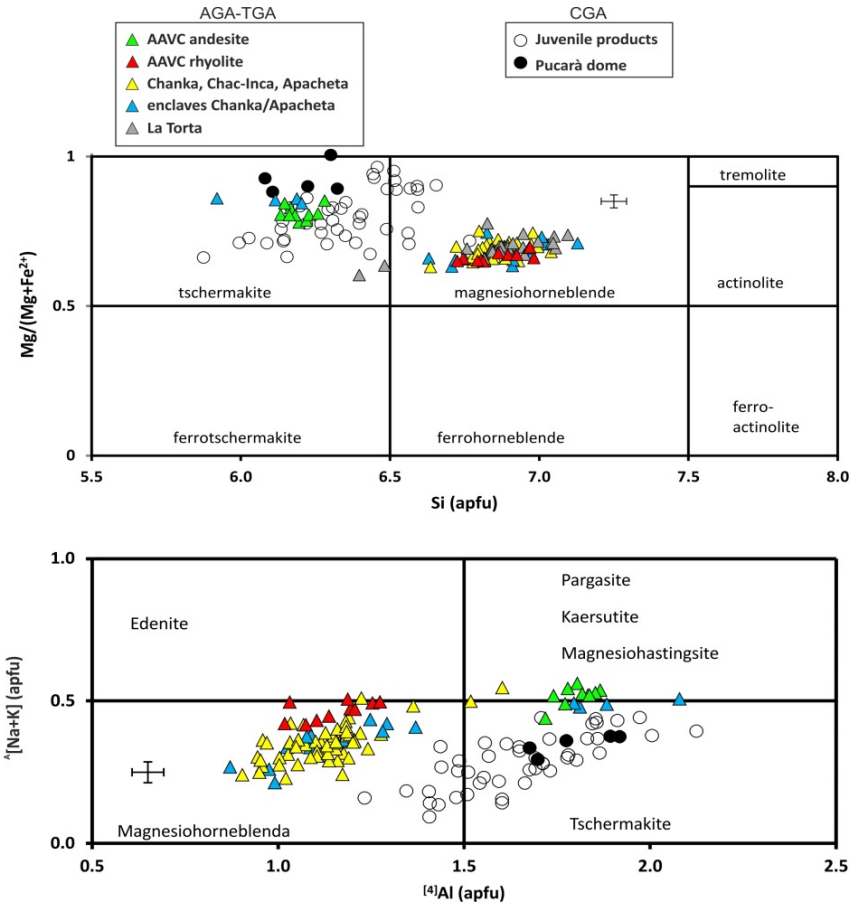

Fig. 4.5. a) Si vs Mg/(Mg+Fe^{2+}) and b) $^{[4]}$Al vs ^{A}[Na+K] classification diagrams of AGA, TGA and CGA amphiboles according to Leake et al. (1997). The horizontal and vertical black bar indicates the average values of standard deviation of amphiboles analysis.

Table 4.2a. Representative compositions and physico-chemical conditions of the AGA and TGA amphiboles.

Site	AAVC			Apacheta			Chac-Inca	Chanka			La Torta		
Sample	AA010	AA064		CPBa			CINKA1	CKA1	CKA1b		CT1a		
Host	andesite	rhyolite		dacite		andesite	dacite	dacite	andesite		rhyolite		
Type	lava flow	lava flow		lava dome		enclave	lava dome	lava dome	enclave		lava dome		
Mineral	mg-hst	mg-hbl	mg-hbl	mg-hbl	mg-hbl	tsc-prg	mg-hbl	mg-hbl	mg-hbl	mg-hst	mg-hbl	mg-hbl	mg-hst
Texture	phen	phen c	phen r	phen c	phen r	phen	phen	phen	phen	phen	phen c	phen r	phen c
SiO_2	42.09	46.32	47.66	44.75	47.25	43.21	46.42	46.47	49.37	41.03	46.95	48.67	43.06
TiO_2	2.77	1.34	1.19	2.02	1.50	2.62	1.52	1.56	0.97	4.09	1.61	1.20	2.62
Al_2O_3	12.07	7.93	7.06	9.28	7.33	11.89	7.69	7.44	6.03	13.29	7.89	6.68	10.87
Cr_2O_3	0.04	0.02	0.00	0.00	0.00	0.01	0.00	0.04	0.00	0.01	0.01	0.05	0.10
FeO_{tot}	11.62	15.33	12.80	14.91	14.00	11.02	15.28	14.85	13.20	10.56	14.13	13.43	15.37
MnO	0.12	0.54	0.43	0.46	0.47	0.19	0.47	0.48	0.51	0.13	0.43	0.46	0.35
MgO	13.77	12.53	14.06	11.81	13.67	14.88	12.64	12.97	14.32	14.34	13.11	13.81	11.02
CaO	11.28	11.83	11.90	11.69	11.80	11.55	11.79	11.93	12.29	11.21	11.60	12.04	11.65
Na_2O	2.21	1.44	1.70	1.59	1.26	2.17	1.35	1.20	0.96	2.36	1.38	1.12	1.87
K_2O	0.66	1.08	0.79	0.89	0.54	0.56	0.79	0.78	0.53	0.61	0.82	0.63	0.81
F	-	-	-	-	-	-	-	-	-	-	-	-	-
H_2O_{calc}	1.93	1.93	1.94	1.91	1.95	1.98	1.93	1.93	1.96	1.96	1.94	1.95	1.90
Total	98.56	100.27	99.55	99.29	99.77	100.10	99.88	99.66	100.15	99.59	99.87	100.04	99.63
Standard deviations of element oxides calculated on homogeneous domains inside the amphiboles													
σSiO (wt%)	0.17	0.31	-	0.02	-	0.05	0.13	0.09	-	0.29	0.38	0.47	-
σTiO_2 (wt%	0.07	0.08	-	0.02	-	0.06	0.08	0.09	-	0.10	0.12	0.02	-
σAl_2O_3 (wt%	0.19	0.26	-	0.07	-	0.21	0.20	0.09	-	0.04	0.35	0.15	-
σFeO (wt%	0.40	0.39	-	0.17	-	0.02	0.39	0.15	-	0.04	0.38	0.03	-
σMgO (wt%	0.21	0.27	-	0.03	-	0.37	0.20	0.30	-	0.10	0.38	0.21	-
σCaO (wt%	0.14	0.14	-	0.10	-	0.11	0.12	0.07	-	0.32	0.08	0.06	-
σNa_2O (wt%	0.03	0.09	-	0.05	-	0.07	0.04	0.01	-	0.07	0.01	0.06	-
σK_2O (wt%)	0.04	0.07	-	0.11	-	0.03	0.08	0.03	-	0.05	0.07	0.03	-
Formula on the basis of 13 cations (Leake et al., 1997)													
Si	6.163	6.794	6.969	6.636	6.863	6.189	6.808	6.818	7.129	5.92	6.843	7.055	6.4
$^{[4]}Al$	1.837	1.206	1.031	1.364	1.137	1.811	1.192	1.182	0.871	2.08	1.157	0.945	1.6
$^{[6]}Al$	0.247	0.164	0.185	0.258	0.117	0.196	0.136	0.105	0.155	0.180	0.199	0.195	0.3
Ti	0.305	0.148	0.131	0.225	0.164	0.282	0.167	0.172	0.106	0.444	0.177	0.131	0.29
Fe3+	0.685	0.416	0.225	0.318	0.568	0.798	0.487	0.491	0.334	0.770	0.440	0.308	0.3
Fe2+	0.738	1.464	1.341	1.531	1.133	0.522	1.388	1.331	1.260	0.505	1.282	1.320	1.61
Mn	0.015	0.067	0.054	0.058	0.058	0.023	0.059	0.060	0.063	0.015	0.053	0.057	0.04
Mg	3.006	2.739	3.065	2.611	2.961	3.177	2.763	2.837	3.083	3.085	2.849	2.983	2.44
Ca	1.771	1.859	1.865	1.857	1.835	1.773	1.852	1.876	1.902	1.73	1.812	1.871	1.85
^{B}Na	0.229	0.141	0.135	0.143	0.165	0.227	0.148	0.124	0.098	0.27	0.188	0.129	0.15
^{A}Na	0.397	0.269	0.348	0.314	0.189	0.376	0.235	0.217	0.170	0.4	0.201	0.186	0.39
K	0.123	0.201	0.147	0.169	0.101	0.102	0.147	0.145	0.098	0.11	0.152	0.117	0.15
F	-	-	-	-	-	-	-	-	-	-	-	-	-
OH_{calc}	2.000	2.000	2.000	2.000	2.000	2.000	2.000	2.000	2.000	2.000	2.000	2.000	2.000
Physico-chemical conditions (Ridolfi & Renzulli, 2012)													
T(°C)	943	800	790	828	794	948	791	793	742	1011	798	760	872
P(MPa)	403	139	114	189	125	392	130	126	92	508	141	107	267
ΔNNO	1.7	1.2	1.9	0.3	0.2	1.8	0.3	0.3	0.6	0.8	0.8	0.6	-0.5
$logfO_2$	-9.4	-12.7	-12.2	-13	-13.8	-9.1	-13.7	-13.7	-14.6	-9.2	-13.1	-14.1	-12.9
H_2O_{melt} (wt%	6.0	5.8	5.3	6.0	5.7	5.9	5.9	5.9	6.2	4.6	5.8	6.0	6
Depth (km)	15.8	5.5	4.5	7.4	4.9	15.4	5.1	5.0	3.6	19.9	5.5	4.2	10.5

Table 4.2b. Representative compositions and physico-chemical conditions of the CGA amphiboles.

Site	LPD*						UPD**	
Sample	CH22J				CH24J1	CH30J1	CH27J1	
Host	andesite						andesite	
Mineral	tsc-prg	tsc-prg	tsc-prg	tsc-prg	mg-hbl	tsc-prg	tsc-prg	mg-hbl
Texture	phen c	phen	phen c	phen r	phen	phen	phen c	phen r
SiO_2	44.25	42.58	40.86	43.52	44.94	43.29	43.53	46.99
TiO_2	0.88	1.92	1.88	1.54	0.89	0.98	0.87	1.27
Al_2O_3	11.14	12.04	13.94	11.81	9.26	11.79	11.72	9.15
Cr_2O_3	0.00	0.02	0.02	0.03	0.01	0.01	0.01	0.05
FeO_{tot}	15.44	14.13	16.76	12.55	16.39	15.73	16.59	11.63
MnO	0.26	0.15	0.26	0.1	0.45	0.26	0.32	0.14
MgO	12.49	13.12	10.5	13.88	12.36	12.02	11.64	15.55
CaO	10.69	10.87	10.7	11.31	11.17	10.74	10.91	11.06
Na_2O	1.74	2.2	2.12	2.15	1.53	1.79	1.66	1.62
K_2O	0.38	0.33	0.50	0.46	0.48	0.44	0.50	0.35
F	0.02	0.13	0.14	0.14	0.15	0.10	0.09	0.11
H_2O_{calc}	1.95	1.90	1.87	1.89	1.87	1.90	1.91	1.95
Total	99.24	99.39	99.55	99.38	99.5	99.05	99.75	99.87
Standard deviations of element oxides calculated on homogeneous domains inside the amphiboles								
σSiO (wt%)	0.21	0.25	0.20	0.07	0.10	0.21	0.19	0.17
σTiO_2 (wt%)	0.05	0.15	0.04	0.03	0.03	0.09	0.03	0.01
σAl_2O_3 (wt%)	0.42	0.12	0.23	0.17	0.13	0.23	0.12	0.08
σFeO (wt%)	0.20	0.23	0.11	0.09	0.12	0.15	0.13	1.06
σMgO (wt%)	0.15	0.21	0.18	0.19	0.09	0.21	0.20	0.74
σCaO (wt%)	0.20	0.13	0.03	0.12	0.08	0.04	0.04	0.15
σNa_2O (wt%)	0.03	0.10	0.07	0.07	0.05	0.08	0.03	0.07
σK_2O (wt%)	0.03	0.05	0.02	0.03	0.04	0.04	0.03	0.01
Formula on the basis of 13 cations (Leake et al., 1997)								
Si	6.406	6.169	5.995	6.293	6.561	6.308	6.323	6.655
$^{[4]}Al$	1.594	1.831	2.005	1.707	1.439	1.692	1.677	1.345
$^{[6]}Al$	0.306	0.225	0.405	0.306	0.154	0.333	0.330	0.182
Ti	0.096	0.209	0.208	0.168	0.098	0.107	0.000	0.135
Fe3+	1.220	1.131	1.122	0.87	1.072	1.205	1.199	1.026
Fe2+	0.650	0.582	0.934	0.648	0.929	0.711	0.816	0.351
Mn	0.032	0.018	0.032	2.993	0.056	0.032	0.039	0.017
Mg	2.696	2.834	2.297	0.013	2.689	2.611	2.520	3.284
Ca	1.658	1.687	1.682	1.752	1.747	1.676	1.698	1678
^{B}Na	0.342	0.313	0.318	0.248	0.253	0.324	0.302	0.322
^{A}Na	0.146	0.307	0.285	0.356	0.179	0.181	0.166	0.122
K	0.071	0.061	0.093	0.085	0.088	0.081	0.092	0.062
F	0.008	0.059	0.063	1.935	0.071	0.045	0.040	0.049
OH_{calc}	1.992	1.941	1.937	0.065	1.929	1.955	1.960	1.951
Physico-chemical conditions (Ridolfi & Renzulli, 2012)								
T(°C)	843	912	907	889	819	855	843	842
P(MPa)	283	364	491	325	187	326	313	195
ΔNNO	1.0	0.9	-0.1	2.2	0.2	1.0	0.7	2.0
$logfO_2$	-11.9	-10.7	-11.7	-9.8	-13.2	-11.7	-12.2	-11
H_2O_{melt} (wt%)	8.2	6.8	8.3	7.4	7	8.7	9.1	6.3
Depth (km)	10.0	12.8	17.3	11.4	6.6	11.5	11.0	6.9

can be rapid, i.e. characterized by spikes and drops (e.g. Kiss et al. 2014) or gradual such as the intra-crystalline chemical variations of Fig. 4.6 a. A normal zoningis typically characterized by a stage of crystallization at constant conditions followed by a SiO_2 increase (and concomitant Al_2O_3 decrease) to the rim. An example of normal zoning is reported in Fig. 4.6 b also showing disequilibrium conditions during the very last crystallization stage, characterized by a rapid Al_2O_3 increase at the rim (most probably a syn-eruptive phenomenon). In theory, a reverse zoning should show the opposite of a normal zoning. The first 5 analytical spots of the crystal in Fig. 4.6 c show a similar phenomenon, characterized by an increase of Al_2O_3 (and SiO_2 decrease) toward the rim. However, this crystal should be referred as a complex or oscillatory zonings because the SiO_2 content increases at the last stage of crystallization. By contrast, homogeneous amphiboles show no significant intra-crystalline variation for both chemical composition and calculated intensive parameters (Fig. 4.6 d).

Indeed, Figure 4.6 also report the physico-chemical (P, T, ΔNNO) and compositional conditions ($SiO_{2\ melt}$, H_2O_{melt}) of amphiboles crystallization calculated with the R&R2012 method. P is closely related to major element variations and therefore to zoning of the amphibole with direct proportionality to Al_2O_3 and FeO and indirect proportionality to SiO_2 and MgO (Fig. 4.6 a, b, c). Temperature changes in a similar way to the pressure but with less pronounced variations. H_2O_{melt} changes accordingly to the pressure while ΔNNO and $SiO_{2\ melt}$ show an inverse correlation with pressure.

Large chemical variations within the crystals and rapid changes of physico-chemical parameters point out a crystallization of amphiboles at disequilibrium conditions. This is in agreement with petrographic observation of micro-vesiculated intermediate-basic enclaves within dome-related samples, convoluted banded textures in rhyolitic lava (i.e. AA064), zoned crystals and frequent sieve textures in plagioclase, which point out disequilibrium conditions ascribed to magma mixing/mingling processes.

These disequilibrium conditions are in contrast with R&R2012 model since that the equations are calibrated on amphiboles crystallized at equilibrium conditions which in turn mean homogeneous amphiboles crystallized at steady-state conditions. For this reason the method should be applied to crystal showing homogeneous composition or micro-domains with homogeneous composition of zoned amphiboles (Ridolfi et al., 2016). For this reason we compared the intra-crystal compositional variation with the standard error of homogeneous amphibole EMP analyses. As error reference we considered the average standard deviations (σ) of element oxides reported for the 61 experimental amphiboles used to retrieve the thermobarometric model (see Table 4.2 in Ridolfi and Renzulli 2012). Comparison of these values with the element oxide σ of homogeneous micro-domains (Ridolfi et al., 2010b; Ridolfi et al. 2016) indicate that they approximate well the typical uncertainty of

EMP amphibole analyses and thus can be used to evaluate compositional zonings. On this basis, EMP analyses performed on amphiboles showing chemical variability falling within R&R2012 average σ, have been regarded as compositionally homogeneous (i.e. crystallized at chemical equilibrium condition) and have been taken as one through the calculation of their average value. These average compositions were then used for the calculation of the physico-chemical and compositional parameters with the equations of R&R2012 (Table 4.2a, b). The values outside R&R2012 average σ ranges are generically ascribed to crystallization at disequilibrium conditions and were discarded.

In Figure 4.6 are reported the average σ of SiO_2, Na_2O, TiO_2, MgO, FeO, Al_2O_3 of the physico-chemical uncertainties of the R&R2012 method. In oscillatory zoned amphibole the chemical variability is larger than the average σ of R&R2012 and it is not easy to distinguish clear homogeneous micro-domains (Fig. 4.6 a) and the physico-chemical parameters calculated with this kind of data cannot be considered reliable. In normally zoned amphiboles the compositional variation is less pronounced showing element oxides variation lower than average σ of R&R2012 so that a homogeneous dark-greenish core with an average pressure of 313 MPa, average temperature of 843°C and ΔNNO +0.7 can be recognized (Fig. 4.6 b, red rectangles). At the optical zonation transition another homogeneous micro-domain can be observed with an average pressure of 195 MPa, average temperature of 842°C and ΔNNO +2.0 (Fig. 4.6 b, blue rectangles). The outer rim of the crystal, which is in contact with the groundmass, shows once again a rapid spike of pressure to 370 MPa, a significant increase of temperature to 884°C and a decrease of fO_2 (Fig. 4.6 b). The first pressure drop can be interpreted as depressurization condition due to magma ascent toward the surface which is consistent with a H_2O decrease and an enrichment of SiO_2 content in coexisting melt as shown in Figure 4.6b. Conversely, the sudden increase of pressure of about 170 MPa near the rim is simply due to sin-eruptive disequilibrium phenomena since that a pre-eruptive sink of the crystal of about 6 Km in the crust (considering a crustal density of 2.7g/cm^3) is not reliable. Crystal rims with P-T increases are commonly found in our amphiboles especially in micro-vesiculated enclaves of AGA volcanic products and represent evidence of disequilibrium conditions suffered by crystals during mixing/mingling processes. The amphibole with complex/oscillatory zoning chcraterized by reverse zoning at main core micro-domain (Fig. 4.6 c) shows the most reliable compositional values at the core. The average composition is then considered valulable for thermobarometric constraints. The homogeneous amphibole (Fig. 4.6 d) show compositional variations within the average σ of R&R2012. However, the outer rim shows a significant compositional change and a slight pressure drop that can be interpreted as a magma ascent phenomenon toward the surface, similar to the normal zoned amphibole in Figure 4.6 b.

Another disequilibrium condition to avoid is represented by fast growing textures which are present both in AGA and CGA amphiboles (Fig. 4.4 d). Recent undercooling experiments at 150 MPa carried out by Shea and Hammer (2013) make it possible to evaluate the behaviour of a model calibrated at conditions of physico-chemical equilibrium (i.e. R&R2012) in disequilibrium conditions. The experimental amphiboles, calculated with R&R2012 model, show slight temperature overestimations (6-27 °C, within the margin of error reported in R&R2012, ±24 °C) but pronounced pressure overestimations increasing with the cooling rate. In such a non-steady state context dominated an elevated thermal gradients, the crystallized amphibole show disequilibrium textures (e.g. acicular, elongate and hopper morphologies). Most probably these amphiboles record the compositional information of the liquid that was in equilibrium with the high pressure phases (i.e. at the temperature and pressure of the deep source). For these reasons, the application of the R&R2012 model to natural amphiboles showing similar morphologies should be evaluated carefully.

Substantially, during the application of the thermobarometric model, the chemical variations inside the crystals should be compared with the average σ in R&R2012 in order to identify homogeneous micro-domain indicating equilibrium condition. The intensive parameters calculated on the basis of chemical values should be evaluated on the basis of their reliability, as in the case of pressure drops due to ascent of magma. Data outside average σ or associated with zoned or fast-growing textured amphiboles should be discarded because if used for thermobarometric calculations they could lead to large overestimations of P and crystallization depth.

4.5.2 Amphibole thermobarometry application. The P-T-h diagram

Once we have cleaned up the database analyses from data considered synonymous with disequilibrium, we compared cation variation diagrams for CGA and AGA amphiboles with natural and experimental amphiboles used by R&R2012; they are in agreement and thus CGA and AGA data are suitable for the application of thermobarometer.

The calculated data were plotted in a pressure-temperature-depth (P-T-h) diagram which represents the storage and equilibrium crystallization conditions of amphibole in the different volcanic products (Fig. 4.7 a, b). Most of the data of the dacitic domes Chanka, Chac-Inca, Apacheta and La Torta are grouped in a pressure range between 97 and 144 MPa and temperature between 755 and 818°C (Fig. 4.7 a). The depth corresponding to the P values are between 3.8 and 5.6 km (the depth is calculated from average height of AGA and TGA, 4.63 Km; the average crustal density is 2.6 g/cm^3; Leidig & Zandt, 2003) indicating the presence of shallow magmatic chambers in the upper crust. Oxygen fugacity ranges between ΔNNO -0.1 to +1.4. Melt in equilibrium with amphiboles shows a H_2O content between 5.1-6.8 wt% and a SiO_2 content between 74.3-78.5 wt%. However, some amphiboles of Apacheta dome, show growth conditions slightly deeper with P

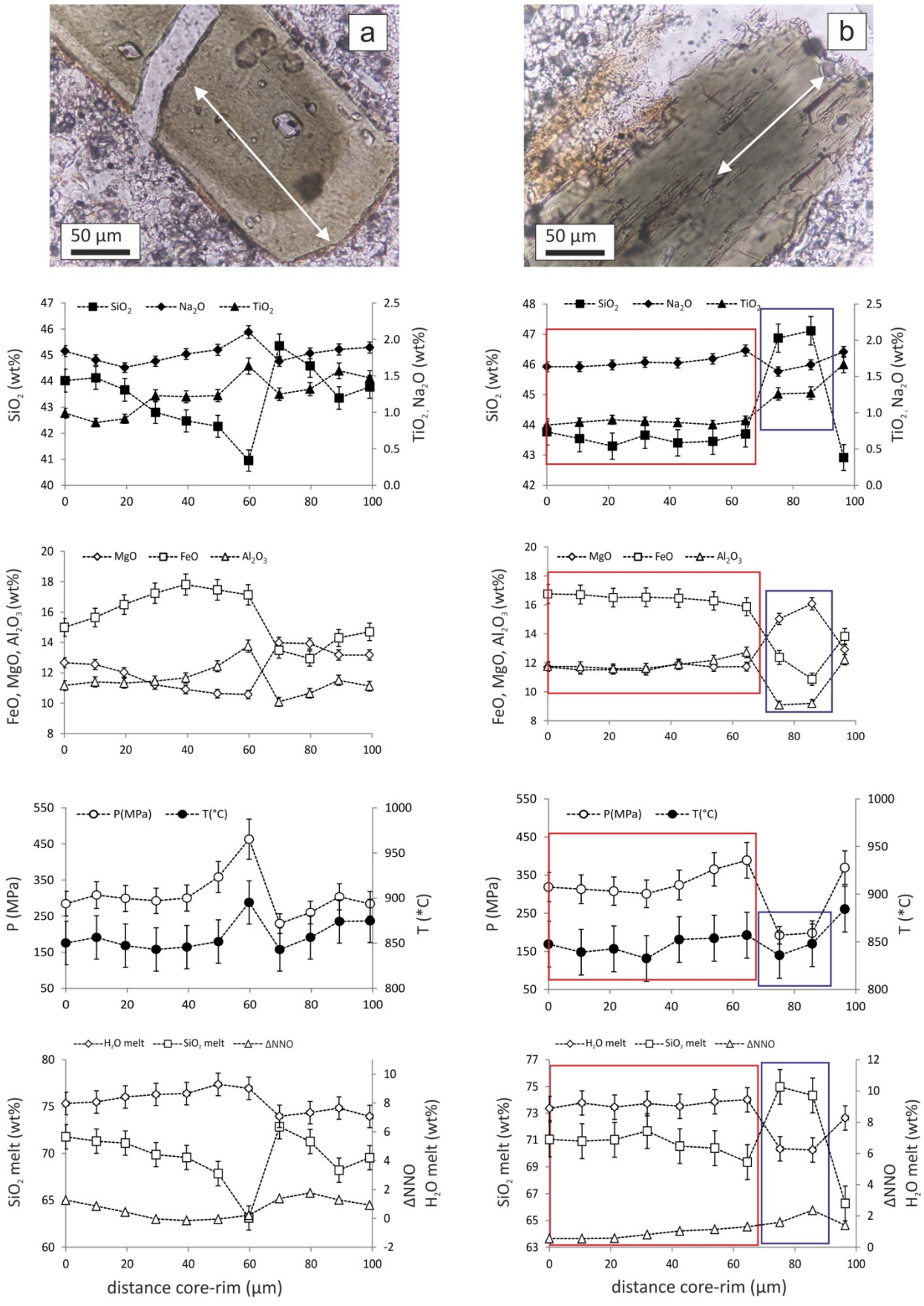

Fig. 4.6 a, b. (see caption ahead).

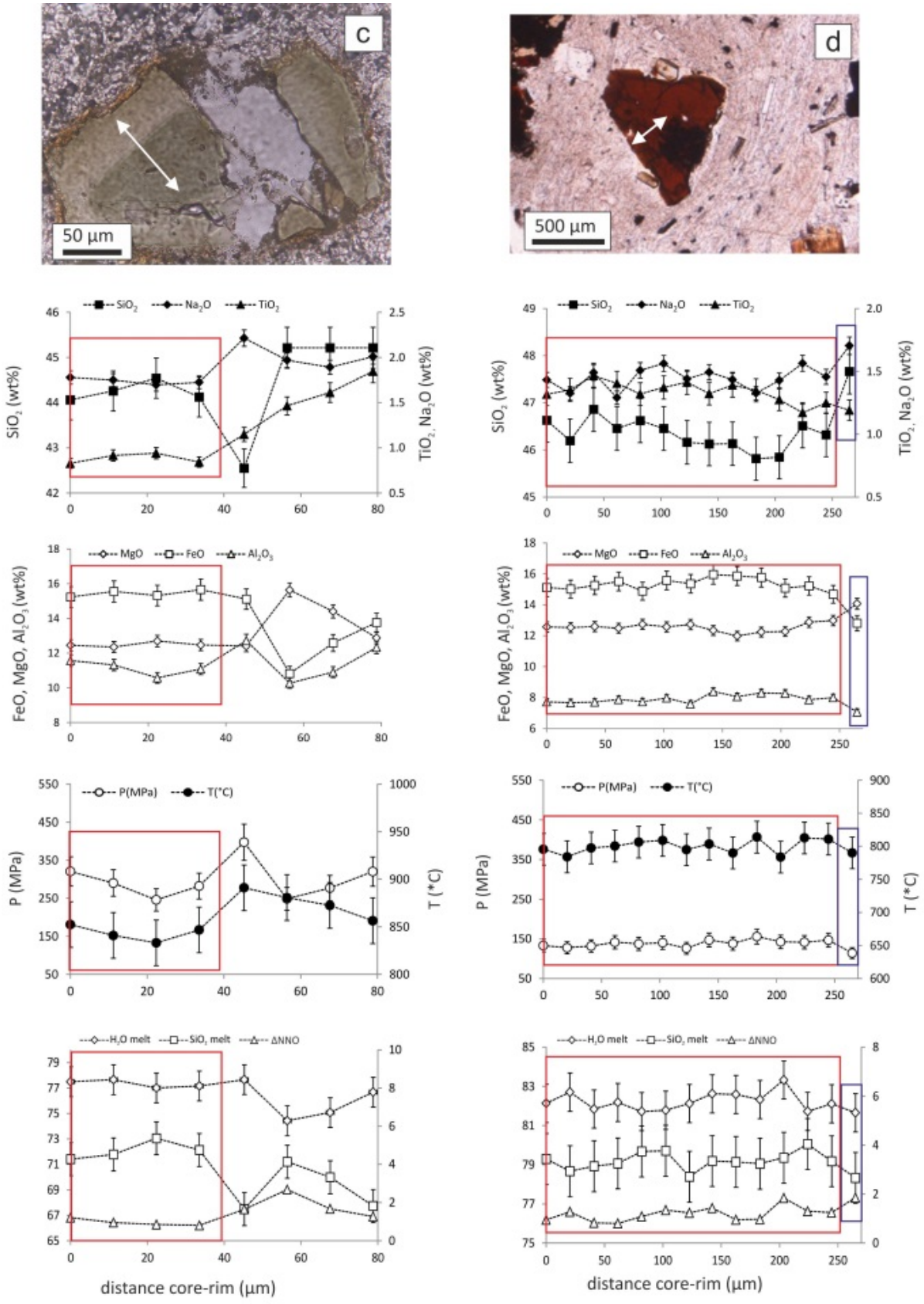

Fig. 4.6 c, d. (see caption ahead).

Fig. 4.6 a, b, c, d. Core to rim compositional profiles of selected amphiboles. a) oscillatory zoning, b) normally zoning with disequilibrium rim. Red and blue rectangle show homogeneous micro-domain within the amphibole. c) Inverse zoning with disequilibrium rim. d) Un-zoned amphibole. Optical zoning is correlated with element oxide variations. Pressure and temperature calculated with R&R2012 method change accordingly to chemical variation. R&R2012 method requires homogeneous crystals to retrieve reliable physico-chemical parameters. Average standard deviation (σ) of amphibole used in R&R2012 equation should be used to assess compositional variation within the studied crystals. Compositional variations falling outside the σ can be ascribed to disequilibrium condition suffered by the crystal and should be not used to retrieve P, T and chemometric parameters. Vertical black bars of SiO_2, Na_2O, TiO_2, MgO, FeO, Al_2O_3 indicate the average standard deviation (σ) of the experimental amphiboles in R&R2012. Vertical black bars if P, T, ΔNNO, SiO_2melt and H_2O melt, indicate the uncertainties (i.e. standard error of estimate) of R&R2012 method.

between 165 and 189 MPa (6.5-7.4 Km), T in the range 820-828 °C (Fig. 4.7 a), ΔNNO +0.9 to +0.3. They arein equilibrium with a rhyolitic melt containing 6.0 wt% H_2O and 74.5-76.7 wt% SiO_2. At greater depth are some amphiboles of La Torta dome with a 248-267 MPa pressure range (9.7-10.5 Km), T between 850 and 872 °C and redox condition of ΔNNO +0.6 to -0.5. The coexisting liquid shows a higher H_2O content (up to 6.6 wt%) and a less evolved composition (68.4-70.6 wt%).

Amphiboles belonging to lava erupted by AAVC are distributed in two separate groups. Not surprisingly, evolved product such as rhyolite lava (AA-064) includes amphiboles with low P (114-150 MPa; depth 4.5-5.9 km) and T (778-808 °C) (Fig. 4.7 a), and redox conditions in the range 0.8≤ΔNNO≤1.9. Coexisting melt show the most evolved composition with 78.3-79.8 wt% SiO_2 content and 5.3-5.9 H_2O content. High silica andesite lava (AA-010) contains amphiboles with higher P-T values that can be further subdivided in two sub-groups: the first one with P-T values between 383-435 MPa (15-17 Km) and 938-959 °C, the second one is in equilibrium with lower values in the range 318-323 MPa (12.5-12.7 km) and 927-936°C (Fig. 4.7 a). Oxygen fugacity shows the higher values with ΔNNO +1.4 to 2.1. Coexisting melt has a SiO_2 content between 61.8-65.6 wt% and H_2O content between 5.0-6.1 wt%.

Black arrow in Figure 4.7a highlight the core-rim path of normal zoned amphibole with a core in equilibrium at 189 MPa (about 7.4 km) and a rim at 125 MPa (about 4.9 km).

Amphiboles of the basic-intermediate enclaves in the Chanka and Apacheta domes overlaps the P-T path of dome-related amphiboles of Apacheta, Chac-Inca and Chanka domes with P range between 92-194 MPa (depth 3.6-7.6 km), T range of 742-837 °C and similar oxygen fugacity (ΔNNO -0.5 to +1.6). SiO_2 and H_2O content in coexisting melt is 72.1-79.2 wt% and 5.6-7.1 wt%, respectively. These amphiboles most probably crystallized in a silicic magma body and fell into the enclave during ma interaction with the basic magma. Indeed, a group of crystals in the enclaves is plotted at greater P-T condition between 375-392 MPa (14.7-15.4 km) and 948°C in higher oxidation condition (ΔNNO +1.8). SiO_2 and H_2O content in coexisting melt is 62.1-63.4 wt% and 5.5-6.1 wt%, respectively. One crystal show even higher P-T conditions, 505 MPa (about 20 km) and 1011 °C (Fig. 4.7 a), with ΔNNO +0.8

and coexisting melt with 54.3 wt% SiO_2 and 4.6 wt% H_2O.

These data indicate that the dome-related magmas were stored in different magma chambers placed at different depths in the crust.

P-T data for CGA show a more scattered pattern (Fig. 4.7 b). Most of the amphiboles belonging to pyroclastic products show crystallization pressure between 187-364 MPa corresponding to depth of about 6.6-13 Km (the depth is calculated from the peak of Pucarà dome, 3.041 Km; the average crustal density is 2.9 g/cm^3; Feininger and Seguin, 1983: unlike the AGA and TGA, the basement rocks of CGA are formed by oceanic crust, therefore the average crustal density is probably higher than AGA) and temperature between 819-912 °C. Oxygen fugacity ranges between ΔNNO +0.2 to 3.0. Melt in equilibrium with amphibole has SiO_2 content between 65.5-76.3 wt% and H_2O content between 5.5-9.7 wt%. The black arrow in Figure 4.7 b shows the general path of P-T variations on core-rim transect of zoned amphiboles. The lack of breakdown textures may be linked to the eruptive style of such pyroclastic products. They were ejected during a later blast and may have reached the surface as quickly as not to allow the formation of breakdown textures.

All the amphibole crystals from Pucará lava dome are affected by fast-growing textures ascribed to rapid undercooling (Shea and Hammer, 2013) (Fig. 4.1.1) and thus do not represent crystallization at total equilibrium conditions, thereby related thermobarometric and chemometric results were discarded.

4.5.3 Comparison between thermobarometric and geophysical constraints

In order to test the reliability of R&R2012 method, it was carried out a comparison between thermobarometric data of AGA and TGA with the geophysical results for the APVC. The APVC is characterized by a laterally extensive seismic low-velocity zone (LVZ) located at depth of about 17-19 km below sea level referred to as Altiplano-Puna Magma Body (APMB) (Chmielowsky et al., 1999; Leidig and Zandt, 2003; Zandt et al., 2003) with an inferred percentage of melt of 5-10%, temperature below 1000°C and felsic composition (Beck and Zandt, 2002). The extension of APBM, its spatial relations with the large caldera forming ignimbrites and its chemical-physical conditions, suggest it can be considered the intrusive equivalent of the APVC volcanic products (de Silva et al., 2006). Recently, Ward et al. (2014), presented a new 3-D seismic images of the APVC crust considerably improving the extension and morphology of the APMB. They identified a ~200 km diameter large and ~11 km thick LVZ below the APVC, with an inferred percentage of partial melt up to 25% and a much larger volume (~500,000 Km^3) than previous estimates. We plotted our thermobarometric data in a cross-section of the joint ambient noise-receiver function inversion S-velocity model performed by Ward et al. (2014) that show the depth and lateral extent of 2.9 km/s and 3.2 km/s velocity contour with an estimated percentage of melts respectively of ~10% and~4% (Fig. 4.8a). Since that AGA and TGA

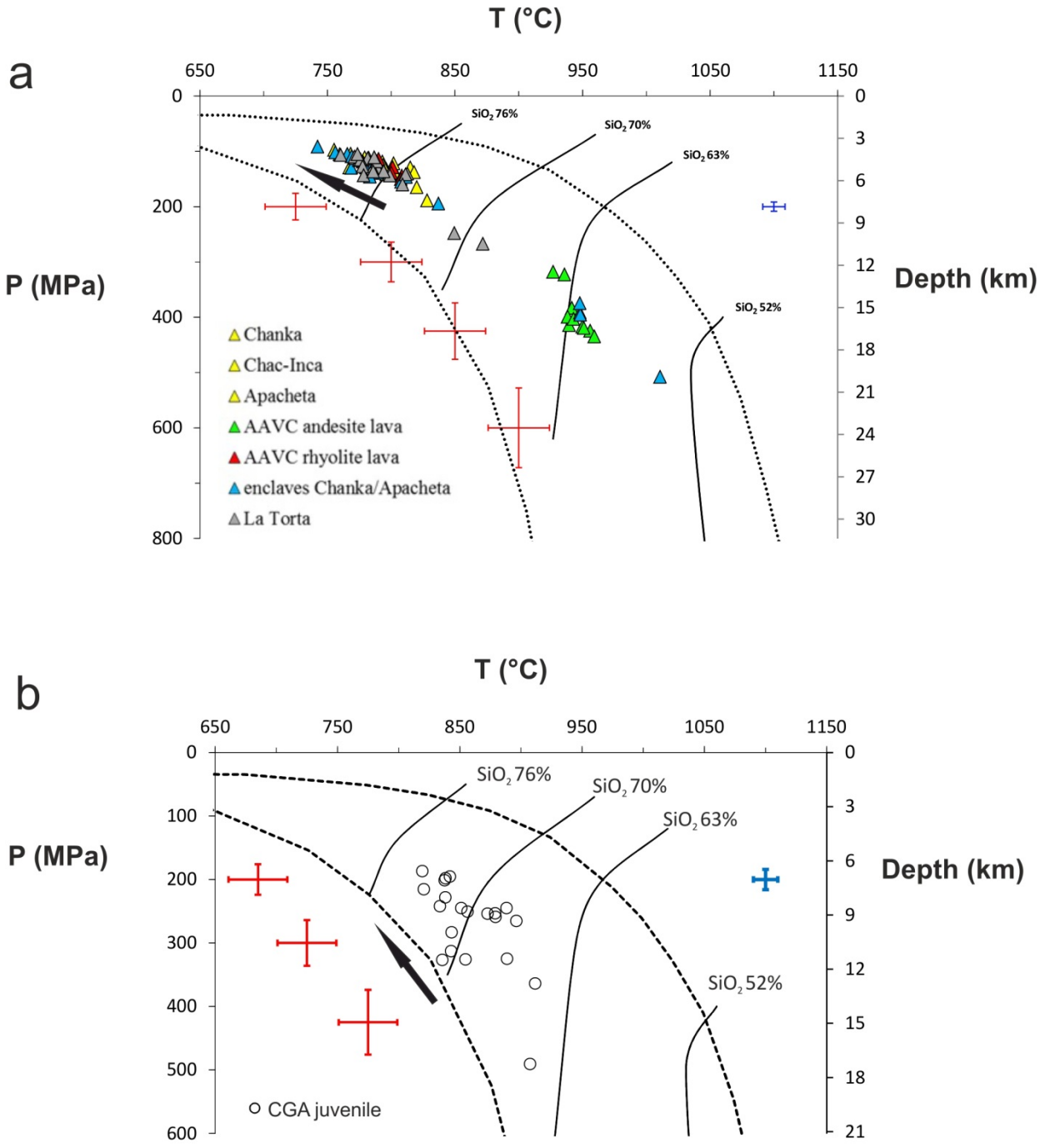

Fig. 4.7 a) and b) P-T-h diagrams for AGA, TGA and CGA amphiboles. The black dotted lines represent the stability field of Mg-rich amphibole. The solid black lines represent the SiO_2 content of melts in equilibrium with amphiboles used to derived the thermobarometric equations. Red bars indicate the P-T uncertainties of R&R2012 method. The blue bars indicate the average value of SD for the entire dataset of AGA, TGA and CGA anphiboles Black arrows show the general path of P-T variation from core to rim of zoned amphiboles.

are not aligned with the cross-section of Ward et al. (2014) (cross-section lies approximately 30 km NE from AGA domes) we correct this misalignment plotting our data also into the map slices at different depth of Ward et al. (2014) model (Fig. 4.8b, c, d), obtaining a more realistic qualitative contextualization of our crystallization depths [since that Ward et al. (2014) referred their seismic profile depth to sea level, we correct our amphiboles depth to sea level]. As we can see in Figure 4.7a and b, at depth of 5 km the data from AGA with low depth of crystallization fall within the 3.2 km/s velocity contour. Between the 10 and 15 km map slices (Fig 3.8c, d) the data from Apacheta dome with the highest depth of crystallization (andesite lava and

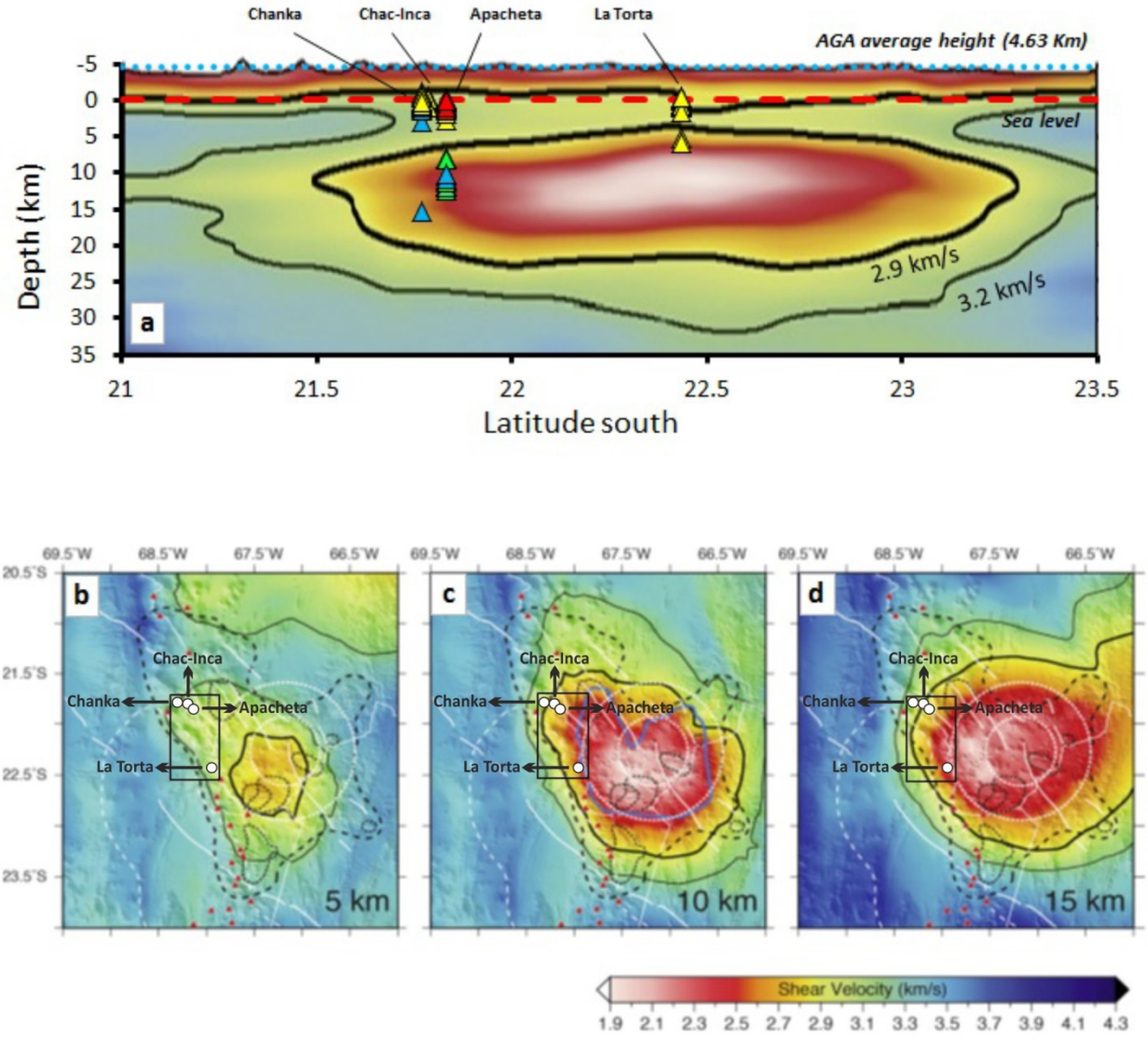

Fig. 4.8 a) Seismic tomography cross-section of APMB (Ward et al., 2014) with crystallization depth of amphiboles obtained with the R&R2012 method [(referred to sea level (red dotted line)]. b), c), d) map slices, at different depth, of APMB as constrained through joint ambient noise-receiver function inversion S-velocity model by Ward et al., (2014). The location of AGA and TGA domes is highlighted by the black boxes in b, c and d.

intermediate-basic enclaves) fall within the 2.9 km/s velocity contour and in proximity of the volume of rocks with velocity of 2.5 km/s (red coloured area in Fig 3.8a, c, d). Crystals from La Torta dome are located above the lowest velocity contour (1.9 km/s; white coloured area) and presumably at the border between 2.9 and 3.2 km/s velocity contour. In fact in the 5 km map slice La Torta dome is located between the 2.9 km/s and 3.2 km/s velocity contours while at depth of 10 km, corresponding to the deepest crystal of La Torta, the 2.9 km/s velocity contour enclose the crystals (Fig. 4.8 b, c). Data from Chanka dome always lies outside the 2.9 km/s contour (Fig. 4.8b, c, d).

Overall the crystallization depths of amphiboles are coherent with the APMB of Ward et al. (2014). Indeed the deepest values of Apacheta dome, represented by less differentiated products, are located within the lowest velocity contour which is linked to more elevated temperatures of rocks or to larger volume of silicate melts. Moreover with increasing age of the volcanic structures from south [La Torta dome, 34±7 Ka (Renzulli et al., 2006)] to north [Chanka dome, 1.5 Ma-years-old (Roobol et al., 1974)] also increases the distance from the central area of APMB where much more volume of melt is expected due to the low velocity (1.9 km/s) (Fig. 4.8b, c, d). The younger eruptive centre (i.e. La Torta dome) seems to be located where the inferred volume of magma is higher while the older eruptive centre (i.e. Chanka dome) is located at the border of APMB where higher velocity contour (3.2 km/s) probably indicates the presence of colder rocks or less volume of melt.

4.6 CONCLUSIONS

In the framework of the geothermal exploration, a fundamental aspect is to constrain the heat source of geothermal system. In this study we selected amphiboles from geothermal areas of Chachimbiro (northern Ecuador), Apacheta and La Torta (northern Chile). We applied the Ridolfi and Renzulli (2012) amphibole thermobarometer to retrieve the P-T conditions during amphibole crystallization trying to reconstruct the magma path during its ascent toward the surface. The studied amphiboles are frequently affected by chemical zoning, breakdown and fast-growing textures, indicating disequilibrium conditions suffered by crystals. Since that the R&R2012 thermobarometer requires homogeneous amphibole composition (i.e. equilibrium condition) to calculate reliable P and T values, we have compared the intra-crystal compositional variation with average standard deviation (σ) of element oxide of experimental amphibole used to retrieve the thermobarometric model to identify homogeneous micro-domains in the crystal with compositional variation in the range of σ. These micro-domains approximate the typical uncertainty of EMP analyses and can be considered crystallized at equilibrium condition. Thus, these compositions were used to retrieve P-T values with R&R2012. Element oxide variation outside the σ range can be ascribed to disequilibrium condition of amphibole crystallization and should be discarded together with fast-growing texture (non-steady state condition) to avoid large

errors in the calculation of intensive parameters (e.g. overestimation of pressure). This procedure allowed us to obtain reliable P-T value of magma storage and crystallization below the geothermal areas. The feeding systems of AGA and TGA are composed by shallow magma chambers with crystallization of evolved magma between depth of 4-7.5 km (T=755-828 °C) and 4-10 km (T=755-872 °C), respectively. They represent the primary source of heat for the hydrothermal reservoir. In the case of AGA, the shallow magma chamber is fed by basic to intermediate magmas from deeper crustal levels (about 15-19 km, T=948-1011 °C). We therefore suggest polybaric differentiation of magma in the upper crust (20 km) beneath an area of APVC from Chanka (north) to La Torta (south) domes. This petrological evidence is in agreement with the existence of a partially melted zone in the upper crust of the APVC, the so called Altiplano-Puna Magma Body (APMB) which was detected by geophysical data. Crystallization depths of amphibole obtained with the R&R2012 method is thus consistent with the seismic tomography model for the APMB recently carried out by Ward et al. (2014), pointing out a good accuracy and reliability of R&R2012 method.

Pre-eruptive conditions of amphiboles in the feeding system of CGA constrain the presence of shallow magma chamber at depth of about 6.5 km (T between 800-900°C) which represent the heating source of the geothermal system. Deeper magma sources are present up to depth of 19 km with temperature higher than 900°C. Also in this case the presence of normally zoned amphibole points out a polybaric differentiation of magma below the geothermal area.

5 Origin of geothermal fluids along active to semi-dormant volcanoes of Northern Ecuador (1°S to 1°N) as inferred from chemical and isotopic composition

5.1 INTRODUCTION

Late-Pliocene to present-day volcanism in Ecuador is characterized by large stratovolcanoes, caldera complexes and lava domes many of which active and potentially active (Hall et al., 2008). Volcanic edifices are distributed along three NNE-trending alignments and built up over basements of different age, thickness and composition in a complex geodynamic setting characterized by a flat-slab subduction (Gutscher et al., 1999, 2000) between the Nazca and the South American Plates (Fig. 5.1a). A widespread geothermal activity which could be exploited is present in northern Ecuador (ca. between 1°S and 1°N) closely associated to Quaternary volcanism. Despite this great geothermal potential, the exploitation of geothermal energy is still restricted to direct use of low and medium temperature fluids for bathing, balneology and swimming pool (Beate and Urquizo, 2015) although several high-enthalpy resources for electric-power generation have been identified (Almeida et al., 1992; Beate and Urquizo, 2015).

The first systematic characterization of thermal and cold waters from the whole Ecuador as well as dissolved and bubbling gases was performed by Inguaggiato et al (2010). On the basis of the chemical and isotopic features of the thermal discharges, strong gas–water interaction processes acting on the recharging meteoric water were recognized to occur within the fluid reservoirs. Isotopic tracers suggested the occurrence of significant mantle-related fluid contribution. Inguaggiato et al. (2010) also emphasized the different isotopic characteristics of fluids from the Ecuadorian Quaternary active volcanism (north of 2°S), with respect to those from the inactive arc (south of 2°S). However, they did not find differences between the hydrothermal systems through the frontal arc, the Inter-Andean Depression and the main volcanic arc despite their different basement terranes.

The present work provides a description of the geology and fluids geochemistry of geothermal areas located between the frontal and main arcs (including the Inter-Andean Depression) of Northern Ecuador (1°S to 1°N) and directly associated to the Late-Pliocene and the ongoing volcanic activity (Hall et al., 2008). The thermal fluids, with the exception of those from the Nangulvì and Cristobal Colon systems, are likely related to the following volcanoes (Fig. 5.1b; Table 5.1): i) Chiles-Cerro Negro Volcanic Complex, ii) Chachimbiro Volcanic Complex and Cuicocha caldera, iii) Chacana Caldera Complex and iv) Quilotoa volcano. Seven thermal water samples (from Chiles-Cerro Negro, Chachimbiro, Cristobal Colon and Nangulvi) and two bubbling gas samples

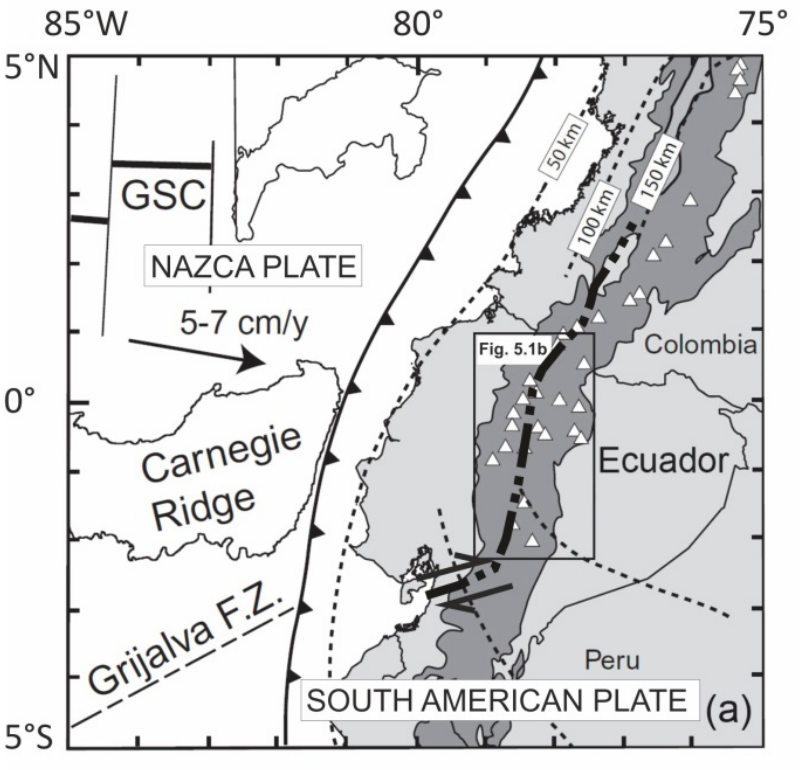

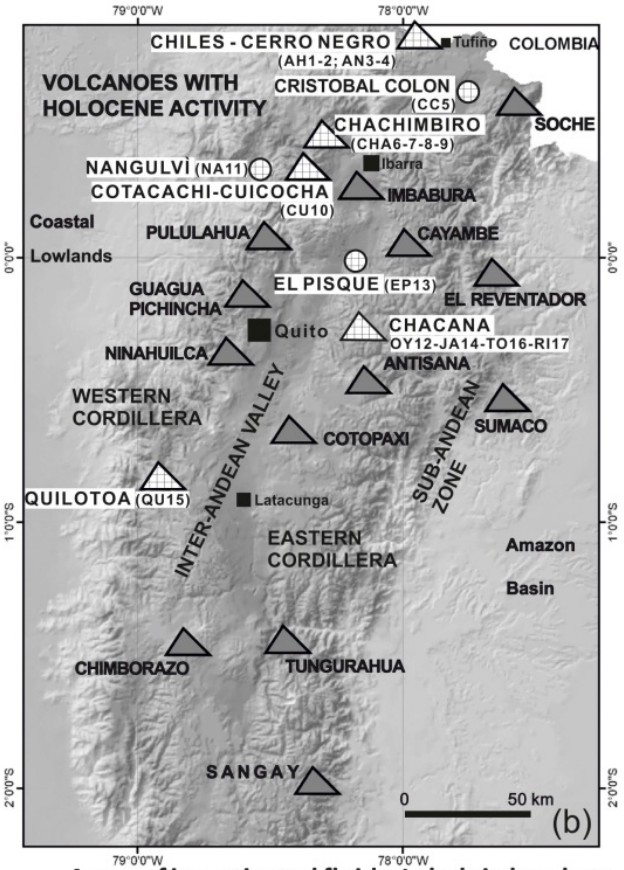

Areas of investigated fluids. Labels in brackets indicate the identification code of thermal water and/or bubbling gas samples.

Fig. 5.1a, b. (see caption ahead)

Fig. 5.1. a) Geodynamic setting of the Ecuadorian arc, including the Carnegie Ridge Plateau and other main oceanic features (Grijalva F.Z. = Grijalva Fault Zone; GSC = Galápagos Spreading Centre). The Andes are delineated by the 2000 m contour (dark grey) and the main Quaternary volcanoes by the small white triangles. Depth contours of the Wadati-Benioff Zone indicated as dotted line (modified from Bourdon et al., 2003). The thick solid-dotted line represents the regional boundary between the oceanic terranes domain to the west and continental terranes to the east (from Spiking et al., 2005) (approximate location). b) Distribution of Ecuadorian volcanoes with Holocene activity and subdivisions of the volcanic arc (modified from Hall and Mothes, 2008a).

Table 5.1 Summary table for sampling sites and related volcanic/geothermal areas.

Sample	Location	Type*	Latitude	Longitude	Elev. (masl)**	Volcanic structure/Geothermal Area		Volcano type	Spring location (physiographic unit)
AH 1	Aguas Hediondas	TS	0.8097380307	-77.90597403	3608	Chiles-Cerro Negro volcanic complex		Semi-active	Western Cordillera
AH 2	Aguas Hediondas	CS	0.8097620029	-77.90632498	3613				
AN 3	Aguas Negras	TS	0.8113890141	-77.90013000	3544				
AN 4	Aguas Negras	TP	0.8115999866	-77.89956900	3400				
CC 5	Cristobal Colon	TS	0.5965109635	-77.79112402	2827				Inter-Andean Valley
CHA 6	Chachimbiro (Aguas Savia)	TS	0.4645679891	-78.23405497	2507	Chachimbiro Volcanic Complex		Semi-dormant	Western Cordillera
CHA 7	Chachimbiro	TS	0.4571350012	-78.24117296	2567				
CHA 8	Chachimbiro (Cahuasquì)	TS	0.5072799884	-78.21886503	2262				
CHA 9	Chachimbiro (Timbuyaco)	TS	0.4266439844	-78.26884297	2735				
CU 10	Cuicocha	LW	0.3060780186	-78.36163902	3070	Cotacachi-Cuicocha Volcanic Complex		Semi-dormant	Western Cordillera
NA 11	Nangulvì	TS	0.3285329696	-78.54660298	1391				Western Cordillera
OY 12	Oyacachi	TS	-0.2157960366	-78.08822603	3011	Chacana Caldera	North-eastern rim	Active	Eastern Cordillera
EP 13	El Pisque	TS	0.0066659600	-78.17860298	2670		Distal outflow (~20 km N)		Inter-Andean Valley
JA 14	Jamanco	TS	-0.3755820170	-78.17849502	3322		Southern sector		Eastern Cordillera
TO 16	Calera de Tolontag	TS	-0.3448190074	-78.31507503	3432		Western outer slope		Inter-Andean Valley
RI 17	Vertiente Rio Lisco	TS	-0.4611190036	-78.31562103	3464		South-western outer slope		Eastern Cordillera
QU 15	Quilotoa	LW	-0.8621430304	-78.91108501	3459	Quilotoa Caldera		Semi-dormant	Western Cordillera

* TS= thermal spring; CS=cold spring; TP=thermal pool; LW=lake water

**masl=meters above sea level

(Chiles-Cerro Negro and Chachimbiro), represent new data with respect to Inguaggiato et al. (2010). We provide geochemical and isotopic data on thermal waters and gases to evaluate the relationship between active, semi-dormant or dormant Ecuadorian volcanoes and geothermal areas and the characteristics of hydrothermal resources in the framework of the high geothermal potential of northern Ecuador. We also point out the role played by the different geological and geodynamic settings of Ecuadorian arc-trench system on the characteristics of thermal fluids and gases.

5.2 GEODYNAMIC, GEOLOGICAL AND VOLCANOLOGICAL SETTINGS

The Quaternary Ecuadorian volcanic arcs results from the eastward subduction of the Miocene Nazca oceanic Plate (<25 Ma; Hey, 1977; Pennington, 1981; Lonsdale, 2005; Barckhausen et al., 2008; Müller et al., 2008; Seton et al., 2012) beneath the South American Plate (Fig. 5.1a) at a convergence rate of 5-7 cm/y at least north to 0° of latitude (DeMets et al., 1990; Kellogg and Vega, 1995; Norabuena et al., 1999). The subducting plate carries an aseismic volcanic plateau, namely the Carnegie Ridge (Fig. 5.1a), formed by the eastward motion of the Nazca Plate over the Galapagos hotspot (Hey, 1977; Lonsdale, 1978, Lonsdale and Klitgord, 1978). From west to the east, Ecuadorian

volcanoes are distributed along three NNE-trending alignments: Western Cordillera (frontal arc), the Inter-Andean Depression and Eastern Cordillera (main arc) and the Sub-Andean Zone (back-arc region). A tectonic boundary (Fig. 5.1a) separates the Late Cretaceous- Eocene-accreted oceanic terranes and associated volcano-sedimentary arc underlying the Western Cordillera (Lebrat et al., 1987; Daly, 1989; Bourgois et al., 1990; Reynaud et al., 1999; Spikings et al., 2001; Hughes and Pilatasig, 2002; Kerr et al., 2002; Vallejo et al., 2009) from the Paleozoic continental metamorphic and igneous rocks forming the basement of the Eastern Cordillera (Litherland et al., 1994; Pratt et al., 2005). The thickness of the crust is inferred to be 25-30 km (Feininger and Seguin, 1983) up to 40-50 km (Guillier et al., 2001) for the Western Cordillera and about 50 km (Feininger and Seguin, 1983) up to 75 km (Guillier et al., 2001) for the Eastern Cordillera.

The volcanic products consist of medium to high-K calc-alkaline basaltic andesites to rhyolites with predominance of andesites and dacites (Barragan et al., 1998; Monzier et al., 1999; Bourdon et al., 2003; Samaniego et al., 2005; Hidalgo et al., 2008; Robin et al., 2009; Chiaradia et al., 2011). In the Sub-Andean Zone smaller stratovolcanoes and scoria cones have erupted both medium-K calc-alkaline lavas (Ridolfi et al., 2008) and K-rich, silica undersaturated lavas with alkaline affinity (Barragan et al., 1998; Bourdon et al., 2003; Hoffer et al., 2008). It is worth to note that a flat-slab geometry, due to the Carnegie Ridge subduction, could have led to a lithospheric slab-tears (Gutscher et al., 1999, 2000) and the partial melting of the oceanic slab with the change of geochemical signature of volcanic products and transition from calc-alkaline to adakitic magmatism (Samaniego et al., 2002; Bourdon et al., 2003; Samaniego et al., 2005; Hidalgo et al., 2007; Robin et al., 2009).

5.2.1 Chiles-Cerro Negro Volcanic Complex

Chiles (0°49' N, 77°56' W) and Cerro Negro (0°46' N, 77°57' W) are two adjacent active stratovolcanoes with an elevation of 4,748 and 4,470 m a.s.l. respectively, located in the northern sector of Western Cordillera at the border between the province of Carchi, in Ecuador and the department of Nariño, in Colombia (Fig. 5.1b), about 7 km west of the villages of Tufiño (Ecuador) and Chiles (Colombia). The most significant morphological features are horseshoe-shaped collapsing structures affecting the northern slope of Chiles and the western slope of Cerro Negro with 1 km and 1.8 km across respectively, and landscape forms linked to glacial moraine deposits (Cortés y Calvache, 1996). The volcanic complex is built up on top of a thick sequence of Pliocenic andesitic lavas overlying volcano-sedimentary deposits of Nariño Formation and accreted oceanic crust of Early-Mid Cretaceous age (Pallatanga Terrain), with an associated island arc (Río Cala Formation) and trench sediments (Natividad Formation) of Mid-Late Cretaceous age (Beate and Urquizo, 2015). The tectonic framework is characterized by active NNE trending regional strike-slip faults (Cepeda et al., 1987) and

local NNE and NW trending fault systems cutting the volcanic complex (ICEL, 1983).

Lavas are mainly medium-K calc-alkaline two-pyroxenes and olivine-bearing andesites and dacites (Droux and Delaloye, 1996) with predominantly effusive products for Chiles, while Cerro Negro was characterized by a more explosive behaviour, since its products consist of pyroclastic flow deposits and debris avalanche (Cortés and Calvache, 1996). Petrographic and geochemical data suggest that fractional crystallization, magma mixing and crustal assimilation occurred in the genesis of the erupted magmas (Droux and Delaloye, 1996). The volcanic complex activity started in Pleistocene and the last eruption of Chiles is dated 160 ky while some lavas of Cerro Negro are probably Holocenic. An eruption reported in 1936 is questionable because may have been from El Reventador (Global Volcanism Program, 2013a) located about 100 km toward ESE. ^{14}C dating related to the most recent debris avalanche deposit of Cerro Negro provided an age of 6065±130 years BP (Cortés and Calvache, 1996). The current activity is represented by thermal discharges consisting of acidic hot (up to 55°C) springs occurring 2-3 km east of Volcan Chiles and bicarbonate springs close to the villages of Tufiño and Chiles (Beate and Urquizo, 2015). The development of tourist thermal spring area of Aguas Hediondas has repeatedly failed because of the detected high (deadly) levels of H_2S emissions (Global Volcanism Program, 2013a). Other hot water discharges located near the collapse structures of both volcanoes were also reported (Cortés and Calvache, 1996). Since April 2013, as reported by Ruiz (2015) on the basis of data from the Observatorio Vulcanológico and Sismológico de Pasto (SGC-OVSP), a division of the Servicio Geologico Colombiano and the Instituto Geofísico de la Escuela Politécnica Nacional (IGEPN), three seismic swarms have been detected. Most earthquakes had magnitude between 1.0 to 4.0 and are located about 1-4 km south of Chiles volcano with shallow depth (up to 14 km). A major 4 km-depth event occurred on October 2014 with a local magnitude of 5.7. Anyway no evidence of surface volcanic activity linked to the above recent seismic swarms has been documented or reported.

5.2.2 Chachimbiro Volcanic Complex and Cuicocha caldera

The Chachimbiro Volcanic Complex (0°28' N, 78°18' W, max altitude 4054 m a.s.l.) is located in the northern part of the Western Cordillera on the border of the Inter-Andean Valley, about 70 km NNE of Quito and 17 km NE of Ibarra city (Fig. 5.1b). The whole complex is underlain by Cretaceous oceanic plateau basalt of the Pallatanga Terrain and associated with the Late Cretaceous volcano-sedimentary and volcanic deposits of Rio Cala Group (Rio Cala and Natividad Formations; Boland et al., 2000; Vallejo, 2007; Vallejo et al., 2009), overlain by Late Maastrichtian-Early Paleocene continental sediments and volcanic products of the Silante Formation (Vallejo et al., 2007, Vallejo et al., 2009) and finally by Miocene-Pliocene volcanoclastic deposits (Boland et al., 2000). Two main NE-SW and WNW-ESE striking tectonic trends are present (Aguilera et al., 2005). According

to Bernard et al. (2011), the area of Chachimbiro is characterized by persistent volcanic activity started with the eruption of calc-alkaline andesites of the Mid-Pleistocene Huanguillaro Volcano, which subsequently suffered a gravity-driven collapse involving some explosive events (Aguilera et al., 1998). The volcanic activity continued with the building up of caldera-filling rhyodacitic Tumbatu and Hugà domes with related pyroclastic deposits and the Late-Pleistocene Chachimbiro-Pucarà NNE line of andesitic-dacitic domes (Beate and Salgado, 2010).

The most recent volcanic products consist of pyroclastic flow deposits from one of these domes with an age younger than ca. 8000 years BP (Aguilera, 1998; Beate, 2001; Comida, 2012; Bernard et al., 2014). Near-neutral chloride to bicarbonate hot springs, with temperatures ranging from 40 to 55°C, were recognized to the east of the system (Beate and Salgado, 2010). Other volcanoes are located W and WNW of Chachimbiro such as Yanaurcu de Piñán (andesite to dacite), Pulumbura (andesite) and Pilavo (basaltic andesite) (Bernard et al., 2011).

The Cuicocha lake-filled caldera (0°18' N, 78°21' W) is located in the Western Cordillera, about 20 km SSW of Chachimbiro Volcanic Complex, at the southern foot of the inactive Pleistocene Cotacachi volcano that stands along the Otavalo-Umpala fracture zone (Hanuš, 1987). The caldera-forming eruption is dated at 3 ky BP (Hall and Mothes, 1988). Cuicocha volcano can be considered semi-dormant as the last post-caldera activity is represented by four intracaldera lava domes (Gunkel et al., 2009) dated between 1350 and 1230 years BP. The caldera has a diameter of 3.2 km with steep side flank (>45°) and host a 148 m-deep sodium-bicarbonate lake with a surface altitude of 3072 m a.s.l., formed after the dome-building phase and feed by the catchment area of Cotacachi volcano, rainwater and hydrotermal water inflow (Gunkel et al., 2009). Post-magmatic activity consists of regular gas emissions in the western part of the lake and in the channel between the two domes. The gas, mainly CO_2 and N_2, is of volcanic origin, due to the occurrence of CO and the accumulation of boron in the lake (Gunkel et al., 2008).

5.2.3 Chacana Caldera Complex

The active Chacana Caldera Complex (0°19'S, 78°10' W) is located at about 40 km ESE of Quito in the Eastern Cordillera (Fig. 5.1b). It represents the largest rhyolitic center of Ecuador with a length of 35 km in N-S direction and a width of 10-15 km through E-W, with a maximum altitude of about 4500 m a.s.l. (Beate et al., 2009). The basement consists of Paleozoic-Mesozoic metamorphic rocks in the middle part and eastern side, Mesozoic oceanic basalts in the western side and thick Miocene-Pliocene sequence of andesite flow, breccias and tuffs of the Pisayambo Formation (Beate et al., 2010). Ongoing tectonic activity includes NE-trending transpressive faults and eastward-trending thrust faults (Hall and Mothes, 2008b). Prior to the caldera-forming eruptions, a Pliocene andesite volcanic field 60 km long (N-S direction) and 28 km wide (E-W) was present (Beate et al., 2010). According to Hall and Mothes (2008b), the

Chacana Caldera Complex began its activity at about 2.7 My BP, with evidence of fault-related breccias ring dike injections along the caldera fractures. A subsequent event consisted of deposition of a *ca.*1250 m thick sequence of dacitic to rhyolitic ignimbrites and tuffs that covered the western outer flank of the structure, followed by the main caldera collapse occurred about 0.8 My BP. The depression was partly filled by thick sequences of tuffs, breccias, andesitic lavas and a succession of fluvial sediments. Post-collapse resurgence began after 0.44 My with a long period of andesite to dacite lavas erupted by a series of vents aligned NNE in the western sectors of the caldera. Volcanic activity continued until about 0.16 My BP, including ignimbrites, pumice fall deposit and obsidian flow. More recent andesite to dacite lava flow occurred from 30 to 20 ky BP, whereas the youngest lava flow occurred in the 1700's. Alkaline chloride hot (up to 65°C) springs were recognized along the NE-trending fault in the southern-central sectors of the caldera (Beate et al., 2010), as well as on the SSW and W outer flank and on the NE (Oyacachi) inner caldera rim.

5.2.4 Quilotoa volcano

Quilotoa volcano (0°51' S, 78°54' W) is located in the Western Cordillera, approximately 35 km WNW of the city of Latacunga (Fig. 5.1b). The volcanic edifice, with a maximum elevation of 3915 m.a.s.l., is truncated by a subcircular caldera containing a lake with a diameter of about 2 km, a maximum depth of 256 m and an estimated total volume of about 0.35 km^3 (Aguilera et al., 2000). According to Hall and Mothes (2008c), the regional basement consists of folded Tertiary sediments overlying Cretaceous oceanic basalts and sediments. The volcanic edifice was produced by three Late-Pleistocene to Holocene caldera-forming eruptions and its present morphology consists of ca 3 km-wide caldera with interior steep-sided walls rising about 400 m above the lake. A series of dacitic domes aligned along and inside the highly irregular caldera rim were recognized. The outer flanks of the volcanic edifice have a more gently slope to the north and south compared to the eastern side that abruptly slope downward toward the Toachi canyon.

Hall and Mothes (2008c) recognized at least eight major Quaternary eruptive cycles, each one separated by a long (10-15,000 years) dormant interval. The last eruption occurred about 800 years BP. The volcanic activity was characterized by large plinian eruptions (VEI=4-6) whose deposits mainly consists of phreatomagmatic ash fall units followed by pumice lapilli falls and repeated series of surge and ash flows. The final stage of eruptive cycles was occasionally marked by dome extrusions. The tephra products and dome rocks are medium-K calc-alkaline dacites with a mineral assemblage constituted by plagioclase, amphibole, biotite, quartz, Fe-Ti oxides and apatite as accessory phases. The similarities between volcanic products, eruptive styles and stratigraphic sequences throughout the cyclic eruptions, might be the results of the same petrogenetic processes involving homogeneous magma bodies at shallow depth (Hall and Mothes, 2008c). Bubbling

gases currently occur in the southwestern sector of the shoreline along the NNE-trending fault crossing the lake and the caldera walls (Aguilera et al., 2000).

5.3 SAMPLING AND ANALYTICAL METHODS

Water samples are reported in Table 5.2. Four water samples (AH1-2; AN3-4) and two gas samples (AH1 and AN3) were collected from the Chiles-Cerro Negro Volcanic area, whereas the CHA6-9 waters and the CHA6, CHA 7, and CHA9 gases were collected from Chachimbiro volcanic complex. One gas sample (CU10) was collected from the Cuicocha caldera lake. Five water (OY12, EP13, JA14, TO16 and RI17) and five gas (OY12, EP13, JA14, TO16 and RI17) samples were collected within and close to the Chacana caldera. Water and gas samples (QU15) were collected at Quilotoa caldera lake. NA11 and CC5 water samples were collected from Nangulvì and at ~16 km NNW (Cristobal Colon) of the Chalpátan caldera, respectively.

Water temperature and pH were measured in the field using portable instruments. Two water aliquots were collected for the determination of anions and cations. One of them was acidified by adding Suprapur hydrochloric acid (1% HCl). Both aliquots were filtered at 0.45 µm in the field. An unfiltered water aliquot (125 mL) was sampled for the analysis of the oxygen and hydrogen isotopes in H_2O. For the analysis of reduced sulfur species (hereafter ΣS^{II-}), 8 mL of water were transferred in the field to a tube containing 2 mL of an ammonia–cadmium solution to favor CdS precipitation (Montegrossi et al., 2001). Total alkalinity was measured by titration using HCl 0.01N as titrating agent and methyl-orange as colorimetric indicator. Water samples were analyzed by ion chromatography (Cl^-, SO_4^{2-}, NO_3^-, Br^-, and F^-), molecular spectrophotometry (NH_4^+), atomic absorption spectroscopy (Li^+, Na^+, K^+, Ca^{2+} and Mg^{2+}) and inductively coupled plasma-optical emission spectroscopy (H_3BO_3 and SiO_2). Analytical errors were <3% and <5% for the main and minor components, respectively. The ΣS^{II-} concentrations were determined after centrifugation to separate the CdS precipitate from the liquid phase. Then, CdS was oxidized by adding 5 mL of H_2O_2 and analyzed as SO_4^{2-} by ion chromatography. The isotopic composition of oxygen and hydrogen in H_2O values were determined by mass spectrometry (Vaselli et al., 2006 and references therein). The analytical errors were ±0.05 and ±1, respectively.

Gas samples (Table 5.3) were collected from bubbling waters by using a plastic funnel positioned above the bubbles and connected with a glass thorion-tapped flask. At each sampling point two different gas aliquots were collected, as follows: i) a pre-evacuated 150 mL glass flask for the determination of the of the $^{13}C/^{12}C$ ratios of CO_2 ($\delta^{13}C\text{-}CO_2$) and $^3He/^4He$ values; ii) a pre-evacuated 60 mL glass flask filled with 20 mL of a 5N NaOH and 0.15 M $Cd(OH)_2$ suspension for the determination of the chemical composition. Inorganic gases (N_2, $Ar+O_2$, H_2, He and CO) and CH_4 stored in the soda flask headspace were analyzed by using a Shimadzu 15A gas

chromatographic system equipped with a 9 m long molecular sieve column and thermal conductivity detector (TCD). Argon and O_2 were analyzed using a Thermo Focus gas chromatograph equipped with a 30 m long capillary molecular sieve column and a TCD. Light hydrocarbons were determined by a Shimadzu 14A gas-chromatograph equipped with a 10 m long stainless steel column (φ = 2mm) packed with Chromosorb PAW 80/100 mesh (coated with 23% SP1700) and FID detector. Hydrogen sulfide concentrations were determined by analyzing SO_4^{2-} in the soda solution by ion-chromatography as after oxidation with H_2O_2. Carbon dioxide, dissolved in the soda solution as CO_3^{2-}, was analyzed by acidimetric titration with 0.1N HCl. The analytical errors were ±5% for the main gas components and ±10% for minor and trace gas compounds.

The $\delta^{13}C$-CO_2 values (expressed as ‰ vs. V-PDB) were analyzed by mass spectrometry (Finningan Delta S), after a two-step extraction and purification procedure of the gas mixtures by using liquid N2 and a solid–liquid mixture of liquid N_2 and trichloroethylene. Internal (Carrara and San Vincenzo marbles) and international (NBS18 and NBS19) standards were used to estimate external precision. The analytical uncertainty and the reproducibility were ±0.05‰ and ±0.1‰, respectively.

The $^3He/^4He$ ratios (expressed as R/Ra, where R is the $^3He/^4He$ measured ratio and Ra is the $^3He/^4He$ ratio in the air: 1.39×10^{-6}; Mamyrin and Tolstikhin, 1984) were determined by using a double collector mass spectrometer (VG 5400-TFT) according to method described by Inguaggiato and Rizzo (2004). The analytical uncertainty was ±1%.

5.4 RESULTS

5.4.1 Chemical composition of thermal waters

Outlet temperature, pH value and chemical composition of water samples are shown in Table 5.2. The outlet temperatures range from 8.6 to 70.2 °C which correspond to Jamanco (JA14, Chacana) and cold spring discharge at Chiles-Cerro Negro (AH2), respectively. The highest temperatures measured at Chiles-Cerro Negro and Chachimbiro are 54.7 °C and 58.8 °C, respectively. Finally, Cristobal Colon with T=36.6 °C, Nangulvì T=50 °C, and Quilotoa T=14 °C. TDS (Total Dissolved Solids) show a wide range of values ranging from those typical of groundwater up to 11.58 g/L (Quilotoa). Chachimbiro and Chacana have TDS values in the same range (0.89-5.20 and 1.44-5.47 g/L, respectively) while lower values were measured at Chiles-Cerro Negro (0.03-1.34 g/L), Cristobal Colon (2.05 g/L) and Nangulvì (2.85 g/L). Except for the water samples from Nangulvì and Quilotoa , which show near-neutral pH values, those from Chachimbiro, Chacana and Cristobal Colon are slightly acidic (6.02-6.29, 5.98-6.5 and 6.14, respectively), whereas those from Chiles-Cerro Negro show the lowest pH values (from 4.52 to 5.77).

As shown in the LL classification diagram (Langelier-Ludwig, 1942; Fig. 5.2), the compositions of waters from the

Table 5.2. Outlet temperatures, pH, chemical composition, $\delta^{18}OH_2O$ and δDH_2O (‰V-SMOW) of thermal and cold water discharges from Chiles-Cerro Negro, Cristobal Colon, Chachimbiro, Nangulvì, Chachana and Quilotoa.

Geoth. Volc. Areas	Chiles-Cerro Negro					Chachimbiro					Chacana					Quilotoa
ID	AH1	AH2	AN3	AN4	CC5	CHA6	CHA7	CHA8	CHA9	NA11	OY12	EP13	JA14	TO16	RI17	QU15
Type*	TS	CS	TS	TP	TS	TS	TS	TS	TS	TS	TS	TS	TS	TS	TS	LW
Sampling location	Aguas Hediondas	Aguas Hediondas	Aguas Negras	Aguas Negras	Cristobal Colon	Aguas Savia	Chachimbiro	Cahuasquì	Timbuyaco	Nangulvì	Oyacachi	El Pisque	Jamanco	Calera de Tolontag	Vertiente Rio Lisco	Quilotoa
Date of sampling	15/01/2015	15/01/2015	15-16/01/2015	16/01/2015	16/01/2015	17/01/2015	17/01/2015	18/01/2015	18-19/01/2015	19/01/2015	20/01/2015	20/01/2015	21/01/2015	23/01/2015	23/01/2014	22/01/2015
T°C	54.7	8.6	35.7	19	36.6	32.5	58.8	26.8	43.3	50	46.2	38.2	70.2	39	31.2	14
Eh	-236	130	-380	-2.2	-85	-56	-70	92	-100	-114	-132	-41	-126	-160	-49	13
pH	4.52	5.39	5.77	5.15	6.14	6.09	6.02	6.15	6.29	7.01	6.5	6.29	6.03	6.18	5.98	7.25
Ca^{2+}	86.4	2.8	104.9	102.3	150.0	146.1	89.2	31.6	237.3	247.1	128.8	33.8	256.1	294.2	61.1	432.4
Mg^{2+}	53.0	1.8	78.1	76.9	151.5	90.4	54.6	29.2	146.1	4.5	61.5	91.0	9.2	66.2	72.3	785.2
Na^{+}	195.9	2.2	142.0	137.0	131.4	1565.2	1113.9	198.3	620.1	729.8	984.1	373.7	1246.1	1224.5	244.9	2222.5
K^{+}	45.1	1.0	33.5	34.1	39.0	61.9	145.7	17.5	66.1	10.1	38.9	47.5	57.9	79.1	29.4	210.3
Cl^{-}	109.5	0.1	116.3	110.5	88.9	2006.9	1824.7	181.0	853.0	1122.6	691.1	200.1	2039.6	566.6	248.4	4074.7
SO_4^{2-}	668.4	10.0	538.5	771.8	2.1	8.0	56.8	11.0	11.9	653.1	103.7	14.4	318.0	1455.4	15.1	2493.9
HCO_3^{-}	13.7	15.7	326.9	0.0	1482.2	1322.6	682.1	423.8	1710.1	83.6	2106.9	1226.3	479.3	1785.1	772.8	1362.5
TDS g/L	1.17	0.03	1.34	1.23	2.05	5.20	3.97	0.89	3.64	2.85	4.12	1.99	4.41	5.47	1.44	11.58
Li^{+}	0.26	bdl	0.16	0.13	0.13	3.81	4.80	0.54	2.12	1.41	2.75	0.33	2.66	2.42	0.18	3.42
F^{-}	2.98	0.03	0.41	0.66	0.55	0.35	0.35	0.56	0.28	1.88	0.64	0.84	2.46	2.99	0.95	0.49
Br^{-}	0.29	bdl	0.23	0.27	0.40	2.58	2.56	0.24	1.14	2.13	1.74	0.55	4.99	1.32	0.61	12.65
SiO_2	98.2	nd	138.4	nd	117.6	99.5	173.5	nd	141.8	46.0	129.2	118.3	83.6	68.4	133.7	83.4
H_3BO_3	32.0	nd	22.9	nd	56.0	288.2	236.7	nd	139.5	82.9	106.4	13.2	104.1	124.1	34.3	815.4
HS^{-}	26.5	bdl	40.5	nd	nd	nd	1.2	nd	0.5	11.6	0.1	nd	10.7	nd	nd	nd
NH_4^{+}	1.40	bdl	0.65	0.02	bdl	bdl	bdl	bdl	0.32	0.12	0.15	bdl	0.25	2.70	0.08	0.03
NO_3^{-}	bdl	bdl	bdl	0.02	0.07	0.07	0.14	0.10	0.12	0.10	0.14	0.10	0.14	0.26	0.93	6.59
$dD\text{-}H_2O$ ‰ (vs. V-SMOW)	-88.08	-81.30	nd	nd	-80.69	-64.28	-70.61	-78.51	-72.82	-52.80	-84.36	-95.32	-83.85	-90.93	-96.86	-37.91
$d^{18}O\text{-}H_2O$ ‰ (vs. V-	-11.76	-11.52	nd	nd	-11.45	-6.77	-7.78	-10.88	-9.40	-7.94	-10.77	-13.23	-11.73	-11.12	-13.14	-2.32

concentration expressed as mg/L; bdl: below detection limit; nd: not detected

* TS= thermal spring; CS=cold spring; TP=thermal pool; LW=lake water

Table 5.3. Chemical composition, $\delta^{13}C_{CO_2}$ (‰V-PDB) and R/Ra of free gases emitted from the thermal discharges of Chiles-Cerro Negro, Chachimbiro, Cuicocha, Chacana and Quilotoa

Geoth. Volc. Areas	Chiles-Cerro Negro		Chachimbiro			Cotacachi-Cuicocha	Chacana					Quilotoa
ID	AH 1	AN 3	CHA 6	CHA 7	CHA 9	CU10	OY 12	EP 13	JA 14	TO 16	RI 17	QU 15
Sampling location	Aguas Hediondas	Aguas Negras	Aguas Savia	Chachimbiro	Timbuyaco	Cuicocha	Oyacachi	El Pisque	Jamanco	Calera de Tolontag	Vertiente Rio Lisco	Quilotoa
CO_2	964	961	991	824	993	514	291	625	840	992	341	983
H_2S	13	11	bdl	bdl	bdl	bdl	bdl	bdl	bdl	bdl	bdl	bdl
N_2	21	26	7.1	168	5.6	456	661	351	146	6.3	623	16
Ar	0.48	0.62	0.17	3.9	0.13	6.5	15.5	7.6	3.2	0.15	14.5	0.36
O_2	0.72	0.66	1.6	3.9	0.96	21.8	32.3	15.2	9.6	1.1	21.8	0.71
H_2	0.075	0.061	0.006	bdl	0.003	bdl	0.004	0.006	0.004	0.005	bdl	0.081
CO	0.031	0.036	bdl	bdl	bdl	bdl	bdl	bdl	bdl	bdl	bdl	0.044
Ne	0.00026	0.00031	0.00012	0.0022	0.00009	0.0061	0.011	0.0041	0.0019	0.00011	0.011	0.00026
He	0.00013	0.00015	0.00011	0.0009	0.00011	0.0021	0.009	0.056	0.061	0.00015	0.0039	0.0015
CH_4	0.036	0.041	0.55	1.3	0.11	0.75	0.051	0.181	0.56	0.15	0.011	0.035
C_2H_6	0.00021	0.00015	0.0012	0.0068	0.0011	0.00092	0.0002	0.0019	0.0009	0.0016	bdl	0.0026
C_3H_8	0.00006	0.00007	0.00041	0.00087	0.00051	0.00011	bdl	0.00054	0.00012	0.00085	bdl	0.00013
C_6H_6	0.00011	0.00009	bdl	0.00007	bdl	bdl	bdl	bdl	bdl	bdl	bdl	0.00005
$d^{13}C\text{-}CO_2$ (V-PDB)	-5.28	-6.22	-6.89	-4.89	-5.24	-7.98	-8.05	-10.42	-7.14	-5.92	-10.56	-4.92
R/Ra	2.40	4.60	1.46	nd	nd	4.43	4.57	4.17	nd	nd	5.56	3.97
Rc/Ra	3.13	5.88	1.50	nd	nd	4.60	4.68	4.19	nd	nd	5.58	5.04

concentration expressed as mmol/mol; bdl: below detection limit; nd: not detected

Chachimbiro and Chachana areas ranged from Na-Cl to Na-HCO_3. Thermal waters from Chiles-Cerro Negro have a Na(Ca)-SO_4 composition. Lake Quilotoa had a Na-Cl(SO_4) composition, similar to what observed in November 1993 by Aguilera et al. (2000). Waters from Nangulvì and Cristobal Colon are classified as Na-Cl and Ca-HCO_3, respectively.

Silica content ranges between 46 and 173.5 mg/L, the highest value being recorded in the Chachimbiro area.

5.4.2 Chemical composition of gases

The chemical compositions of inorganic and organic (C2-C6 hydrocarbons) fractions in the free gases are reported in Table 5.3. The gas discharges of the investigated areas consisted of bubbling pools, hence it is not surprising that acidic and high-soluble gases (i.e. SO_2, HF, HCl) were not detected. Except for gas samples from Vertiente Rio Lisco and Oyacachi (Chacana), where N_2 is the dominant gas (623 and 661 mmol/mol, respectively) followed by CO_2 (341 and 291 mmol/mol, respectively), the gas chemical composition is dominated by CO_2 (from 514 to 993 mmol/mol) followed by N_2 (from 5.6

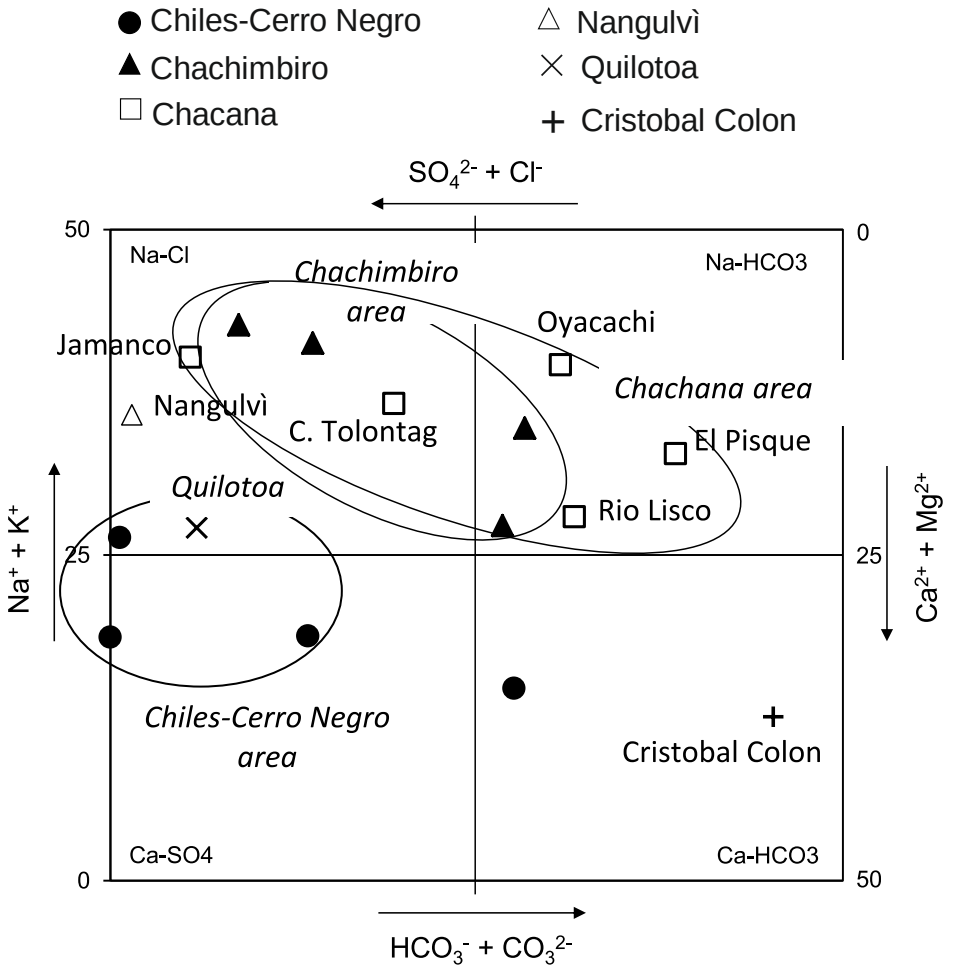

Fig. 5.2. Chemical classification of cold and thermal waters from the investigated areas (square classification diagram; after Langelier and Ludwig, 1942.

to 456 mmol/mol), O_2 (from 0.66 to 32.3 mmol/mol), Ar (from 0.13 to 15.5 mmol/mol). The highest values of O_2 (21.8 and 32.3 mmol/mol) and Ar (14.5 and 15.5 mmol/mol) were detected in Vertiente Rio Lisco and Oyacachi (Chacana). Detectable concentrations of H_2S were found only at Chiles-Cerro Negro (11 and 13 mmol/mol). CO shows appreciable values at Chiles-Cerro Negro (0.031 and 0.036 mmol/mol) and Quilotoa (0.044 mmol/mol). H_2 is <0.081 at Chiles-Cerro Negro and Quilotoa and <0.006 mmol/mol at Chachimbiro and Chacana.

He concentration and Ne concentrations are <0.0009 and <0.0022 mmol/mol, respectively, at Chiles-Cerro Negro and Chachimbiro. Volcanic lakes Quilotoa and Cuicocha show similar values of He (0.0015 and 0.0021 mmol/mol, respectively) and different values in Ne concentrations (0.00026 and 0.0061 mmol/mol, respectively). At Chacana He and Ne are <0.061 mmol/mol and <0.011 mmol/mol respectively.

The highest concentration of CH_4 was measured at Chachimbiro (1.3 mmol/mol).

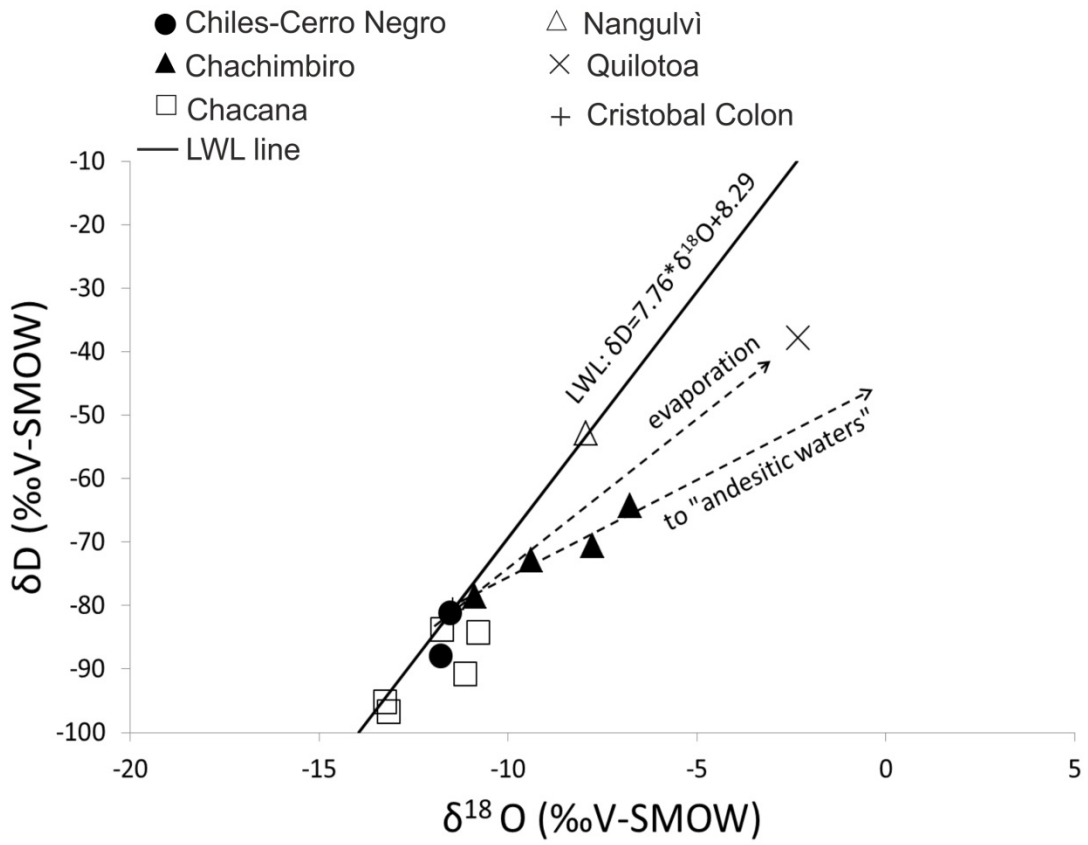

Fig. 5.3. δD versus $\delta^{18}O$. The isotopic compositions of sampled springs highlight a meteoric origin for all the samples. Significative isotopic shift are reported for Quilotoa and Chachimbiro samples and, to a lesser extent, for Chacana e Ciles-Cerro Negro. Local meteoric water-lines have been reported.

Chacana and Chiles-Cerro Negro show methane concentrations one or two orders of magnitude lower than Chachimbiro (<0.181 and <0.041 mmol/mol, respectively). CH_4 at Cuicocha is 0.75 mmol/mol.

$\sum C_2$-C_6 shows low values ranging from <0.00038 mmol/mol at Chiles-Cerro Negro to <0.00278 at Quilotoa, Chachimbiro, Chacana and Cuicocha.

5.4.3 Isotopic composition of waters (δD, $\delta^{18}O$) and gases ($\delta^{13}C_{CO_2}$ and R/Ra)

The isotopic compositions of thermal waters are reported in Table 5.2.

δD and $\delta^{18}O$ ranges from -96.9 to -37.9 ‰ and -13.23 to -2.3 ‰ versus V-SMOW, respectively. Data and local meteoric water-line (LWL) are reported on δD vs $\delta^{18}O$ diagram (Fig. 5.3). Samples from Nangulvì, Chiles-Cerro Negro and Cristobal Colon plot close to the LWL. A moderate isotopic shift of oxygen is observed for Chacana suggesting the occurrence of enhanced water-rock interactions. Much greater deviations from the LWL are recorded for Quilotoa and, to a lesser extent, for Chachimbiro water samples, suggesting evaporation and input of arc-type magmatic waters (Giggenbach, 1992).

The isotopic compositions of gases are reported in Table 5.3.

The $\delta^{13}C_{CO_2}$ values range from -5.3 to -6.2 V-PDB ‰ at Chiles-Cerro Negro, from -4.9 to -6.9 V-PDB ‰ at Chachimbiro, from -5.9 to -10.6 V-PDB ‰ at Chacana. Volcanic lakes Quilotoa and Cuicocha show values -4.92 and -7.98 V-PDB ‰, respectively.

R/Ra values, corrected for air contamination, indicate a significant contribution of mantle at Chacana (5.58) and, to a lesser extent, at Cuicocha (4.60) and Quilotoa (5.04), whereas Chachimbiro shows the lowest value (1.50).

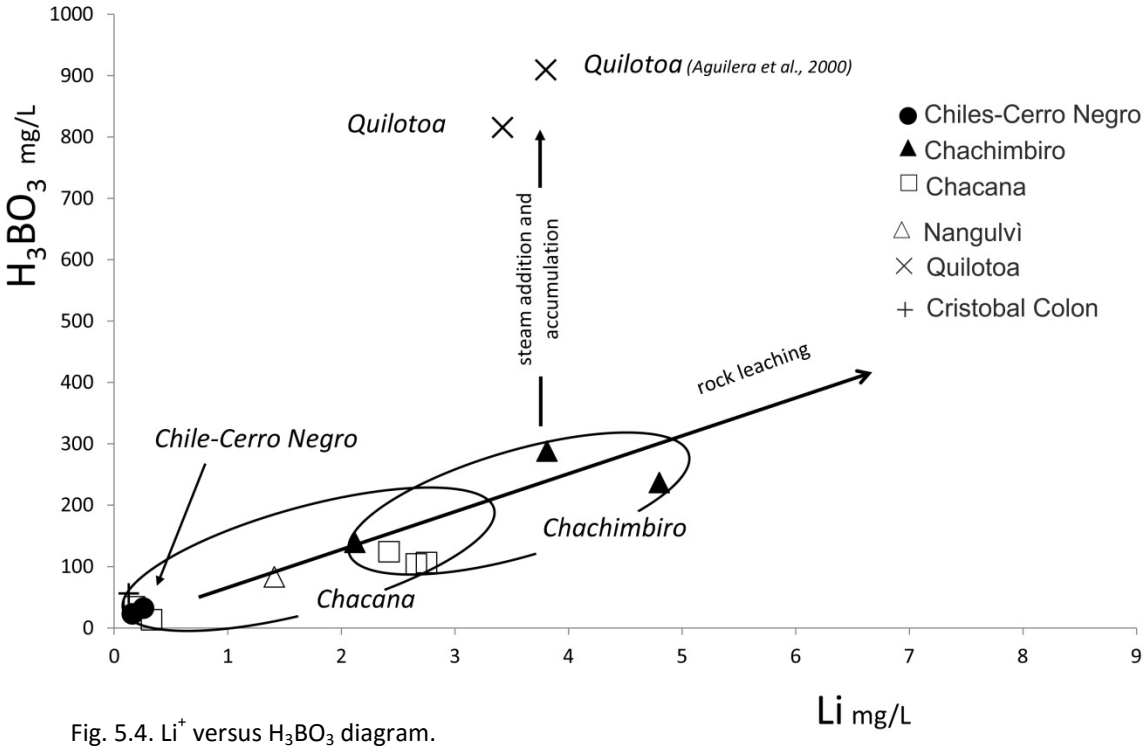

Fig. 5.4. Li^+ versus H_3BO_3 diagram.

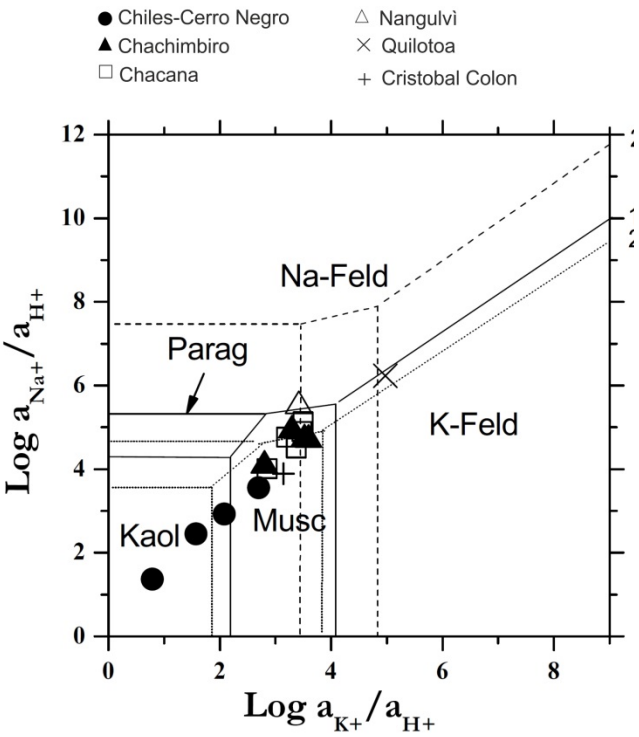

Fig. 5.5. log a_{Na+}/ a_{H+} versus log a_{K+}/ a_{H+}

5.5 DISCUSSION

5.5.1 Thermal water discharges

Waters from Chiles-Cerro Negro with temperature up to 55 °C, have a Na(Ca)-SO_4 composition, low pH values (<5.77) and low TDS values (<1.34 g/L) possibly identifying relatively shallow, steam-heated acid-sulphate waters. High temperature slightly acidic waters from Chachimbiro (T up to 60 °C; pH=6.02-6.29) and Chacana (T up to 70 °C; pH=5.98-6.5) with higher TDS values (from 0.89 to 5.20 g/L, from 1.44 to 5.47 g/L, respectively) compared to Chiles-Cerro Negro, are consistent with a direct emergence of partially or fully equilibrated thermal waters from the main geothermal reservoir.

Concerning minor components, Fig. 5.4 reports the Li^+ vs H_3BO_3 distribution. Li^+ only derives from leaching of the hosting rocks, whereas H_3BO_3 can be also added by addition of a vapor phase. Samples are mainly plotted with moderate shift respect to the rock leaching line. Samples of Chachimbiro and Chachana areas define a positive correlation between Li^+ and H_3BO_3, pointing out processes of rock leaching. Conversely, samples from Quilotoa caldera (data from this work and literature, Aguilera et al., 2000) only display very high contents of H_3BO_3, thus possible revealing the addition and accumulation within the active caldera lake of a boron-bearing vapor phase. Waters from Chiles-Cerro Negro and Cristobal Colon show low contribution of both elements.

The different interaction between waters and rocks is also shown in Fig. 5.5 where thermal waters display a different approach to equilibrium with alkali-feldspar in the hosting rocks. Samples from Chiles-Cerro Negro are far from any possible equilibrium, thus further supporting the idea of shallow, steam-heated waters. Conversely samples collected at Chachimbiro and Chacana areas plot closer to equilibrium conditions apparently at temperature in the range 150-200 °C, confirming the processes of rock leaching highlighted in Li^+ vs H_3BO_3 diagram (Fig. 5.4).

The isotopic composition of waters reveals a meteoric origin for all investigated areas. Anyway significant isotopic shift for Quilotoa suggests a process of evaporation probably related to steam accumulation as shown in Fig. 5.4. Moderate isotopic shift related to a few samples from Chacana suggests the

occurrence of enhanced water-rocks interaction as previously shown in Fig. 5.4 e Fig. 5.5. Input of arc-type magmatic waters at Chachimbiro does not seem to be the only one to control the isotopic enrichment process. This observation is based on a larger number of samples from Aguilera et al. (2005). The extrapolation of the thermal water trend towards the δD and $\delta^{18}O$ of arc-type magmatic water [δD= -20‰ and $\delta^{18}O$= +10‰ (Giggenbach, 1992)] does not pass through the arc-type magmatic water value. According to the authors, the isotopic shifting matches, most likely, with significant water/rock exchange of oxygen isotopes supporting the water/rock interaction shown in Fig. 5.4 e 5.5).

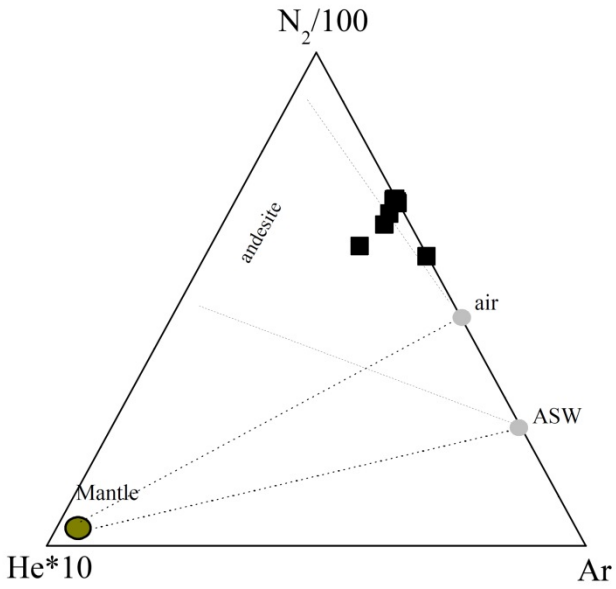

Fig. 5.6. N_2/100-Ar-He*10 triangular diagram from the geothermal areas of Chiles-Cerro Negro, Chachimbiro, Cuicocha, Chacana and Quilotoa.

5.5.2 Gas discharges

As reported in the N_2-Ar-He triangular plot (Fig. 5.6), all the samples display a N_2-excess with respect to atmospheric value, which is typical of the so called "andesitic" gases of Giggenbach (1978). The existence of a significant input of non-atmosferic N_2, together with the relatively high R/Ra values such as those observed at Chacana and Quilotoa (5.58, 5.04) and the values of $\delta^{13}C_{CO2}$ (ranging from -5 to -10‰) supports the idea of a mantle-like signature for these fluids (Fig. 5.7). Further suggestions concerning the relative contributions of mantle, crustal carbonate and biogenic carbon are provided by the relative amount of CO_2 and the inert noble gases (He and Ar) and their isotopic composition. According to Fig. 5.8, the investigated Ecuadorian gas samples cover a large spectrum of $CO_2/^3He$ ratios, from mantle- to limestone-derived compositions (Chacana area and Chiles-Cerro Negro and Chachimbiro areas, respectively) passing throughout an apparent mixture of the two (Quilotoa caldera). The observed vertical distribution of the samples could also result from different $CO_2/^3He$ fractionation due to the selective dissolution of CO_2 and He into the shallow aquifers. The slight shifting of gas compositions with respect to the mantle-limestone mixing curve suggest a modest but homogeneous contribute of biogenic carbon. The $CO_2/^3He$ vs $^3He/^4He$ (reported as Rc/Ra; Fig. 5.9) confirm an apparently prevailing crustal component in the northermost geothermal sites (Rc/Ra = 1.50 at Chachimbiro-Agua Savia and Rc/Ra = 3.13, 3.35 at Chiles-Cerro Negro), whereas a prevailing mantle component in the Chacana caldera, Quilotoa and Cuicocha volcanoes. The He isotopic values show that mantle

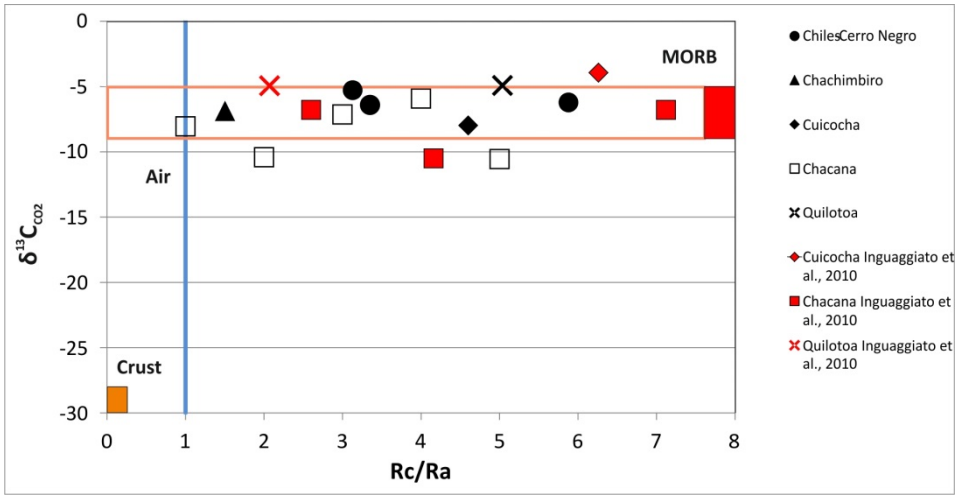

Fig. 5.7. $^{13}C_{CO2}$ of bubbling gas versus Rc / Ra; mid-ocean ridge basalts (MORB) and crust values are plotted as reference. Data from Inguaggiato et al., (2010) referred to Quilotoa, Chacana and Cuicocha are also reported for comparison.

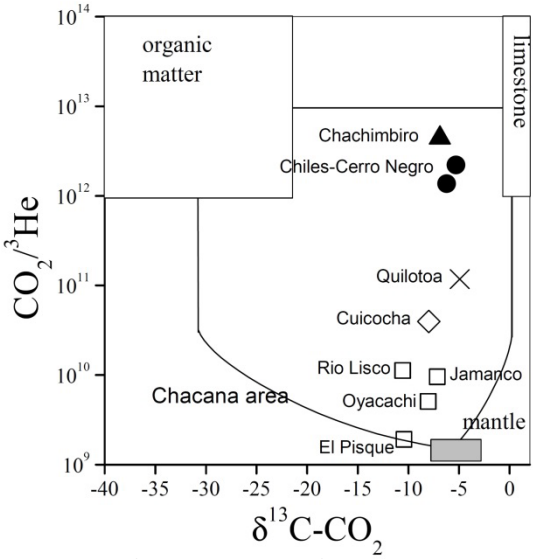

Fig. 5.8. $\delta^{13}C_{CO_2}$ versus $CO_2/^3He$ diagram.

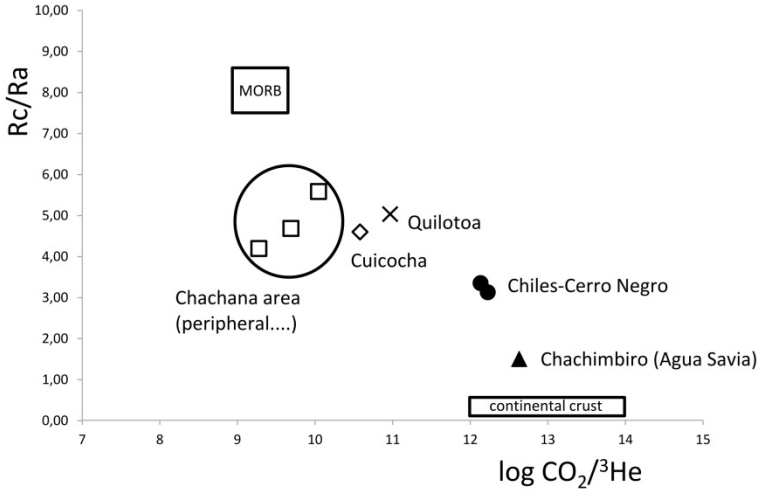

Fig. 5.9. log $CO_2/^3He$ versus $^3He/^4He$ diagram.

contribution was higher in the geothermal areas related to the active and semi-dormant volcanoes located between + 0.3°N and -1°S (Cuicocha, Chacana caldera and Quilotoa) with respect to that of the northernmost geothermal systems (between 0.5-1°N, i.e. Chiles-Cerro Negro and Chachimbiro). This spatial distribution of mantle He was possibly driven by the slab-tears inferred at this latitude of Ecuador, due to the flat-slab geometry linked to the Carnegie Ridge subduction (Gutscher et al., 1999).

5.5.3 R_H and T geoindicator

Giggenbach (1991) proposed that the H_2/Ar molar ratio could be representative of the deep degassing liquid. This ratio in the liquid phase is basically controlled by dominating redox conditions. These latter are well represented by the R_H value (R_H = log H_2/H_2O) due to the ability of the H_2/H_2O redox pair to instantaneously adjusts in response to variation in redox conditions (Giggenbach, 1980; 1987). Similarly, the CH_4/CO_2 ratio can be used to evaluate equilibrium temperatures according to:

(1)

$CH_4 + H_2O = CO_2 + H_2$

where

(2)

log Keq = f(T) = R_H - log CH_4/CO_2

The CH_4/CO_2 ratio is controlled by i) the dependence on of log Keq, and iii) the R_H value, that is in turns controlled by the redox-controlling system.

The dependence on R_H and temperature of the H_2-Ar and CH_4-CO_2 geothermometers can be expressed, as follows:

(3)

$R_H = -6.523 + 10.0492 – 0.014T + \log H_2/Ar$

(4)

$R_H = 1/4(– 5182/T + 2.41 – 0.0034T + \log (CH_4/CO_2)$

Substituting the measured values of log H_2/Ar and log CH_4/CO_2 to equations (3) and (4), the R_H = f(T) can be plotted in the R_H vs T diagram (Fig. 5.10). Assuming the attainment of equilibrium at the same P, T and redox conditions, the convergence point of the two curves directly provides T and R_H values at which the two systems were simultaneously equilibrated. In the R_H vs T plots, the R_H = f(T) of HM (Hematite-Magnetite), GT (FeO1.5-FeO) and DA (D'Amore and Panichi, 1980) redox buffer systems, were reported.

In the R_H vs T plot of Fig. 5.10a, the two gas samples from Chachimbiro area plot at equilibrium temperatures and R_H values in the range 149-153 °C and -3.80 ÷ -3.60 respectively, the latter being consistent with the DA redox buffer. Bubbling gases collected at Chiles-Cerro Negro area display slightly higher equilibrium temperatures (180-190 °C) at similar redox conditions (R_H = -3.76 ÷ -3.70; Fig. 5.10b). Gases from Lake Quilotoa apparently attained equilibrium at 200°C under redox conditions more oxidizing with respect to those dictated by the DA buffer (Fig. 5.10c). This could be related to loss of

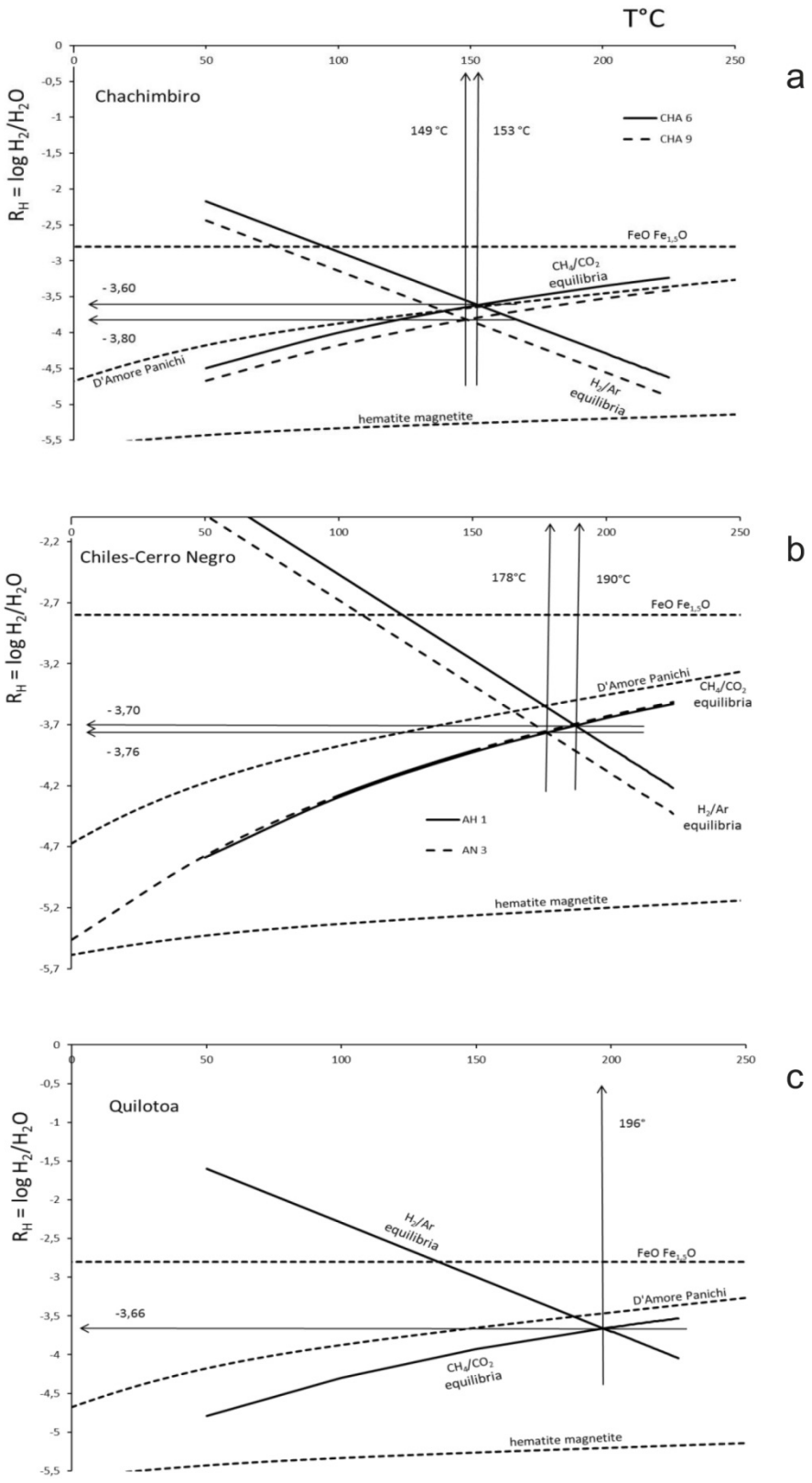

Fig. 5.10a-c: R_H versus T diagram.

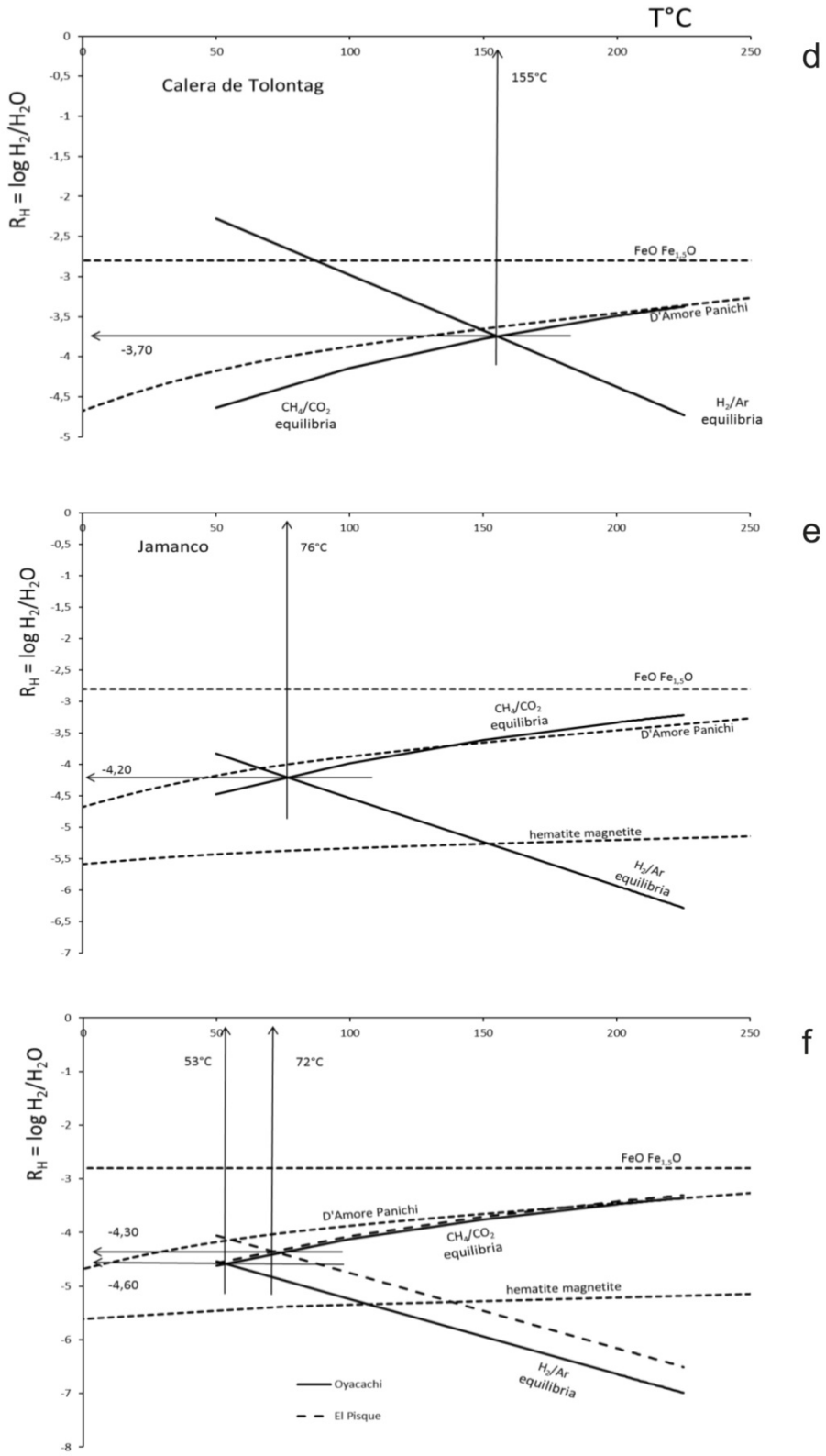

Fig. 5.10d-f: R_H versus T diagram.

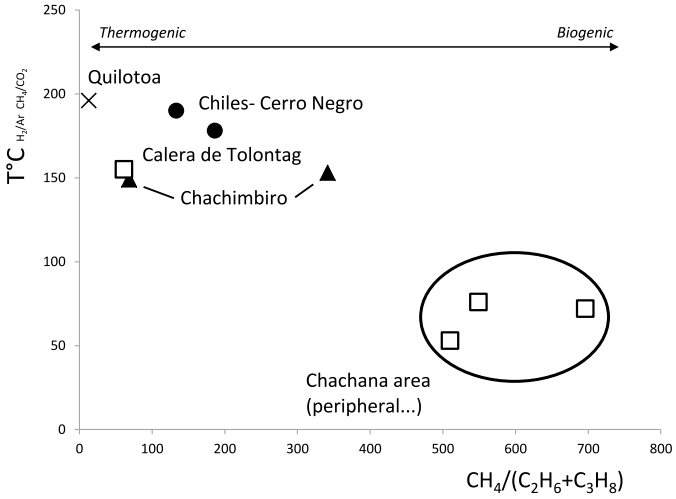

methane due to its oxidation at shallow depths (metanotrophic bacteria) and/or, as stated below, loss of hydrogen due to its conversion to methane (hydrogenotrophic bacteria) at more reducing conditions. Within the Chacana area, gas sample from Calera de Tolontag (Fig. 5.10d) displays temperature and R_H condition very similar to those from Chachimbiro, i.e. 155°C and R_H = -3,70. Conversely, gas samples collected at Jamanco (Fig. 5.10e) and Oyacachi and El Pisque (Fig. 5.10f) provide apparent equilibration temperatures < 100°C and $R_H \leq$ -4.20. However, only considering the CH_4-CO_2 geothermometer, these gases seem to have been equilibrated at 150÷170 °C and -3.70<R_H<-3.50, thus very close to the values obtained with the convergent geothermometers at Calera de Tolontag. This would suggest that at these sampling sites a significant H_2 removal could be occurred, possibly due to hydrogenotrophic bacteria at reducing conditions. The increasing fraction of bacterial methane at Oyacachi, Jamanco and El Pisque is also testified by samples distribution in the $CH_4/(C_2H_6+C_3H_8)$ vs T°C diagram (Fig. 5.11). Values of $CH_4/(C_2H_6+C_3H_8)$ > 500 (Bernard et al., 1978), which characterize gas samples from Oyacachi, Jamanco and El Pisque, typically suggest a bacterial origin of methane. Conversely, samples from Quilotoa and, at lesser extent, Chachimbiro, Calera de Tolontag and Chiles-Cerro Negro plot at $CH_4/(C_2H_6+C_3H_8)$ < 500, thus suggesting a prevailing thermogenic origin for methane.

Silica content ranges between 46 and 173 mg/L, the highest value being recorded in the Chachimbiro area. Temperatures calculated for equilibria of thermal waters with chalcedony (Fournier, 1991) and quartz (no steam loss) (Fournier, 1977) at Chachimbiro provide 148 and 170 °C respectively, which fits very well with temperature estimation according to gas phase equilibria (149-153 °C). Temperature ranges of 67-129 °C and 97-154 °C have been recorded respectively for chalcedony and quartz for water samples collected in the Chachana area. Also in this case, the recorded range of silica temperatures well fits with those calculated according to gas phase equilibria (53-155 °C). Thermal waters collected in the Chiles-Cerro Negro area report silica equilibration temperature for chalcedony in the range 109 – 132 °C and for quartz in the range 136-156 °C. In this case silica temperatures appear significantly lower with respect those calculated by using gas phase equilibria (178-190 °C).

5.6 CONCLUSIONS

Northern Ecuador is the site of superficial thermal springs mostly located along the active to semi-dormant volcanoes of the

Cordillera in the northern half of the country (Inguaggiato et al. 2010). The surface manifestations consist of thermal springs at medium to low temperature rarely associated with bubbling gases. The chemical features of waters reflect two different origins: emergences of shallow waters, heated by the uprising steam and sites of deeper reservoir partially or totally equilibrated with rock minerals and gas phases. Among the investigated samples those pertaining to Chachimbiro and Chacana geothermal systems represent thermal waters partially equilibrated with the hosting rocks, (i) the Pallatanga oceanic Terrain with overlying Late Cretaceous to Pliocene volcano-sedimentary successions and (ii) the Paleozoic-Mesozoic basement (mainly metamorphic rocks and overlying Miocene-Pliocene volcanic sequences) respectively. At Chachimbiro the direct emergence of the main liquid-dominated reservoir is characterized by thermal waters associated with free bubbling gases, possible equilibrated at the same temperature and redox conditions, i.e. 150-170 °C and -3.80<R_H<-3.60, that is controlled by the D'Amore and Panichi (1980) (DA) redox buffer. Samples from the Chachana caldera pertain to both Na-Cl waters from reservoir (Jamanco and Calera de Tolontag springs) and Na-HCO_3 peripheral waters (Rio Lisco, Oyacachi and El Pisque springs). The emergence of a mature geothermal reservoir at Calera de Tolontag also agrees with the calculated equilibrium temperature of the gas phase (155°C) and the R_H value, also in this case very close to the DA redox buffer. Silica temperature ranges between 60 and 154 °C thus confirming the previous temperature calculated with gas phase. Conversely, the location of the other water discharges is consistent with the lower calculated equilibrium temperature (<100°C) and higher oxidizing conditions (R_H>-4). Decoupled conditions between liquid and gas phases were recognized at Chile-Cerro Negro, where the acid waters with Na-SO_4 composition represent shallow, steam heated waters at temperature close to the boiling point, whereas the gas phase appears to be equilibrated at deeper PT conditions, i.e. 178÷190 °C and -3,76<R_H<-3,70, that is slightly more oxidizing with respect to the DA redox buffer system. Waters and gas phases from the caldera lake of Quilotoa volcano reveal a further decoupling conditions, in which lake waters represent a sort of condenser for chemicals carried upwards by geothermal gases and waters from the reservoir (196°C and R_H = -3,66), in particular H_3BO_3, Cl- and Na^+, as well as free gases, bubbling throughout it.

Summarizing, the chemico-physical characteristics of the investigated Ecuadorian geothermal areas display a high degree of heterogeneity from low enthalpy systems (Vertiente Rio Lisco, Oyacachi and El Pisque) to medium-high enthalpy systems (Chachimbiro, Chiles-Cerro Negro, Quilotoa). Mantle vs crustal contributions to the investigated fluids can pointed out by the He isotopic tracers coupled with carbon dioxide. A prevailing crustal component seem to characterize the geothermal fluids of the northernmost investigated volcanic complexes (Chiles-Cerro Negro and Chachimbiro) whereas mantle contribution is

higher in the Cuicocha, Chacana and Quilotoa calderas which are active and semi-dormant volcanoes being located at a latitude associated to slab-tears (e.g. prosecution of the Grijalva Fault Zone) of the flat-slab geometry due to the Carnegie Ridge subduction, making easier the influx to the surface of mantle-derived fluids.

REFERENCES

Aguilera, E., 1998. The Chalupas and Chachimbiro geothermal fields in Ecuador. Geotherm. Resour. Council Trans., 22, 247–251.

Aguilera, E., Chiodini, G., Cioni, R., Guidi, M., Marini, L., and Raco, B., 2000. Water chemistry of lake Quilotoa (Ecuador) and assessment of natural hazards, J. Volcanol. Geoth. Res., 97, 271–285.

Aguilera E., Cioni R., Gherardi F., Magro G., Marini L., Zhonghe P., 2005. Chemical and isotope characteristics of the Chachimbiro geothermal fluids (Ecuador). Geothermics, 34, 495 – 517.

Aguilera F., Ahumada S., Mercado J.L., Piscaglia F., Renzulli A., Tassi F., 2008. Geological survey, petrology and fluid geochemistry of the Apacheta-Aguilucho Volcanoes (Andean Central Volcanic Zone, Northern Chile) and their geothermal system. XXVII National Conference GNGTS, Trieste, 23 August.

Aguirre, I., Clavero, J., Simmons, S., Giavelli, A., Mayorga, C., Soffia, J., 2011. Colpitas-a new geothermal project in Chile. Geothermal Resources Council Transactions, 35, 1141–1145, California.

Alimonti, C., and Soldo, E., 2016. Study of geothermal power generation from a very deep oil well with a wellbore heat exchanger. Renewable Energy, 86, 292-301.

Almeida E., 1990. Alternativas para el desarrollo geotermoeléctrico en la República del Ecuador. Unp. Tech. Report for INECEL.

Andersen, D.J., and Lindsley, D.H., 1988. Internally consistent solution models for Fe-Mg-Mn-ti oxides: Fe-Ti oxides. The American Mineralogist, 73(7-8), 714-726.

Anderson, A.T., 1980. Significance of hornblende in calc-alkaline andesites and basalts. Am Mineral, 65(9-10), 837-851.

Anderson J.L., 1996. Status of thermobarometry in granitic batholiths. Trans. R. Soc. Edinb., 87,125–138.

Anderson, J.L., Barth, A.P., Wooden, J.L., and Mazdab, F., 2008. Thermometers and thermobarometers in granitic systems. Reviews in Mineralogy and Geochemistry, 69(1), 121-142.

Anderson J.L., Smith D.R., 1995. The effects of temperature and fO_2 on the Al-in-hornblende barometer. Am. Mineral., 80,549–559.

Aravena, D., Munoz, M., Morata, D., Lahsen, A., Parada, M. Á., and Dobson, P., 2016. Assessment of high enthalpy geothermal resources and promising areas of Chile. Geothermics, 59, 1-13.

Ármannsson, H. 2007. Application of geochemical methods in geothermal exploration. Short Course II on Surface Exploration for Geothermal Resources. Organized by: UNU-GTP, United Nations University Geothermal Training Programme. Lake Naivasha, Kenya, 2-7 November.

Árnason, K., and Gíslason, G., 2009. Geothermal surface exploration. Short Course on Surface Exploration for Geothermal Resources. Organized by

UNU-GTP and LaGeo, in Ahuachapan and SantaTecla, El Salvador.

Auker, M.R., Sparks, R.S.J., Jenkins, S.F., Aspinall, W., Brown, S.K., Deligne, N.I., Jolly, G., Loughlin, S.C., Marzocchi, W., Newhall, C.G. and Palma, J.L., 2015. Development of a new global Volcanic Hazard Index (VHI). In: S.C. Loughlin, R.S.J. Sparks, S.K. Brown, S.F. Jenkins and C. Vye-Brown (eds) Global Volcanic Hazards and Risk, Cambridge: Cambridge University Press.

Bachmann, O., and Dungan, M.A., 2002. Temperature-induced Al-zoning in hornblendes of the Fish Canyon magma, Colorado. American Mineralogist, 87(8-9), 1062-1076.

Barazangi M., and Isacks B.L., 1976. Spatial distribution of earthquakes and subduction of the Nazca plate beneath South America. Geology, 4, 41-47.

Barbier, E., 2002. Geothermal energy technology and current status: an overview. Renewable and Sustainable Energy Reviews, 6(1), 3-65.

Barckhausen, U., Ranero, C.R., Cande, S.C., Engels, M., Weinrebe, W., 2008. Birth of an intraoceanic spreading center. Geology, 36, 767.

Barla, G.B., 2008. Sviluppi e potenzialità della geotermia di nuova generazione.

Barragán, R., Geist, D., Hall, M., Larson, P., Kurz, M., 1998. Subduction controls on the compositions of lavas from the Ecuadorian Andes. Earth Planet. Sci. Lett.,154, 153–166.

Beate, B., 2001. Tefracronología Holocénica en el complejo Volcánico de Chachimbiro, prov. de Imbabura, Cuartas Jornadas en Ciencias de la Tierra, EPN, Quito, 3-6 de Abril, p. 46.

Beate B., Inguaggiato S., Villares F., Benitez S., Hidalgo S., 2010. The Cachiyacu Geothermal Prospect, Chacana Caldera, Ecuador. Proceedings World Geothermal Congress 2010, Bali, Indonesia.

Beate B., Salgado R., 2010. Geothermal Country Update for Ecuador, 2005 -2010. Proceedings World Geothermal Congress 2010 Bali, Indonesia, 25-29 April.

Beate, B., Urquizo, M., 2015. Proceedings World Geothermal Congress 2015, Melbourne, Australia, 19-25 April.

Beate B., Villares F., Inguaggiato S., Hidalgo S., Benitez S., 2009. Modelo geotérmico preliminar de tres áreas de interés en la caldera cuaternaria resurgente de chacana y estimación teórica de su potencial geotermoeléctrico. bibdigital.epn.edu.ec.

Beattie, P., 1993. Olivine-melt and orthopyroxene-melt equilibria. Contributions to Mineralogy and Petrology, 115(1), 103-111.

Beck S.L., Zandt G., 2002. The nature of the orogenic crust in the central Andes. J. Geophys. Res., 107 (B10), 2230.

Bernard B., Hidalgo S., Robin C., Beate B., Quijozaca J., 2014. The 3640–3510 BC rhyodacite eruption of Chachimbiro compound volcano, Ecuador: a violent directed blast produced by a satellite dome. Bull. Volcanol., 76, 849.

Bernard B., Robin C., Beate B., Hidalgo S., 2011. Nuevo modelo evolutivo y actividad eruptiva reciente del volcán Chachimbiro. Extended abstract in the "7mas Jornadas en Ciencias de la Tierra", Escuela Politécnica Nacional, November 23–25, Quito (Ecuador), pp 119–122.

Bernard, B.B., Brooks, J.M., Sackett, W.M., 1978. Light hydrocarbons in recent Texas

continental shelf and slope sediments. J. Geophys. Res. 83, 4053–4061.

Bertani R., 2012. Geothermal power generation in the world 2005-2010 update report. Geothermics, 41, 1–29.

Bertani R., 2015. Geothermal Power Generation in the World, 2010-2014 Update Report. Proceedings World Geothermal Congress 2015. Melbourne, Australia, 19-25 April, 2015.

Bertani, R., and Thain, I., 2002. Geothermal power generating plant CO2 emission survey. IGA News, 49, 1-3. http://iga.igg.cnr.it.

Blanco Ilzarbe, J.M., Malpartida, J.G., and Chandro, E.R., 2013. Recent Patents On Geothermal Power Extraction Devices. Recent Patents on Engineering, 7(1), 2-24.

Blodgett L., Slack K., 2009. Geothermal 101: basics of geothermal energy production and use. Geothermal Energy Association. Washington, DC.

Blundy, J., Cashman, K., and Humphreys, M., 2006. Magma heating by decompression-driven crystallization beneath andesite volcanoes. Nature, 443(7107), 76-80.

Blundy J., Holland T.J., 1990. Calcic amphibole equilibria and a new amphibole-plagioclase geothermometer. Contrib, Mineral, Petrol., 104, 208-224.

Boland, M.L., Pilatasig, L.F., Ibadango, C.E., McCourt, W.J., Aspden, J.A., Hughes, R.A., Beate, B., 2000. Geology of the Cordillera Occidental of Ecuador between 0° and 1°N. Proyecto de Desarrollo Minero y Control Ambiental, Programa de Informacion Cartografica y Geologica, CODIGEM–BGS, Quito, Informe 10.

Bona, P., and Coviello, M., 2016. Valoración y gobernanza de los proyectos geotérmicos en América del Sur: una propuesta metodológica.

Bourdon, E., Eissen, J.P., Gutscher, M.A., Monzier, M., Hall, M.L., Cotton, J., 2003. Magmatic response to early aseismic ridge subduction: the Ecuadorian margin case (South America). Earth Planet. Sci. Lett., 205, 123–138.

Bourgois, J., Eguez, A., Butterlin, J., De Wever, P., 1990. Evolution geodynamic de la Cordillere Occidentale des Andes d'Equateur: la decouverte de la formation eocene d'Apagua. C. R. Acad. Sci. Paris, 311 (II), 173-180.

British Petroleum, 2016. Statistical Review of World Energy 2016. BP, London.

Browne, B.L., and Gardner, J.E., 2006. The influence of magma ascent path on the texture, mineralogy, and formation of hornblende reaction rims. Earth and Planetary Science Letters, 246(3), 161-176.

Budiarto, R., Indarto, S.H., and Sutrisno, S. 2014. Recent development of non-conventional geothermal power plant. Proceedings of the 3rd Applied Science for Technology Innovation, August, 13-14.

Calvin, W.M., Coolbaugh M., and Kratt C., 2005. Application of remote sensing technology through geothermal exploration. Geological Society of Nevada 2005, pp.1083-1089.

Campbell R., 2006. Results of the Demonstration Power Plant on the Pleasant Bayou Geopressured Resource. SMU Geothermal Workshop, 2006.

Capaccioni B., Mangani F., 2001. Monitoring of active but quiescent volcanoes using light hydrocarbon distribution in volcanic gases: the results of 4 years of discontinuous monitoring in the Campi

Flegrei (Italy). Earth Planet. Sci. Lett., 188, 543-555.

Casey T., 2011. Timescales of Large Silicic Magma Systems: Implications from Accessory Minerals in Pleistocene Lavas of the Altiplano-Puna Volcanic Complex, Central Andes. Unpublished Master of Science Degree, Oregon State University.

Cepeda, H., Acevedo, A.P., Lesmes, L.E., 1987. Características químicas y petrográficas de los volcanoes Azufral, Cumbal y Chiles-Cerro Negro, Colombia, S.A. Informe Ingeominas. 25 pp. Medellín.

Chu, T.Y., Dunn J.C., Finger J.T., Rundle J.B. and Westrich H.R. 1990. The Magma Energy Program. Geothermal Resources Council Bulletin, 19 (2), 42-52.

Chiaradia M., Muntener O., Beate B., 2011. Enriched basaltic andesites from mid-crustal fractional crystallization, recharge, and assimilation (Pilavo Volcano, Western Cordillera of Ecuador). Journal of Petrolog,y 52:1107-1141.

Chiodini G., Marini L., Russo M., 2001. Geochemical evidence for the existence of high-temperature hydrothermal brines at Vesuvio Volcano, Italy. Geochim. Cosmochim. Acta, 65, 2129-2147.

Chmielowski J., Zandt G., 1999. The Central Andean Altiplano-Puna magma body. Geophysical Research Letters, 26(6), 783-786.

Civetta, L., Massimo, D.A., Orsi, G., and Tilton, G.R., 1998. The geochemistry of volcanic rocks from Pantelleria Island, Sicily Channel: petrogenesis and characteristics of the mantle source region. Journal of Petrology, 39(8), 1453-1491.

Clavero, J., Pineda, G., Mayorga, C., Giavelli, A., Aguirre, I., Simmons, S., Martini, S., Soffia, J., Arriaza, R., Polanco, E., and Achurra, L., 2011. Geological, geochemical, geophysical and first drilling data from Tinguiririca geothermal area, central Chile. Geothermal Resources Council Transactions, 35, 731-734.

Comida P.P., 2012. Ricostruzione cronostratigrafica e dinamica eruttiva dell'esplosione laterale olocenica del duomo Pucará (Ecuador). Unpublished Master Degree Thesis (in Italian), Università degli Studi di Pisa, pp 148.

Cordani U.G., Milani E.J., Thomaz Filho A., Campos D.A., 2000. Tectonic evolution of South America. 31st International Geological Congress, Rio de Janeiro Brazil 6-17 August.

Cortés G.P., Calvache M.L., 1996. Geología de los volcanes Chiles y Cerro Negro, Informe preliminar. Ingeominas, 41 p., Pasto.

Costa F., Andreastuti S., Bouvet de Maisonneuve C., Pallister J.S., 2013. Petrological insights into the storage conditions, and magmatic processes that yielded the centennial 2010 Merapi explosive eruption. Journal of Volcanology and Geothermal Research, 261, 209–235.

Coviello, M., 2000. Estudio para la Evaluación del Entorno del Proyecto Geotérmico Binacional “Tufiño-Chiles-Cerro Negro". Proyecto OLADE/CEPAL/GTZ. http://www.cepal.org/publicaciones/xml/6/5696/LCR1995-E.pdf

Cumming, W., Vieytes, H., Ramirez, C., Sussman, D., 2002. Exploration of the LaTorta geothermal prospect, northern Chile. In: Geothermal Resources CouncilTransactions, 26, 3–7, California.

Daly, M., 1989. Correlations between Nazca/Farallon plate kinematics and forearc basin evolution in Ecuador.

Tectonics, 8, 769–790. doi:10.1029/TC008i004p00769.

D'Amore, F., Panichi, C., 1980. Evaluation of deep temperatures of hydrothermal systems by a new gas geothermometer. Geochim. Cosmochim. Acta, 44, 549–556.

De Angelis S.H., Larsen J., Coombs M., 2013. Pre-eruptive magmatic conditions at Augustine volcano, Alaska, 2006: evidence from amphibole geochemistry and texture. J. Petrol., 54, 1939-1961.

DeMets C., Gordon R.G., Angus D.F., Stein C., 1990. Current plate motions. Geophys. J. Int., 101, 425–478.

de Silva S.L., 1989. Altiplano-Puna volcanic complex of the central Andes. Geology, 17, 1102-1106.

de Silva, S.L., Self, S., Francis, P.W., Drake, R.E., Ramirez, C.R., 1994. Effusive silicic volcanism in the Central Andes: the Chao dacite and other young lavas of the Altiplano-Puna Volcanic Complex. Journal of Geophysical Research, 99, 17805-17825.

de Silva S.L., Zandt G., Trumbull R., Viramonte J., Salas G., Jimenez N., 2006. Large ignimbrite eruptions and volcano-tecttonic depressions in the Central Andes: a termomechanical perspective. Geological Society of London, 269, 47-63.

Deichmann, N., and Giardini, D., 2009. Earthquakes Induced by the Stimulation of an Enhanced Geothermal System below Basel (Switzerland). Seismological Research Letters, 80 (5), (784–798).

DiPippo, R., 2012. Geothermal power plants: principles, applications, case studies and environmental impact. Butterworth-Heinemann.

Dixon P.A., Nakagawa M., 2016. Proceedings, 41st Workshop on Geothermal Reservoir Engineering Stanford University, Stanford, California, February 22-24, 2016, SGP-TR-209.

Droux A., Delaloye M., 1996. Petrography and geochemistry of Plio-Quaternary calc-alkaline volcanoes of southwestern Colombia. J. S. Am. Earth Sci., 9, 27–41.

Elders, W.A., Friðleifsson, G.Ó., and Albertsson, A., 2014. Drilling into magma and the implications of the Iceland Deep Drilling Project (IDDP) for high-temperature geothermal systems worldwide. Geothermics, 49, 111-118.

ElectraTherm, 2011. Denbury White Paper: Mississippi Oilfield Generates Low-Temperature, Emission Free Geothermal Energy at the Wellhead.

Emerging Energy Research, 2009. Emerging Energy Research: Global Geothermal Markets & Strategies.

Enel Latinoamérica (Chile) Ltda. Project Design Document (PDD).

Erdmann S., Martel C., Pichavant M., Kushnir A., 2014. Amphibole as an archivist of magmatic crystallization conditions: problems, potential, and implications for inferring magma storage prior to the paroxysmal 2010 eruption of Mount Merapi, Indonesia. Contrib. Mineral. Petrol., 167, 1016.

Evans, B.W., 2007. The synthesis and stability of some end-member amphiboles. Reviews in Mineralogy and Geochemistry, 67(1), 261-286.

ESMAP, 2012. ESMAP 2012 Annual Report. Energy Sector Management Assistance Program.

Feininger T., Seguin M.K., 1983. Simple Bouger gravity anomaly field and the inferred crustal structure of continental Ecuador. J. Geol., 11, 40-44.

Féménias, O., Mercier, J.C.C., Nkono, C., Diot, H., Berza, T., Tatu, M., and Demaiffe, D., 2006. Calcic amphibole growth and compositions in calc-alkaline magmas: Evidence from the Motru Dike Swarm (Southern Carpathians, Romania). American Mineralogist, 91(1), 73-81.

Friðleifsson, G.O., 2003. Iceland Deep Drilling Project. Feasibility Report. Part I: Geosciences and Site Selection, Part II: Drilling Technology, Part III: Fluid Handling and Evaluation. Orkustofnun. OS-2003/007, Reykjavík.

Friðleifsson G.Ó., Ármannsson H., Árnason K., Bjarnason I.Þ., Gíslason G., 2003. Part I: geosciences and site selection, 1–104. In: Friðleifsson, G.Ó.(Ed.), Iceland Deep DrillingProject, feasibility report. Iceland Energy Authority, Orkustof- nun Report OS-2003-007. Reykjavik, Iceland.

Friðleifsson, I.B., Bertani R., Huenges E., Lund J. W., Ragnarsson A., and Rybach L., 2008. The Possible Role and Contribution of Geothermal Energy to the Mitigation of Climate Change. Report for the Intergovernmental Panel on Climate Change (IPCC). Reykjavik, Iceland, February.

Friðleifsson, G.Ó., Elders, W.A., 2005. The Iceland Deep Drilling Project: a search for deep unconventional geothermal resources. Geothermics 34, 269–285.

Fridleifsson, G.O., Elders, W.a., Albertsson, A., 2014. The concept of the Iceland deep drilling project. Geothermics, 49, (2–8).

Fournier R.O. and Rowe J.J., (1977). The solubility of amorphous silica in water at high temperatures and high pressures. Am. Min. 62, 1052-1056.

Fournier, R. O., (1991). Water geothermometers applied to geothermal energy. Application of Geochemistry in Geothermal Reservoir Development, Ed Franco D'Amore. Unitar/UNDP, 37-69.

Friðleifsson, G.Ó., Elders,W.A., Albertsson,A., 2014. The concept of the Iceland Deep Drilling Project. Geothermics 49, 2–8.

Garnish J.D., Batchelor A.S., Ledingham P., 1992. Hot Dry Rock: fringe technology or key component? Proc. Internat. Conference on Industrial Uses of Geoth. Energy, Reykjavik, Iceland, 2–4 Sept. 1992, section A8, 1992. pp.8.

Gehringer, M., and Loksha, V., 2012. Geothermal handbook: planning and financing power generation. Energy Sector Management Assistance Program (ESMAP), Technical Report, 2, 12.

Genter, A., Goerke, X., Graff, J.J., Cuenot, N., Krall, G., Schindler, M., and Ravier, G., 2010. Current status of the EGS Soultz geothermal project (France).

Gherardi F., Spycher N., 2014. Application of Integrated Multicomponent Geothermometry at the Chachimbiro Thermal Area, a Difficult Geothermal Prospection Case. Proceedings, the 25th Workshop on Geothermal ReservoirEngineering (2013), Stanford University, Stanford, CA, SGP-TR-202.

Giggenbach, W.F., 1978. The isotopic composition of waters from the El Tatio geothermal field, Northern Chile. Geochimica et Cosmochimica Acta, 42(7), 979-988.

Giggenbach, W.F., 1980. Geothermal gas equilibria. Geochimica et cosmochimica acta, 44(12), 2021-2032.

Giggenbach, W.F., 1987. Redox processes governing the chemistry of fumarolic gas discharges from White Island, New Zealand. Applied Geochemistry, 2(2), 143-161.

Giggenbach, W.F., 1991. Chemical techniques in geothermal exploration. Application of

geochemistry in geothermal reservoir development, 11, 9-144.

Giggenbach, W.F., 1992. Isotopic shifts in waters from geothermal and volcanic systems along convergent plate boundaries and their origin. Earth Planet. Sci. Lett. 113, 495–510.

Global Volcanism Program, 2013a. Chiles-Cerro Negro (351110) in Volcanoes of the World, v. 4.5.0. Venzke, E (ed.). Smithsonian Institution. Downloaded 06 Sep 2016 (http://volcano.si.edu/volcano.cfm?vn=351110). http://dx.doi.org/10.5479/si.GVP.VOTW4-2013

Global Volcanism Program, 2013b. Quilotoa (352060) in Volcanoes of the World, v. 4.5.0. Venzke, E (ed.). Smithsonian Institution. Downloaded 06 Sep 2016 (http://volcano.si.edu/volcano.cfm?vn=352060). http://dx.doi.org/10.5479/si.GVP.VOTW4-2013

Gorini A., 2011. I vulcani Pilavo e Cerro Negro: un confronto petrografico e geochimico tra aree di arco frontale e retroarco in Ecuador. Unpublished Master Degree Thesis (in Italian), Università degli Studi di Urbino pp, 148.

Gudmundsson, J. S., 1985. Direct uses of geothermal energy in 1984. GRC Bulletin 14, 3–13.

Guiller B., Chatelain J.L., Jaillard E., Yepes H., Poupinet G., Fels J.F., 2001. Seismological evidence on the geometry of the orogenic system in central-northern Ecuador (South America). Geophys. Res. Lett. 28, 3749-3752.

Gunkel G., Beulker C., Grupe B., Viteri F., 2008. Hazards of volcanic lakes: analysis of Lakes Quilotoa and Cuicocha, Ecuador. Adv. Geosci., 14, 29–33.

Gunkel G., Beulker C., Grupe B., Viteri F., 2009. Survey and assessment of post volcanic activities of a young caldera lake, Lake Cuicocha, Ecuador. Nat. Hazards Earth Syst. Sci., 9, 699-712.

Gutscher, M.A., Malavieille, J., Lallemand, S., and Collot, J.Y., 1999. Tectonic segmentation of the North Andean margin: Impact of the Carnegie Ridge collision. Earth Planet. Sci. Lett., 168, 255–270. doi:10.1016/S0012-821X(99)00060-6.

Gutscher, M.A., Maury R., Eissen J.P., Bourdon E., 2000. Can slab melting be caused by flat subduction?. Geology, 28, 535-538.

Hall, M.L., Mothes, P.A., 1988. La actividad volcánica del Holoceno en el Ecuador y Colombia Austral: impedimento al desarrollo de las civilizaciones pasadas. In: Mothes, P.A. (Ed.), Actividad Volcanica y pueblos Precolombinos en el Ecuador. Abya-Yala, Quito, 11–40 pp.

Hall, M.L., Mothes, P.A., 2008a. Volcanic impediments in the progressive development of pre-Columbian civilizations in the Ecuadorian Andes. Journal of Volcanology and Geothermal Research, 176(3), 344-355.

Hall, M.L., Mothes, P.A., 2008b. The Chacana Caldera Complex in Ecuador. IOP Conference Series: Earth and Environmental Science, 3, 012004.

Hall M.L., Mothes P.A., 2008. Quilotoa volcano—Ecuador: an overview of young dacitic volcanism in a lake-filled caldera. J. Volcanol. Geotherm. Res 176, 44-55.

Hall, M.L., Samaniego, P., Le Pennec, J.L., and Johnson, J.B,. 2008. Ecuadorian Andes volcanism: A review of Late Pliocene to present activity. Journal of Volcanology and Geothermal Research, 176(1), 1-6.

Hammarstrom J.M., Zen E.A., 1986. Aluminium in hornblende: an empirical igneous geobarometer. Am. Mineral. 71, 1297–1313.

Hanuš, V., 1987. Deep seismically active fracture zones in Ecuador and Northern Peru. Studia geoph. et geod., 31, 8–25.

Hardee, H.C., Dunn, J.C., Hills R.G. and R.W. Ward, 1981. Probing the Melt Zone of Kilauea Iki Lava Lake, Kilauea Volcano, Hawaii. Geophysical Rev. Letters, 8(12), 1211-1214.

Hauser, A., 1997. Catastro y catacterización de las fuentes de aguas minerales ytermales de Chile (No.50). Servicio Nacional de Geología y Minería,Santiago.

Herzberg, C., Asimow, P.D., Arndt, N., Niu, Y., Lesher, C.M., Fitton, J.G., Cheadle M.J., and Saunders, A.D., 2007. Temperatures in ambient mantle and plumes: Constraints from basalts, picrites, and komatiites. Geochemistry, Geophysics, Geosystems, 8(2).

Hey, R., 1977. Tectonic evolution of the Cocos–Nazca spreading center. Geol. Soc. Amer. Bull., 88, 1404–1420.

Hickson, C.J., Ferraris, F., Rodriguez, C., Sielfeld, G., Henriquez, R., Gislason, T., Selters, J., Benoit, D., White, P., Southon, J., Ussher, G., Charroy, J., Smith, A., Lovelock, B., Lawless, J., Quinlivan, P., Smith, L., and Yehia, R., 2011. The Mariposa geothermal system, Chile. Geothermal Resources Council Transactions, 35, 817-825.

Hidalgo S., Monzier M., Almeida E., Chazot G., Eissen J.P., van der Plicht J., Hall M.L., 2008. Late Pleistocene and Holocene activity of the Atacazo–Ninahuilca volcanic complex (Ecuador). J Volcanol. Geotherm. Res., 176, 16-26.

Hidalgo S., Monzier M., Martin H., Chazot G., Eissen J.P., Cotten J., 2007. Adakitic magmas in the Ecuadorian Volcanic Front: Petrogenesis of the Illiniza Volcanic Complex (Ecuador). J. Volcanol. Geotherm. Res., 159, 366-392.

Hoffer, G., Eissen, J.P., Beate, B., Bourdon, E., Fornari, M., Cotten, J., 2008. Geochemical and petrological constraints on rear-arc magma genesis processes in Ecuador: the Puyo cones and Mera lavas volcanic formations. J. Volcanol. Geotherm. Res., 176, 107–118.

Holland T.J.B., Blundy J.D., 1994. Non-ideal interactions in calcic amphiboles and their bearing on amphibole-plagioclase thermometry. Contrib. Mineral. Petrol. 116, 433–447.

Hollister L.S., Grissom G..C, Peters E.K., Stowell H.H., Sisson V.B., 1987. Confirmation of the empirical correlation of Al in hornblende with pressure of solidification of calc-alkaline plutons. Am. Mineral. 72, 231–239.

Hólmgeirsson S., Guðmunsdsson Á., Pálsson B., Bóasson H.Á., Ingason K., Þórhallsson S., 2010. Drilling operations of the first Iceland Deep Drilling well (IDDP). In: Proceedings of the World Geothermal Congress 2010, Bali, Indonesia, 25-39 April, 2010. Paper 2129, pp.1–10.

Hristova D. 2015. Ecuador Celec contracts Imbavial for road to geothermal project. Renewable Now, 14 December 2015. https://renewablesnow.com/news/ecuador-celec-contracts-imbavial-for-road-to-geothermal-project-505572/

Hughes R.A., Pilatasing L.F., 2002. Cretaceous and Tertiary terrane accretion in the Cordillera Occidental of the Andes of Ecuador. Tectonophysics, 345, 29-48.

Humphreys M.C.S., Blundy J.D., Sparks R.S.J., 2006. Magma evolution and open-system processes at Shiveluch Volcano: insights from phenocryst zoning. J. Petrol. 47, 2303–2334.

Humphreys, M.C.S., Edmonds, M., Christopher, T., and Hards, V., 2009. Chlorine variations in the magma of

Soufrière Hills Volcano, Montserrat: Insights from Cl in hornblende and melt inclusions. Geochimica et Cosmochimica Acta, 73(19), 5693-5708.

IEA, 2013a. Resources to Reserves 2013: Oil, Gas and Coal Technologies for the Energy Markets of the Future. OECD Publishing, Paris.

IEA, 2013b. World Energy Outlook 2013. OECD Publishing, Paris.

IEA, 2015a. Energy and climate change: World Energy Outlook Special Report 2015.

IEA, 2015b. World Energy Outlook 2015. OECD Publishing, Paris.

IEA, 2016. Key Renewables Trends: Excerpt from Renewables Information 2016. IEA, Paris.

ICEL, 1983. Proyecto geotérmico Chiles-Cerro Negro. Fase I etapa de prefactibilidad. Informe preliminar. 146 p. Bogotá.

INECEL-OLADE-AQUATER: Proyecto Geotermico Binacional Tufiño-Chiles-Cerro Negro, informe de prefactibilidad, modelo geotérmico síntesis y recomendaciones. Unp. Tech. Report. (1987).

INER, (2015). Plan de Líneas de Investigación para el Desarrollo de la Geotermia. Instituto Nacional de Eficiencia Energética y Energías Renovables. Marzo de 2015. Documento disponible en: http://www.iner.gob.ec/wpcontent/uploads/downloads/2015/07/plan_lineas_investigacion_desarrollo_geotermia.pdf.

Inguaggiato, S., Hidalgo S., Beate B., Bourquin J., 2010. Geochemical and isotopic characterization of volcanic and geothermal fluids discharged from the Ecuadorian volcanic arc. Geofluids, 10, 525–541. doi: 10.1111/j.1468-8123.2010.00315.x

Inguaggiato, S., Rizzo, A., 2004. Dissolved helium isotope ratios in ground-waters: a new technique based on gas–water re-equilibration and its application to a volcanic area. Appl. Geochem. 19, 665–673.

Ishimaru, S., and Arai, S., 2008. Calcic amphiboles in peridotite xenoliths from Avacha volcano, Kamchatka, and their implications for metasomatic conditions in the mantle wedge. Geological Society, London, Special Publications, 293(1), 35-55.

Johnson M.C., Rutherford M.J., 1989. Experimental calibration of the aluminum-in-hornblende geobarometer with application to Long Valley caldera (California) volcanic rocks. Geology 17, 837–841.

Kagel, A., 2008. The State of Geothermal Technology, Part II: Surface Technology, GEA, Washington.

Karlsson, T., and Ragnarsson, A., (1995). Use of very low temperature geothermal water in radiator heating systems. In Proceedings of World Geothermal Congress,pp. 2193-2201.

Kellogg J.N., Vega V., 1995. Tectonic development of Panama, Costa Rica, and the Colombian Andes: constraints from global positioning system geodetic studies and gravity. Geol. Soc. Am. Spec. Pap., 295, 75-90

Kerr A.C., Aspden J.A., Tarney J., Pilatasing L.F., 2002. The nature and provenance of accreted terranes in Western Ecuador: geochemical and tectonic constraints. J. Geol. Soc. London, 159, 577-594.

Kiss B., Harangi S., Ntaflos T., Mason P.R.D., Pál-Molnár E., 2014. Amphibole perspective to unravel pre-eruptive processes and conditions in volcanic plumbing systems beneath intermediate

arc volcanoes: a case study from Ciomadul volcano (SE Carpathians). Contrib. Mineral. Petrol. 167, 986.

Kohl, T., and Speck, R., 2004. Electricity production by geothermal hybrid-plants in low-enthalpy areas. In Proc. 27th Stanford Workshop on Geothermal Reservoir Engineering, pp. 350-355.

Krawczynski, M.J., Grove, T.L., and Behrens, H., 2012. Amphibole stability in primitive arc magmas: effects of temperature, H2O content, and oxygen fugacity. Contributions to Mineralogy and Petrology, 164(2), 317-339.

Kuşcu, G.G., and Floyd, P.A., 2001. Mineral compositional and textural evidence for magma mingling in the Saraykent volcanics. Lithos, 56(2), 207-230.

Kyoto University. Successful demonstration of the world's first New Geothermal Power System carried out in Kokonoe, Oita Prefecture Online Publication, November 2016.

Lahsen, A. ,1976. Geothermal exploration in Northern Chile -summary. In: Circum-Pacific Energy and Mineral Resources. The American Association of petroleum Geologists, pp.169–175.

Lahsen, A., 1986. Origen y potencial de energía geotérmica en los Andes de Chile,Technical Report Geología y Recursos Minerales de Chile, Universidad deConcepción Concepción.

Lahsen, A., 1988. Chilean geothermal resources and their possible utilization.Geothermics, 17, 401-410.

Lahsen, A., Muñoz, N., Parada, M.A., 2010. Geothermal development in Chile. In: World Geothermal Congress, Bali, pp.25–29.

Lahsen, A., Rojas, J., Morata, D., and Aravena, D. 2015a. Exploration for high-temperature geothermal resources in the Andean countries of South America. In Proceedings of the world geothermal congress, Melbourne, Australia (19-25 April 2015).

Lahsen, A., Rojas, J., Morata, D., and Aravena, D. 2015b. Geothermal exploration in Chile: Country Update. In Proceedings of the world geothermal congress, Melbourne, Australia (19-25 April 2015).

Leake B.E., Woolley A.R., Arps C.E.S., Birch W.D., Gilbert M.C., Grice J.D., Hawthorne F.C., Kato A, Kisch H.J., Krivovichev V.G., Linthout K., Laird J., Mandarino J., Maresch W.V., Nickel E.H., Schumaker J.C., Smith D.C., Stephenson N.C.N., Ungaretti L., Whittaker E.J.W., Youzhi G., 1997. Nomenclature of amphiboles: report of the subcommittee on amphiboles of the International Mineralogical Association Commission on New Minerals and Mineral Names. Mineral. Mag. 61, 295–321.

Lebrat M., Megard F., Dupuy C., Dostal J., 1987. Geochemistry and tectonic setting of pre-collision Cretaceous and Paleogene volcanic rocks of Ecuador. Geol. Soc. Amer. Bull., 99, 569-578.

Leidig M., Zandt G., 2003. Modeling of highly anisotropic crust and application to the Altiplano-Puna volcanic complex of the central Andes. Journal of Geophysical Research, 108(b1), 2014.

Lichoro, C., 2014. Gravity and Magnetic Methods. UNU-GTP Short Course on IX on Exploration for Geothermal Resources. Lake Naivasha, Kenya, 2-24 November 2014.

Lindsay, J. M., Schmitt, A. K., Trumbull, R. B., De Silva, S. L., Siebel, W., and Emmermann, R. 2001. Magmatic evolution

of the La Pacana caldera system, Central Andes, Chile: compositional variation of two cogenetic, large-volume felsic ignimbrites. Journal of Petrology, 42(3), 459-486.

Litherland M., Aspden J.A., Jemielita R.A., 1994. The metamorphic belts of Ecuador. British Geological Survey, Keyworth, 147 pp.

Lonsdale, P., 1978. Ecuadorian subduction system. The American Association of Petroleum Geologists Bulletin, 62 (12), 2454–2477.

Lonsdale, P., 2005. Creation of the Cocos and Nazca plates by fission of the Farallon plate. Tectonophysics, 404, 237–264.

Lonsdale, P., Klitgord, K.D., 1978. Structure and tectonic history of the eastern Panama basin. Geol. Soc. Amer. Bull., 89, 1–9.

López Males G.G., Zura Quilumbango C.B., 2013. Correlación de los estudios magnéticos y gravimétricos con la geología del sector de Chachimbiro para prospección geotérmica. Unpublished Thesis (in Spanish). Universidad central del Ecuador. http://www.dspace.uce.edu.ec/handle/25000/726.

Lund, J.W., 1998. Geothermal Direct-Use Equipment Overview. GHC Bulletin, 19, 1–6.

Lund, J.W., 2009. Utilisation of geothermal resources. Proceedings of the Institution of Civil Engineers 162, 3–12.

Lund, J. W., and Chiasson, A., 2007. Examples of combined heat and power plants using geothermal energy. In Proceedings European geothermal congress. Unterhaching, Germany, 30 May-1 June 2007.

Lund, J.W., Freeston, D.H., Boyd, T.L., 2011. Direct utilization of geothermal energy 2010 worldwide review. Geothermics, 40, 159-180.

Mamyrin, B.A., Tolstikhin, I.N., 1984. Helium Isotopes in Nature. Elsevier, Amsterdam.

Mannvit hf, 2013. Mannvit hf: Environmental study on geothermal power.

Manzella, A., 1973. Geophysical Methods in Geothermal Exploration.

Marini, L. 2000. Geochemical techniques for the exploration and exploitation of geothermal energy. Italy: University of Genua.

Martins, L.T., Madeira, J., Youbi, N., Munhá, J., Mata, J., and Kerrich, R., 2008. Rift-related magmatism of the Central Atlantic magmatic province in Algarve, Southern Portugal. Lithos, 101(1), 102-124.

Mathieu-Potvin, F., 2013. Self-Superheating: A new paradigm for geothermal power plant design. Geothermics, 48, 16-30.

Melosh, G., Cumming, W., Benoit, D., Wilmarth, M., Colvin, A., Winick, J., Soto-Neira, E., Sussman, D., Urzua-Monsalve, L., Powell, T., and Peretz, A., 2010. Exploration results and resource conceptual model of the Tolhuaca geothermal field, Chile. Proceedings, World Geothermal Congress 2010, Bali, Indonesia, 25-29 April, 2010, 7 p.

Melosh, G., Moore, J., and Stacey, R., 2012. Natural reservoir evolution in the Tolhuaca geothermal field, Southern Chile. Proceedings, 36th Workshop on Geothermal Reservoir Engineering, Stanford University, Stanford, CA. SGP-TR-194.

Mercado J.L., Ahumada S., Aguilera F., Medina E., Renzulli A., Piscaglia F., 2009. Geological and Structural Evolution of Apacheta-Aguilucho Volcanic Complex (AAVC), Northern Chile. XII Congreso

Geológico Chileno Santiago, 22-26 November.

Milliken, M., 2007. Geothermal resources at naval petroleum reserve-3 (NPR-3), Wyoming. Proceedings Thirty-Second Workshop on Geothermal Reservoir Engineering, Stanford University. Stanford, California, January 22-24, 2007.

Molina, J.F., Moreno, J.A., Castro, A., Rodríguez, C., and Fershtater, G.B., 2015. Calcic amphibole thermobarometry in metamorphic and igneous rocks: New calibrations based on plagioclase/amphibole Al-Si partitioning and amphibole/liquid Mg partitioning. Lithos, 232, 286-305.

Montegrossi, G., Tassi, F., Vaselli, O., Buccianti, A., Garofano, K., 2001. Sulfur species in volcanic gases. Anal. Chem. 73, 3709–3715.

Monzier, M., Robin, C., Samaniego, P., Hall, M.L., Cotten, J., Mothes, P., Arnaud, N., 1999. Sangay volcano, Ecuador: structural development, present activity and petrology. J. Volcanol. Geotherm. Res., 90, 49–79.

Muffler, L.J.P., 1979. Assessment of Geothermal Resources of the United States-1978. The United States Geological Survey.

Muffler, P., and Cataldi, R., 1978. Methods for regional assessment of geothermal resources. Geothermics, 7(2-4), 53-89.

Müller, R.D., Sdrolias, M., Gaina, C., Roest, W.R., 2008. Age, spreading rates and spreading asymmetry of the world's ocean crust. Geochemistry, Geophysics, Geosystems, 9 (4). Q04006, doi:10.1029/2007GC001743.

Nabighian, M.N., Grauch, V.J.S., Hansen, R.O., LaFehr, T.R., Li, Y., Peirce, J.W., Phillips J.D., and Ruder, M.E., 2005. The historical development of the magnetic method in exploration. Geophysics, 70(6), 33ND-61ND.

Niida, K., and Green, D.H., 1999. Stability and chemical composition of pargasitic amphibole in MORB pyrolite under upper mantle conditions. Contributions to Mineralogy and Petrology, 135(1), 18-40.

Norabuena E.O., Dixon T.H., Stein S., Harrison C.G.A., 1999. Decelerating Nazca-South America and Nazca-Pacific plate motions. Geophys. Res. Lett., 26, 3405-3408.

Ochieng, L., 2013. Overview of geothermal surface exploration methods. In Presented at Short Course VIII on Exploration for Geothermal Resources. Organized by UNU-GTP at Lake Bogoria/Naivasha, Kenya.

Ochsner, K., 2008. Geothermal Heat Pumps. A guide for Planning & Installing. Earthscan, London.

Pálsson, B., Hólmgeirsson,S., Guðmundsson, Á., Bóassson, H.Á., Ingason, K., Þórhallsson, S., 2014. Drilling Well IDDP-1. Geothermics, 49, 23–30.

Pennington, W.D., 1981. Subduction of the Eastern Panama Basin and seismotectonics of northwestern South America. J. Geophys. Res., 86 (B11), 10753–10770.

Peréz, D.Y., 1999. Fuente de aguas termales de la Cordillera Andina del centro-sur de Chile (39–42°S). Servicio Nacional de Geología y Minería, Santiago, 1 map 1:500,000.

Pioro, I., and Mokry, S., 2011. Thermophysical properties at critical and supercritical conditions. Heat Transfer: Theoretical Analysis, Experimental Investigations and Industrial Systems, A. Belmiloudi, ed., INTECH, Rijeka, Croatia, 573-592.

Pipan, M., 2009: Remote sensing and geophysical methods for geothermal exploration. Presented at the School on Geothermics, organised by ICTP, ICS-UNIDO and IAEA, Trieste, Italy.

Piscaglia F., 2011. The high temperature geothermal field of the Apacheta-Aguilucho Volcanic Complex (northern Chile): geopetrographic surface exploration, crustal heat sources and cap rocks. Unpublished Ph.D. Thesis (in Italian), Università di Urbino, pp 174.

Pratt W.T., Pablo D., Ponce M., 2005. An autochtonous geological model for the eastern Andes of Ecuador. Tectonophysics, 339, 251-278.

Putirka, K.D., 2005. Igneous thermometers and barometers based on plagioclase+ liquid equilibria: Tests of some existing models and new calibrations. American Mineralogist, 90(2-3), 336-346.

Putirka, K.D., Mikaelian, H., Ryerson, F., and Shaw, H., 2003. New clinopyroxene-liquid thermobarometers for mafic, evolved, and volatile-bearing lava compositions, with applications to lavas from Tibet and the Snake River Plain, Idaho. American Mineralogist, 88(10), 1542-1554.

REN21, 2016. Renewables 2016 Global Status Report. Paris: REN21 Secretariat.

Reed, M., and Spycher, N., 1984. Calculation of pH and mineral equilibria in hydrothermal waters with application to geothermometry and studies of boiling and dilution. Geochimica et Cosmochimica Acta, 48(7), 1479-1492.

Renzulli A., Menna M., Tibaldi A., Flude S., 2006. New data of surface geology, petrology and Ar-Ar geochronology of the Altiplano-Puna Volcanic Complex (northern Chile) in the framework of future geothermal exploration. XI Congreso Geòlogico Chileno, Antofagasta, 7-11 August.

Reynaud C., Jaillard E., Lapierre H., Mamberti M., Mascle G.H., 1999. Oceanic plateau and island arcs of southwestern Ecuador: their place in the geodynamic evolution of northwestern South America. Tectonophysics, 307, 235-254.

Riahi A., Moncarz P., Kolbe W., Damjanac B. 2017. Innovative Closed-Loop Geothermal Well Designs Using Water and Super Critical Carbon Dioxide as Working Fluids. Proceedings, 42nd Workshop on Geothermal Reservoir Engineering Stanford University, Stanford, California, February 13-15, 2017.

Ridolfi F., Puerini M., Renzulli A., Menna M., Toulkeridis T., 2008. The magmatic feeding system of El Reventador volcano (Sub-Andean zone, Ecuador) constrained by texture, mineralogy and thermobarometry of the 2002 erupted products. Journal of Volcanology and Geothermal Research, 176, 94–106.

Ridolfi F., Renzulli A., 2012. Calcic amphiboles in calc-alkaline and alkaline magmas: thermobarometric and chemometric empirical equations valid up to 1,130 °C and 2.2 GPa. Contrib Mineral. Petrol., 163(5), 877–895.

Ridolfi, F., Renzulli, A., Perugini, D., Cesare, B., Braga, R., and Del Moro, S., 2016. Unravelling the complex interaction between mantle and crustal magmas encoded in the lavas of San Vincenzo (Tuscany, Italy). Part I: Petrography and Thermobarometry. Lithos, 244, 218-232.

Ridolfi F., Renzulli A., Puerini M., 2010a. Stability and chemical equilibrium of amphibole in calc-alkaline magmas: an overview, new thermobarometric formulations and application to

subduction- related volcanoes. Contr. Mineral. Petrol., 160,45-66.

Ridolfi F., Puerini M., Renzulli A., Menna M., Toulkeridis T., 2008. The magmatic feeding system of El Reventador volcano (Sub-Andean zone, Ecuador) constrained by texture, mineralogy and thermobarometry of the 2002 erupted products. J. Volcanol. Geotherm. Res., 176, 94–106.

Ridolfi F., Renzulli A., Cerredo M.E., Oberti R., Boiocchi M., Bellatreccia F., Della Ventura G., Menichetti M., Tassone A., 2010b. Amphibole megacrysts of the Cerro Jeu-Jepe´n pluton: new constraints on magma source and evolution (Fuegian Andes, Argentina). GEOSUR 2010, Buenos Aires, 22–23 November 2010, 80-82.

Robin C., Eissen J.P., Samaniego P., Martin H., Hall M., Cotten J., 2009. Evolution of the late Pleistocene Mojanda-Fuya Fuya volcanic complex (Ecuador), by progressive adakitic involvement in mantle sources. Bulletin of Volcanology, 71, 233-258.

Robin C., Samaniego P., Le Pennec J.L., Mothes P., van der Plicht J., 2008. Late Holocene phases of dome growth and Plinian activity at Guagua Pichincha volcano Ecuador). Journal of Volcanology and Geothermal Research, 176, 7–15.

Rollinson, H.R., 1993. Using Geochemical Data: Evaluation, Presentation, Interpretation. Longman Group UK Ltd., New York. 352.

Roobol M.J., Francis P.W., Ridley W.I., Rhodes M., Walker G.P.L., 1974. Physicochemical characters of the Andean volcanic chain, between latitudes 21° and 22° south. Symposium internacional de Volcanologia, IAVCEI, Santiago, Chile, Sept 9-14th, 1974.

Ruiz, M., 2015. Temporal Evolution of a Seismic Swarm at Chiles-Cerro Negro volcanic complex. European Geosciences Union, General Assembly 2015, Vienna.

Rutherford M.J., Devine J.D., 2003. Magmatic conditions and magma ascent as indicated by hornblende phase equilibria and reactions in the 1995–2002 Soufriere Hills magma. J. Petrol., 44, 1433–1454.

Rojas, F., 2015. ENEL da más detalles sobre Cerro Pabellón, la primera planta geotérmica de Chile. Piensa en Geotermia, 29 July 2015. http://piensageotermia.com/archives/25339.

Rutherford M.J., Devine J.D., 2008. Magmatic conditions and processes in the storage zone of the 2004–2006 Mount St. Helens Dacite. In: Sherrod DR, Scott WE, Stauffer PH (eds) A Volcano Rekindled: The renewed eruption of Mount St. Helens, 2004–2006. US Geological Survey Professional Paper 2007–2008, Chapter 31, pp 24.

Rutherford M.J., Hill P.M., 1993. Magma ascent rates from amphibole breakdown: An experimental study applied to the 1980-1986 Mount St Helens eruptions. J. Geophys. Res., 98(B11):19667-19685.

Saemundsson, K., Axelsson, G., and Steingrímsson, B., 2009. Geothermal systems in global perspective. Short Course on Exploration for Geothermal Resources, UNU GTP, 11.

Salgado, G., & Raasch, G. (2002). Recent geothermal industry activity and the market for electric power in Chile. Transaction-geothermal resources council, 55-58.

Salisbury, M.J., Jicha, B.R., de Silva, S.L., Singer, B.S., Jiménez, N.C., and Ort, M.H., 2011. $^{40}Ar/^{39}Ar$ chronostratigraphy of Altiplano-Puna volcanic complex

ignimbrites reveals the development of a major magmatic province. GSA Bulletin, 123(5-6), 821-840.

Samaniego P., Martin H., Monzier M., Robin C., Fornari M., Eissen J.P., Cotton J., 2005. Temporal evolution of magmatism in the northern volcanic zone of the Andes: the geology and petrology of Cayambe Volcanic Complex (Ecuador). J. Petrol., 46 (11), 2225-2252.

Samaniego, P., Martin, H., Robin, C., Monzier, M., 2002. Transition from calc-alkalic to adakitic magmatism at Cayambe volcano, Ecuador: Insights into slab melts and mantle wedge interactions. Geology, 30, 967–970, doi: 10.1130/0091-7613(2002)030<0967:TFCATA>2.0.CO;2.

Santucci G., 2013. EGS Enhanced Geothermal Systems: una sfida da raccogliere (in Italian); 1st Mediterranean Energy&Efficiency Tour. Matera, 8 June 2013.

Sato, H., Holtz, F., Behrens, H., Botcharnikov, R., and Nakada, S., 2005. Experimental petrology of the 1991–1995 Unzen dacite, Japan. Part II: Cl/OH partitioning between hornblende and melt and its implications for the origin of oscillatory zoning of hornblende phenocrysts. Journal of Petrology, 46(2), 339-354.

Savov, I.P., Luhr, J.F., and Navarro-Ochoa, C., 2008. Petrology and geochemistry of lava and ash erupted from Volcán Colima, Mexico, during 1998–2005. Journal of Volcanology and Geothermal Research, 174(4), 241-256.

Scaillet, B., and Evans, B.W., 199). The 15 June 1991 eruption of Mount Pinatubo. I. Phase equilibria and pre-eruption P–T–fO2–fH2O conditions of the dacite magma. Journal of Petrology, 40(3), 381-411.

Schmidt M.W., 1992. Amphibole composition in tonalite as a function of pressure; an experimental calibration of the Al-in-hornblende barometer. Contrib. Mineral. Petrol., 110, 304–310.

Schmitz M., Lessel K., Giese F., Wigger F., Araneda M., Bribach J., Graeber F., Grunewald S., Haberland C., Lüth S., Röber F., Ryberg T., Schulze A., 1999. The crustal structure beneath the Central Andean forearc and magmatic arc as derived from seismic studies – the PISCO 94 experiment in northern Chile (21° - 23° S). Journal of South American Earth Sciences, 12, 237-260.

Scott, S., Driesner, T., and Weis, P., 2015. Geologic controls on supercritical geothermal resources above magmatic intrusions. Nature, 6(7837).

Self, S.J., Reddy, B.V., Rosen, M.A., 2013. Geothermal heat pump systems: Status review and comparison with other heating options. Applied Energy, 101, 341–348.

Seton, M., Mueller, R.D., Zahirovic, S., Gaina, C., Torsvik, T., Shepard, G., Talsma, A., Gurnis, M., Turner, M., Chandler, M., 2012. Global continental and ocean basin reconstructions since 200 Ma. Earth-Science Reviews, 113, 212-270.

Shafiee, S., and Topal, E., 2009. When will fossil fuel reserves be diminished?. Energy policy, 37(1), 181-189.

Shah, M., Sircar, A., Vaidya, D., Sahajpal, S., Chaudhary, A., & Dhale, S., 2015. Overview of geothermal surface exploration methods. Int. J. Adv. Re.s Innov. Ideas. Educ., 1(4), 55-64.

Shane P., Smith V., 2013. Using amphibole crystals to reconstruct magma storage temperatures and pressures for the post-caldera collapse volcanism at Okataina volcano. Lithos, 156, 159–170.

Shea T., Hammer J.E., 2013. Kinetics of cooling and decompression-induced crystallization in hydrous mafic-intermediate magmas. Journal of Volcanology and Geothermal Research, 260, 127-145.

Shea, T., and Hammer, J.E., 2013. Kinetics of cooling-and decompression-induced crystallization in hydrous mafic-intermediate magmas. Journal of Volcanology and Geothermal research, 260, 127-145.

Sigfússon, B., and Uihlein, A., 2015. 2014 JRC Geothermal Energy Status Report.

Simakin, A., Zakrevskaya, O., and Salova, T., 2012. Novel amphibole geo-barometer with application to mafic xenoliths. Earth Science Research, 1(2), 82.

Sofia, J., and Clavero, J., 2010. Doing geothermal exploration business in Chile, Energia Andina experience. Geothermal Resources Council Transactions, 34, 637-641.

Spycher, N., Peiffer, L., Sonnenthal, E.L., Saldi, G., Reed, M. H., and Kennedy, B. M., 2014. Integrated multicomponent solute geothermometry. Geothermics, 51, 113-123.

Spycher, N., Sonnenthal, E., and Kennedy, B. M., 2011. Integrating multicomponent chemical geothermometry with parameter estimation computations for geothermal exploration. GRC Transactions, 35, 663-666.

Spikings, R., Winkler, W., Hughes, R., and Handler, R., 2005. Thermochronology of allochthonous terranes in Ecuador: Unravelling the accretionary and post-accretionary history of the Northern Andes. Tectonophysics, 399, 195-220. doi: 10.1016/j.tecto.2004.12.023.

Spikings, R., Winkler, W., Seward, D., and Handler, R., 2001. Along-strike variations in the thermal and tectonic response of the continental Ecuadorian Andes to the collision with heterogeneous oceanic crust. Earth Planet. Sci. Lett., 186, 57-73. doi: 10.1016/S0012821X(01)00225-4.

Stern C.R., 2004. Active Andean volcanism: its geologic and tectonic setting. Revista Geológica de Chile 31:161-206.

Streck M.J., 2008. Mineral textures and Zoning as evidence for Open System Processes Reviews in Mineralogy and Geochemistry, 69, 595-622.

Stroncik, N.A., Klügel, A., and Hansteen, T.H., 2009. The magmatic plumbing system beneath El Hierro (Canary Islands): constraints from phenocrysts and naturally quenched basaltic glasses in submarine rocks. Contributions to Mineralogy and Petrology, 157(5), 593-607.

SYR. Chachimbiro Pre-Feasibility Study presentation: informe final.

Tassi F., Aguilera F., Darrah T., Vaselli O., Capaccioni B., Poreda R.J., Delgado Huertas, A., 2010. Fluid geochemistry of hydrothermal systems in the Arica-Parinacota, Tarapacá and Antofagasta regions (northern Chile). Journal of Volcanology and Geothermal Research, 192, 1-15.

Tassi F., Vaselli O., Capaccioni B., Giolito C., Duarte E., Fernandez E., Minissale A., Magro G., 2005. The hydrothermal-volcanic system of Rincon de la Vieja volcano (Costa Rica): a combined (inorganic and organic) geochemical approach to understanding the origin of the fluid discharges and its possible application to volcanic surveillance. J. Volcanol. Geoth. Res., 148, 315–333.

Taylor, M.A., 2008. The State of Geothermal Technology, Part I: Subsurface Technology, GEA, Washington.

Tester, J.W., Anderson, B.J., Batchelor, A.S., Blackwell, D.D., DiPippo, R., Drake, E.M. Garnish J., Livesay B., Moore M.C., Nichols K., Petty S., Toksoz M.N., Veatch R.W., Baria R., Augustine C., Murphy E., Negraru P., Richards M., 2007. Impact of enhanced geothermal systems on US energy supply in the twenty-first century. Phil. Trans. R. Soc. A., 365, 1057–1094.

Thornber, C.R., Heliker, C., Sherrod, D.R., Kauahikaua, J.P., Miklius, A., Okubo, P.G., Trusdell, F.A., Budahn, J.R., Ridley, W.I., Meeker, G.P., 2003. Kilauea east rift zone magmatism: An episode 54 perspective. Journal of Petrology, 44(9), 1525-1559.

Thornber C.R., Pallister J.S., Lowers H.A., Rowe M.C., Mandeville C.W., Meeker G.P., 2008. Chemistry, mineralogy, and petrology of amphibole in Mount St. Helens 2004–2006 dacite. In: Sherrod DR, Scott WE, Stauffer PH (eds) A Volcano rekindled: the renewed eruption of Mount St. Helens, 2004–2006, USGS Professional Paper, 1750, 727-754.

Thorpe R.S., Francis P., 1979. Variations in Andean andesite composition and their petrogenetic significance. Tectonophysics, 57, 53-70.

Thorpe R. S., Francis P., O'Callaghan L., 1984. Relative role of source composition, fractional, crystallization and crustal contamination in petrogenesis of Andean volcanic rocks. Philosophical Transaction of the Royal Society of London; Series A: Mathematical and Physical Sciences, Vol.310, pp.675-692.

Tocchi, E., 1923. Il Tatio, ufficio geológico Larderello SpA (Unpublished report).

Turner, S.J., Izbekov, P., and Langmuir, C., 2013. The magma plumbing system of Bezymianny Volcano: Insights from a 54year time series of trace element whole-rock geochemistry and amphibole compositions. Journal of Volcanology and Geothermal Research, 263, 108-121.

Urzua, L., Powell, T., Cumming, W., Dobson, P., 2002. Apacheta, a new geothermal prospect in northern Chile. Geothermal Resources Council Transactions, 26, 65-69.

Vallejo, C., 2007. Evolution of the Western Cordillera in the Andes of Ecuador (Late Cretaceous–Paleogene). Ph.D. thesis, Institute of Geology, ETH Zürich, 208 pp. http://e-collection.ethbib.ethz.ch/show?type=diss&nr=17023.

Vallejo, C., Winkler, W., Spikings, R. A., Luzieux, L., Heller, F. & Bussy, F. 2009. Mode and timing of terrane accretion in the forearc of the Andes in Ecuador. In: Geological Society of America, Memoir, 204, 197-216.

Vaselli, O., Tassi, F., Montegrossi, G., Capaccioni, B., Giannini, L., 2006. Sampling and analysis of volcanic gases. Acta Volcanol. 18, 65-76.

Von Hillebrandt C., 1989. Estudio geovolcanológico del Complejo Volcánico Cuicocha-Cotacachi y sus aplicaciones. Provincia de Imbabura, Tesis de Ingeniería, Escuela Politécnica Nacional, Quito-Ecuador

Ward K.M., Zandt G., Beck S.L., Christensen D.H., McFarlin H., 2014. Seismic imaging of the magmatic underpinnings beneath the Altiplano-Puna volcanic complex from the joint inversion of surface wave dispersion and receiver functions. Earth Planet. Sci. Lett., 404, 43-53.

Wight, N.M., and Bennett, N.S., 2015. Geothermal energy from abandoned oil and gas wells using water in combination with a closed wellbore. Applied Thermal Engineering, 89, 908-915.

Yücel, C., Arslan, M., Temizel, I., and Abdioğlu, E., 2014. Volcanic facies and mineral chemistry of Tertiary volcanics in the northern part of the Eastern Pontides, northeast Turkey: implications for pre-eruptive crystallization conditions and magma chamber processes. Mineralogy and Petrology, 108(3), 439-467.

Zandt G., Leidig M., Chmielowski J., Baumont D., Yuan X., 2003. Seismic Detection and characterization of the Altiplano-Puna Magma Body, Central Andes. Pure and applied Geophysics, 160, 789-807.

Zang, A., Oye, V., Jousset, P., Deichmann, N., Gritto, R., McGarr, A., Majer, E., Bruhn, D., 2014. Analysis of induced seismicity in geothermal reservoirs-An overview. Geothermics, 52, 6-21.